TECHNISCHE
UNIVERSITÄT
DARMSTADT

Physik

Charged particle multiplicity studies in proton-proton collisions at a centre-of-mass energy of 10 TeV with the ALICE detector

Vom Fachbereich Physik
der Technischen Universität Darmstadt

zur Erlangung des Grades
eines Doktors der Naturwissenschaften (Dr. rer. nat.)

genehmigte Dissertation von
Dipl.-Phys. Juan Francisco Castillo Hernández
aus Sevilla

Referent: Prof. Dr. Braun-Munzinger
Korreferent: Prof. Dr. Wambach

Tag der Einreichung: 12.5.2010
Tag der Prüfung: 30.6.2010

Darmstadt 2012
D 17

Referent: Prof. Dr. Braun-Munzinger
Korreferent: Prof. Dr. Wambach

Tag der Einreichung: 12.5.2010
Tag der Prüfung: 30.6.2010

Contents

Abstract

Particle multiplicity is one of the basic observables in hadron and nuclear collisions. In a proton-proton (pp) system, the measured multiplicity distributions indicate that the hadrons emerging from the collision cannot be considered as produced independently from each other. Furthermore, the correlation between the forward and backward multiplicities reveals the longitudinal size of the particle sources. Sound understanding of these effects in pp system is prerequisite before a similar study of nuclear collisions can be undertaken.

In this work I describe a charged particle multiplicity analysis prepared for the ALICE experiment at CERN LHC. The analysis is focused on multiplicity distributions and forward-backward multiplicity correlations, and was extensively tested using simulated pp collision events. The latter were produced using realistic event generators tuned for the energies at which experimental data exist, and extrapolated to LHC. The analysis scheme and the results are described in Sections 4 and 5. The emphasis is put on the response of the ALICE apparatus to the observables under discussion.

The multiplicity analysis is based on the particle tracks measured with the ALICE Time Projection Chamber (TPC). The TPC is an excellent charged particle detector with large coverage and high resolution, the latter, however, achievable only if the working conditions are well under control. Two essential parameters, the electron drift velocity and the gas gain, are monitored by a dedicated device called Gas prOportional cOunter For drIfting Electrons (GOOFIE). Installation, commissioning, and operation of GOOFIE, described in Section 2.3, were the practical part of this thesis work.

Zusammenfassung

Teilchenmultiplizität ist eine der grundlegenden Observablen in Hadronen- und Kernstößen. Im Proton-proton-System (pp-System) deutet die gemessene Multiplizitätsverteilung darauf hin, dass die in der Kollision entstehenden Hadronen nicht voneinander unabhängig produziert werden. Darüber hinaus liefert die Korrelation zwischen den Vorwärts- und Rückwärtsmultiplizitäten Informationen über die longitudinale Ausdehnung der Teilchenquelle. Ein fundiertes Verständnis dieser Effekte im pp-System ist notwendig bevor ähnliche Studien in Kernstößen unternommen werden können.

In dieser Arbeit beschreibe ich eine für das ALICE-Experiment am CERN-LHC entwickelte Multiplizitätsanalyse der geladenen Teilchen. Die Analyse legt ihren Schwerpunkt auf Multiplizitätsverteilungen und Vorwärts-Rückwärts Multiplizitätskorrelationen und wurde ausführlich mit simulierten pp-Kollisionen getestet. Letztere wurden mit realistischen Eventgeneratoren produziert, die an die experimentellen Daten bei niedrigeren Energien angepasst und zu LHC extrapoliert wurden. Die Analyse und ihre Ergebnisse werden in den Kapiteln 4 und 5 beschrieben. Ein besonders wichtiger Punkt hier ist der Einfluss der ALICE-Detektoren auf die zu messenden Observablen.

Die Multiplizitätsanalyse basiert auf den in der ALICE Time Projection Chamber (TPC) gemessenen Teilchenspuren. Die TPC ist ein ausgezeichneter Detektor, der geladene Teilchen mit großer Akzeptanz und hoher Auflösung messen kann. Letztere ist jedoch nur erreichbar, wenn die Arbeitsbedingungen voll unter Kontrolle sind. Zwei wesentliche Parameter, die Elektrondriftgeschwindigkeit und die Gasverstärkung, werden durch ein spezielles Gerät, Gas prOportional cOunter For drIfting Electrons (GOOFIE), überwacht. Installation, Inbetriebnahme und Operation des GOOFIE, beschrieben im Kapitel 2.3, stellen den praktischen Teil dieser Doktorarbeit dar.

Chapter 1

Introduction

A prerequisite for studying nucleus-nucleus collisions is to understand the physical effects involved in high-energy hadron-hadron collisions. In particular, it is important to identify the genuine collective effects in AA (nucleus-nucleus) collisions and separate them from phenomena already present in proton-proton (pp) collisions [Ppr104]. Some of the questions for pp collisions are still not answered clearly, like the question of the existence of a scaling law for particle production, or the influence and origin of the already observed correlations.

The charged particle multiplicity is one of the simplest and most powerful observables in the studies of relativistic hadronic collisions. In particular, the multiplicity fluctuations and correlations between multiplicities observed in two different regions of phase space carry information about the reaction dynamics and the mechanism of particle production.

This work is centered on investigating these two points. In the next chapters, the existence of a scaling law for the multiplicity distribution at high energies will be discussed, and the contributions to multiplicity correlations will be analyzed. In order to establish a common ground for the discussion, we start by briefly introducing the existing classification of hadron-hadron collisions and the observables we can obtain from the multiplicity measurement.

1.1 Hadron-hadron collisions

Newton's concept of an elementary particle 'hard, impenetrable... as never to break in pieces' can only be applied to leptons. No collision involving electrons has lead to a decay of the type $e^* \rightarrow e\gamma$, where γ is a photon. The muon for instance is not an excited state of the electron [Gott84]. Leptons are subject to weak interaction and considered as 'elementary particles'. On the other hand, hadrons, like the proton, are composed of quarks and are affected by strong interactions as well.

A pattern that appears in hadron collisions at energies above 10 GeV is the signature for the existence of an inner structure, explained by point-like constituents (partons). In quantum chromodynamics (QCD) these are identified with quarks and gluons. Two hadrons can pass through each other with low amount of momentum transferred between, but a hard parton-parton collision results via a string fragmentation into a high number of final particles. The kinematics of these particles is commonly described in terms of variables inspired by special relativity. From the particle momentum in beam direction (longitudinal) $p_L = p_z$ and the energy of the particle E $=p_0$ the rapidity y of a particle can be calculated as [1]:

$$y = \frac{1}{2}\ln(\frac{p_0 + p_z}{p_0 - p_z}) \ . \tag{1.1}$$

If the particle is traveling close to the speed of light the pseudorapidity η is used instead:

$$\eta = -\ln[\tan(\frac{\theta}{2})] = \frac{1}{2}\ln(\frac{|p| + p_z}{|p| - p_z}) \ , \tag{1.2}$$

where θ is the angle with respect to the beam axis. For a speed close to the speed of light $|p| \approx p_0 = E$ and hence $\eta \approx y$. The pseudorapidity is easy to measure because it does not require the knowledge of the particle mass.

---

[1] Here $\hbar = c = 1$ in equations.

Hadron collision events can be divided [Wong94] in elastic, inelastic diffractive (single diffractive SD and double diffractive DD), and inelastic non-diffractive ND events. Inelastic diffractive events are those where a small number of particles is produced and where the momentum transfer is small. Among them we distinguish single diffractive events (SD), where only one beam particle is excited, resulting in a highly asymmetric rapidity distribution, and double diffractive events (DD), with both beam particles excited. Events with a large number of particles produced and a large momentum transfer are called inelastic non diffractive events (ND) (Fig. 1.1).

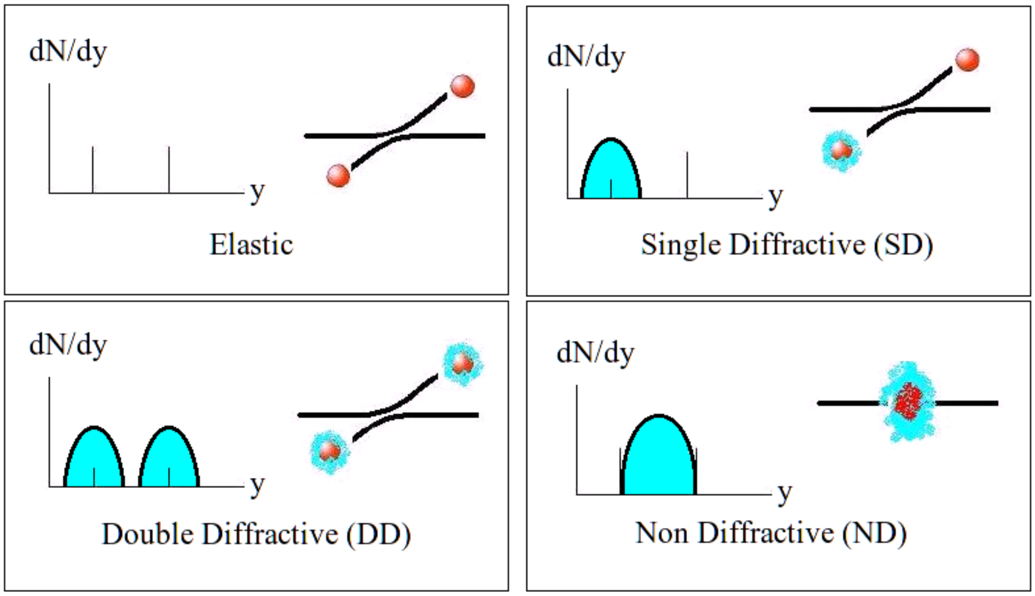

Figure 1.1: Collision types. In inelastic diffractive events, a small number of particles is produced and the momentum transfer is small. They are subdivided in single diffractive events (SD), where only one beam particle is excited, leading to a highly asymmetric rapidity distribution, and double diffractive events (DD), where both beam particles are excited. In inelastic non diffractive events (ND), large number of particles is produced and there is a large momentum transfer.

At the top LHC energy (14 TeV), the total pp cross section is 100 mb; the cross section for ND events is 60 mb, for SD events around 12 mb, and for DD of the same magnitude [Ppr104]. We define non single-diffractive events (NSD) as any inelastic hadron-hadron interaction that cannot be regarded as a single diffractive (SD) event.

According to the transverse momentum p_t of the produced charged particles, processes in which only particles are produced in the 'soft' p_t region ($p_t < 1$ or 2 GeV/c) and around mid-rapidity are called soft processes. They are associated with large length scales in QCD and require non-perturbative QCD calculations. In a collision, a process producing particles with high p_t's are called hard processes and they are treated with perturbative QCD and a parton-based model.

In this work, we will refer to data from e^+e^- collision, proton-proton (pp), and proton-antiproton ($p\overline{p}$) collision. When using antiprotons the additional annihilation energy is properly taken into account.

The total number of particles produced in a collision is defined as the multiplicity of the collision [Wong94]. In case of detectors that are only sensitive to charged particles, we speak of charged particle multiplicity. The multiplicity may be connected, under the scope of statistical mechanics, with the average number of particles of the grand canonical ensemble. Since each collision is a different process, we can define then a charged particle multiplicity distribution (MD), and for this an average charge particle multiplicity $\langle N_{ch} \rangle$.

The scaling of the cross section with the Feynman variable x_F and the previous experimental results supported the existence of a scaling in the MD [Koba72]. The Feynman variable x_F is defined as the ratio between the longitudinal momentum of the particle in the center-of-mass system and the maximum possible momentum for the particle in the given reaction. This scaling hypothesis accounts for including multiplicity distributions for several different types of collisions, e^+e^- annihilation [Carr83], but it turns out to be only approximately valid for higher energies [Kian85]. From the fluctuations of the charged particle multiplicity distribution we expect to learn about the validity (or not) of the Feynman scaling.

Forward-backward (FB) multiplicity correlations appear to be also a sensitive probe for the different models that describe hadron collisions. Below we will discuss one by one the mean multiplicity, the multiplicity fluctuations, and the forward-backward multiplicity correlations.

1.2 Mean charged particle multiplicity

To understand the nature of a collision we first study the dependence of the average number of charged particles on the center of mass energy $\sqrt{s}$. An experimental parametrization of this dependence reads [Kitt04]:

$$\langle N_{ch} \rangle = a_0 + a_1 \ln \sqrt{s} + a_2 (\ln \sqrt{s})^2 \ , \tag{1.3}$$

where $\sqrt{s}$ is the total energy of the collision system in its center-of-mass reference frame, and a_0, a_1 and a_2 are constants. This formula is sometimes written using $\ln s$ instead of $\ln \sqrt{s}$ and the extra factor $\frac{1}{2}$ stored in the constants. A linear dependence of $\langle N_{ch} \rangle$ on $\ln s$ is motivated by the Fermi scaling [Wong94]. The parametrization works reasonably well, albeit with different constants, for pp and AA collisions from several GeV to the highest analyzed energies (Fig. 1.2).

The quadratic term, starting to dominate at higher energies, reflects the contribution of hard processes. Up to now, it is impossible to derive any of these parametrizations from the QCD Lagrangian [Ppr104].

1.3 Charged particle multiplicity fluctuations

The multiplicity fluctuations can be quantified by the scaled variance ω_{ch} as in statistical mechanics:

$$\omega_{ch} = \frac{< N_{ch}^2 > - < N_{ch} >^2}{< N_{ch} >} = \frac{\sigma_{ch}^2}{\mu_{ch}} = \frac{D^2}{\mu_{ch}} = \frac{var(N_{ch})}{\mu_{ch}} \ , \tag{1.4}$$

where N_{ch} is the charged particle multiplicity, $\sigma_{ch}^2 = D^2 = var(N_{ch})$ the variance of the multiplicity, and $\mu_{ch} = \langle N_{ch} \rangle$ the mean multiplicity [Adar08]. The formula 1.4 also shows the different types of notation in use for the variance.

The multiplicity distributions in hadron collisions up to $\sqrt{s} = 30$ GeV show an universal shape when scaled properly [Koba72]. In the following, for simplicity, we set $\langle N_{ch} \rangle \equiv \langle n \rangle$. We define $P_n(s)$ as the probability that

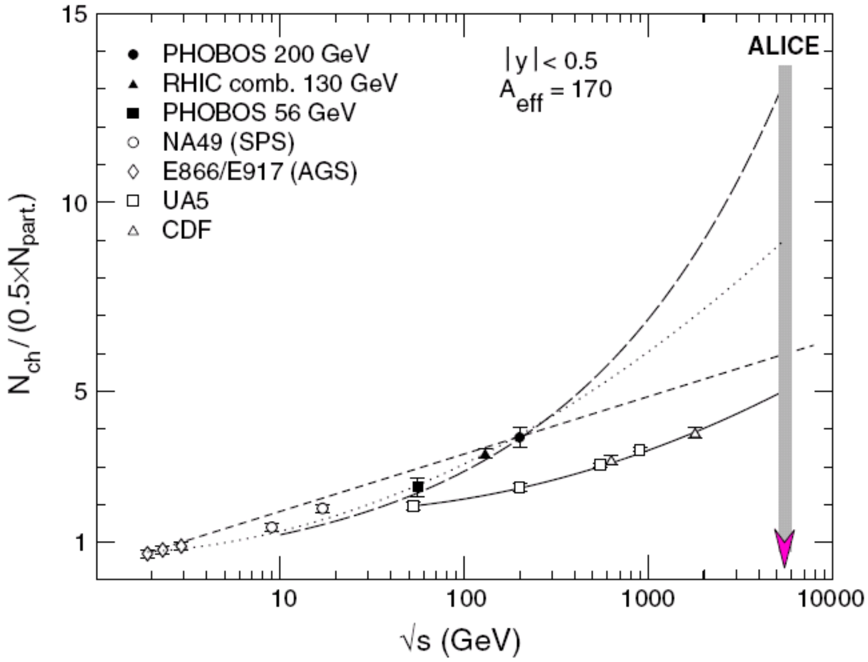

Figure 1.2: Charged particle rapidity density per participant pair as a function of center-of-mass energy for AA and pp collisions. The general parametrization 1.3 is displayed as dotted, dashed, and solid curves. Experimental data for $p\overline{p}$ collisions ($N_{part} = 2$) are well described by the solid line. For AA collisions the three dashed lines represent the range allowed by the fit and demonstrate the uncertainty when extrapolating to LHC energies [Ppr104].

a collision at $\sqrt{s}$ has a multiplicity n. Then, the quantity $P_n(s)$ can be expressed as a function of the variable $z = n/\langle n\rangle$ as follows:

$$P_n(s) = \frac{1}{\langle n\rangle}\Psi\left(\frac{n}{\langle n\rangle}\right) = \frac{\sigma_n(s)}{\sigma_{total}(s)} \ . \tag{1.5}$$

The scaled multiplicity $z = n/\langle n\rangle$, is called the KNO scaling variable after the authors (Z. Koba, H. B. Nielsen and P. Olesen [Koba72]). The function $\Psi(z)$, independent of $\sqrt{s}$ and depending only on z, is called the KNO function.

The KNO scaling applies to a given collision system and energy. In Fig. 1.3, we show a KNO scaling for neutral pions from e^+e^- collisions at various energies [Kras99]. The solid line is the so called shifted Krasznovszky-Wagner (KW) distribution [Kras92], which has the form:

$$P_n(s) = \frac{2m}{\langle n\rangle\,\Gamma(A)}F^A(A)z^{mA-a}exp[-F(A)z^m] \ , \tag{1.6}$$

where z is the scaled multiplicity. The expression for $F(A)$ is:

$$F(A) = \frac{\Gamma^m(A+\frac{1}{m})}{\Gamma^m(A)} \ , \tag{1.7}$$

where A and $\langle n\rangle$ are fitting parameters that depend on energy and m is a constant set according to the collision type (e^+e^-, $p\bar{p}$, etc). The KW distribution is including, as special cases, many of the classical distributions, e.g. the exponential, the half-normal, the gamma [Bial85], the geometrical [Chou83], the chi-square, etc. [Kras92].

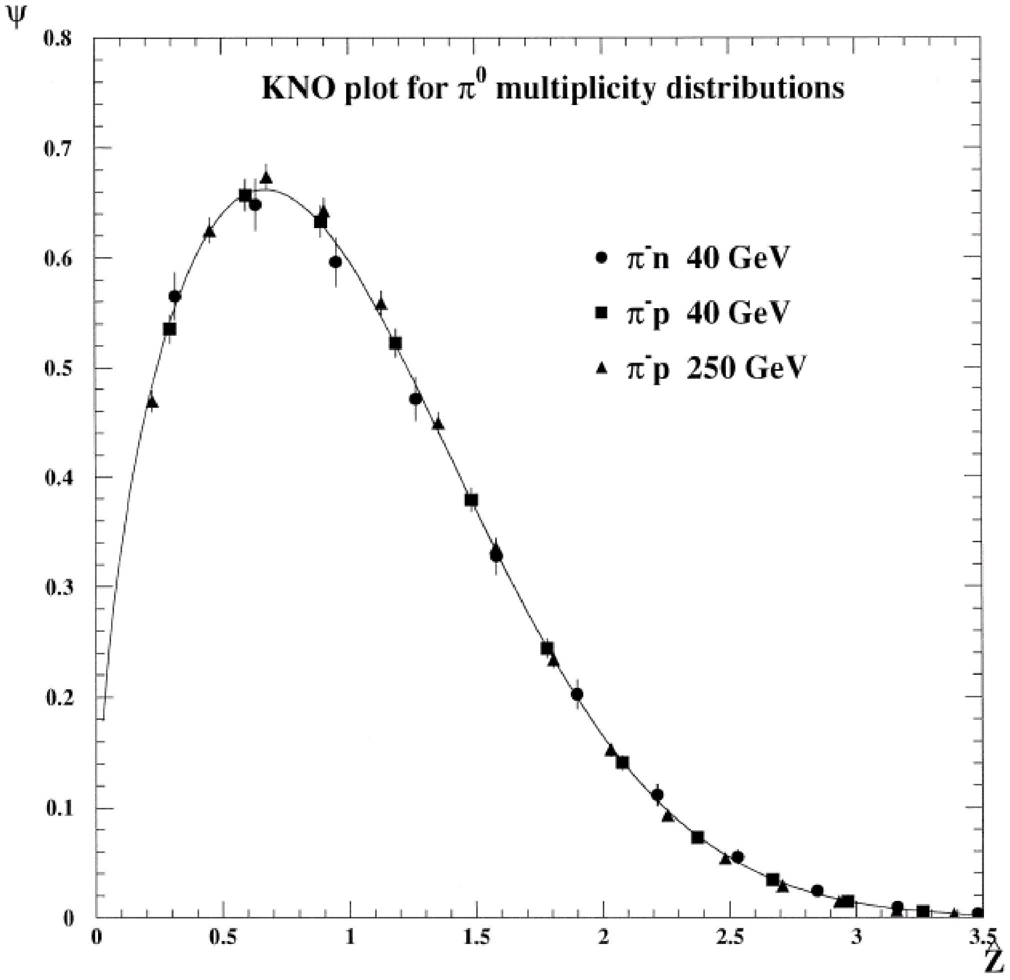

Figure 1.3: KNO plot for π^0 multiplicity distributions. The KNO function is $\Psi(z, s) = \langle n \rangle P_n(s)$, where $P_n(s)$ is the probability that a collision at $\sqrt{s}$ has a multiplicity n. $P_n(s)$ is a shifted Krasznovszky-Wagner KW distribution. The scaled multiplicity $z = n/\langle n \rangle$ is the KNO scaling variable. The 40 GeV data comes from the Dubna 2 m propane bubble chamber, considering 20% mean efficiency; the 250 GeV data are from the E-234 15-ft bubble chamber. Figure taken from [Diam84].

The KNO scaling seems not to hold for the total charged particle multiplicity distribution (i.e, no distinction among different particle productions). The increasing number of produced species with increasing collision energy results in a deviation of a KNO scaling of the total MD [Alne85, Sarc87] and triggered a search for a general MD function.

A good candidate for an universal parametrization is the negative binomial distribution (NB, also named Pascal distribution), found to describe the MD in cosmic ray observations in the '60s, and later applied to fit MD of charged particles for proton-proton collisions from 5 to 100 GeV and e^+e^- annihilation up to 40 GeV [Ugoc05]. It is a two-parameter distribution given by:

$$P_n(\langle n\rangle, k) = \frac{k*(k+1)...(k+n-1)}{n!}\frac{\langle n\rangle^n * k^k}{(\langle n\rangle + k)^{n+k}} \; , \tag{1.8}$$

where $\langle n\rangle$ is the average multiplicity, and k is the number of the contributing phase space cells. The contribution of a cell is equivalent to the one given by an abstract harmonic oscillator [Carr83].

The resulting particle emission model is known as the cell model. The k phase space cells emit particles independently. Originally, a cell was emitting particles following the Bose-Einstein probabilities. Alternatively, the cells may be identified with clusters, jets, etc., each one contributing with a stochastic emission and a coherent component on account for deviations from a pure (Poissonian) emission depending of the noise/signal parameter. In this model, a zero noise/signal parameter gives a pure Poisson emission. This description allows to explain experimental MD in the case of hadron-hadron collision as the sum of several cells affected by the noise/signal parameter (Fig. 1.4).

The number of cells can be linked with the deviation of the variance D^2 of the distribution from the Poissonian one. Two limits are important in this discussion:

- $D^2 = \langle n\rangle$ (that is, $k \longrightarrow \infty$), corresponds to a Poissonian distribution, independent particle production.

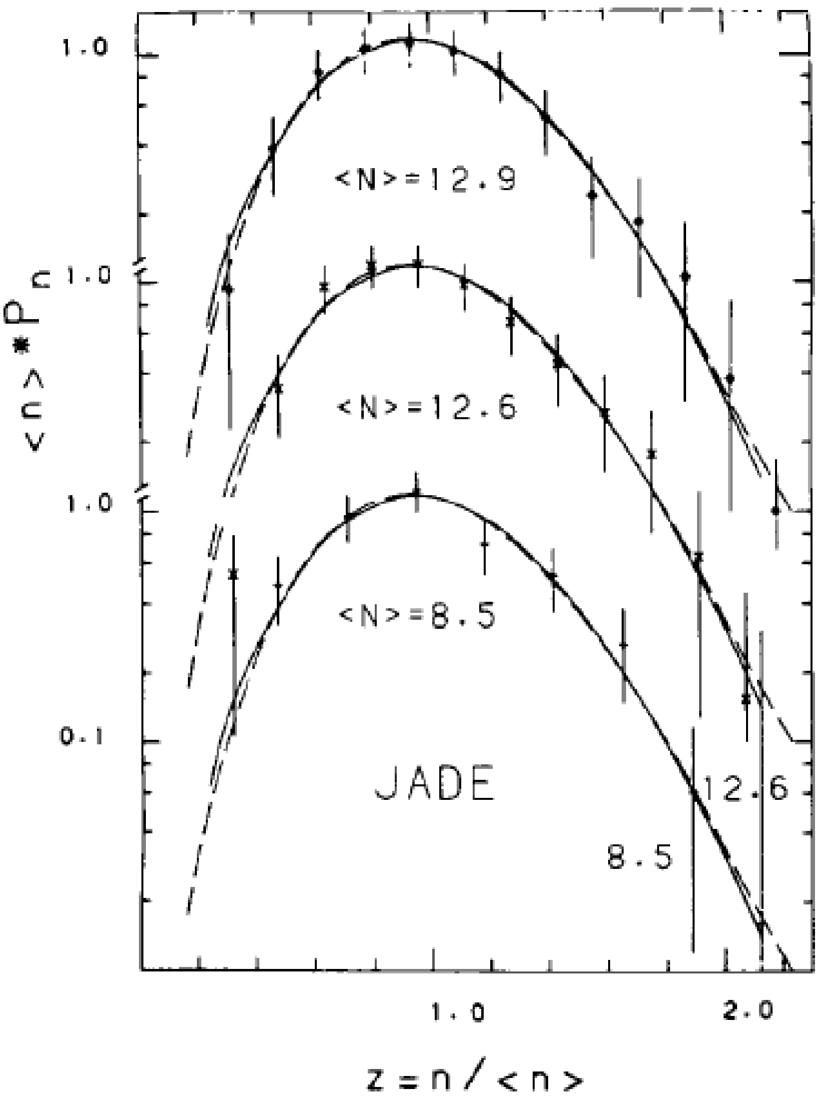

Figure 1.4: JADE multiplicity data (12, 30 and 35 GeV) expressed in KNO variables, compared with a two-cell model fit. Each cell is emitting following a Poisson distribution. The solid curve (dashed curve) is for $\overline{n} = 8.5$ (12.6) and an noise/signal parameter m = 0 (0.2). The noise/signal describes the deviation for a Poisson (independent) emission [Carr83].

- $D^2 = \langle n \rangle + \langle n \rangle^2$ ($k = 1$), the so called geometric distribution.

In terms of NB distributions, KNO scaling is holding if $1/\langle n \rangle + 1/k$ is independent of energy.

At an energy of 540 GeV, like the data published by the UA5 collaboration for pp collisions, the width of the scaled MD increases as the studied rapidity interval gets smaller for inelastic, non single-diffractive (NSD) events. That is, the relative number of large fluctuation events increases for smaller rapidity windows, breaking the scaling in the central region [Alne85].

But the complex observed structures may have a simple origin. This simplicity should manifest itself in terms of regularities in final particle multiplicity distributions [Ugoc05]. The deviation from the scaling at 900 GeV was attributed to an increasing contribution of events with jets, called semi-hard events. UA5 MDs are successfully described (see Fig. 1.5) by adding weighted contributions of soft (events without jets) and semi-hard events, each one described by a NB distribution.

The interpretation of these two separate behaviors is done inside the clan structure analysis. The 'soft' part is following the KNO scaling and the 'semi-hard' part is not. A clan is understood as a group of particles of common ancestry. Clans are independently produced in a number that follows the Poisson MD. Each clan contains at least one particle by assumption and all correlations remain inside a clan (the word is directly taken from the Scottish sense for it). Clan ancestors generate additional particles via cascading, according to a logarithmic multiplicity distribution [Ugoc05]. More important, there is a link between the clan structure analysis and the standard NB. We define $\bar{N}$ as the average number of clans, and $\bar{n_c}$ the average number of particles per clan. Then:

$$\bar{N} = k \ln\left(1 + \bar{n}/k\right) \quad \text{and} \quad \bar{n_c} = \bar{n}/\bar{N} \ , \tag{1.9}$$

where $\bar{n} \equiv \langle n \rangle$ is the average multiplicity of the NB and k is the number of contributing cells of the given NB.

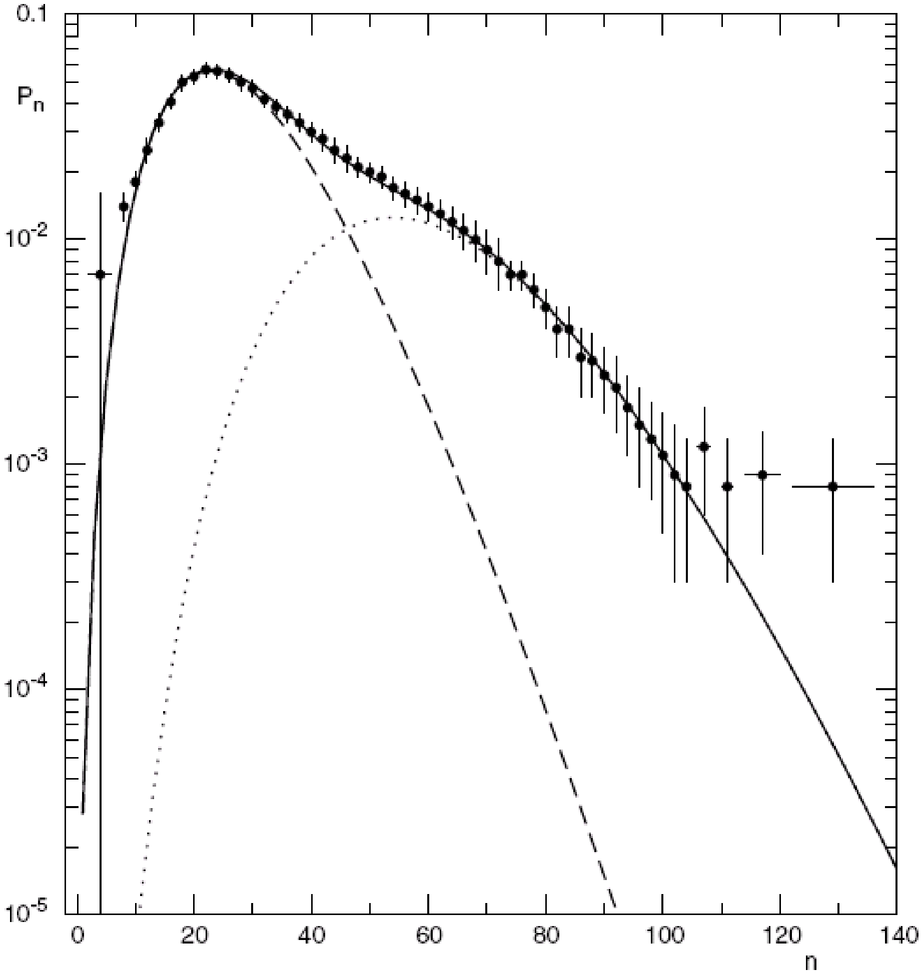

Figure 1.5: Charged particle multiplicity at $\sqrt{s} = 900$ GeV for the UA5 Collaboration. The shoulder structure represents a violation of the KNO scaling. The fit (solid line) is the result of the contribution of the superposition of two different negative binomial (dashed and dotted) distributions [Ugoc05].

The total MD can be therefore described as the superposition of two NB: one for the contribution of the soft events and another NB from the contribution of the semi-hard events. Each NB is described by an average number of clans $\bar{N}$ and an average number of particles per clan $\bar{n_c}$. All correlations are supposed to remain within a clan, so forward-backward (FB) correlations can be explained also, by adding the correlation strength contributions from both NB (soft and semi-hard).

1.4 Charged particle multiplicity correlations

We can define two pseudorapidity regions and evaluate for each event a forward pseudorapidity multiplicity n_F and a backward pseudorapidity multiplicity n_B. Correlations between n_F and n_B are the subject of this section. Depending on the gap between the two regions we can distinguish short-range ($|\eta| < 1.0$) and long range correlations.

Theoretically the existence of forward-backward (FB) correlations is supported by the predictions from the Dual Parton Model (DPM) and the Parton String Model (PSM). Short-range FB correlations are associated with cluster decays, resonance decays, or jet correlations [Tarn08, Foa75, Xu86]. The presence of one particle at a certain pseudorapidity favors the production of other particles in the same pseudorapidity region. The short-range correlations due to cluster formation and decays are energy-independent [Foa75]. Both effects will result in a positive correlation.

Long-range FB charged particle multiplicity correlations are a signature of multiple partonic interactions (MPI) according to the parton model for hard collisions and the hadron model for soft collisions. The overlapping independent emission model (OIE) is predicting a strong reduction of long-range correlations if a certain multiplicity range (sub-sample) is selected [Bene78]. This allows us to get rid of long-range correlations to study only the contribution of short-range correlations. Correlations in a wide pseudorapidity range are considered in heavy ion collision as a probe, free from final state effects, of the early stage of the collision [Tarn08].

Experimentally, the correlation strength can be quantified by the slope of the linear fit of the scatter plot of the forward charged particle multiplicity n_F versus the backward charged particle multiplicity n_B:

$$\langle n_B \rangle (n_F) = a + b * n_F \; . \tag{1.10}$$

The correlation strength b has been extensively studied in hadron-hadron collisions as in e^+e^- annihilation and was found to be positive [Tarn08, Foa75, Bene76]. An example of a FB correlation plot obtained with the PYTHIA event generator, is shown in the left panel of Fig. 1.6. The two pseudorapidity windows have a width of 0.2 units and are centered at $\eta = \pm 0.5$ ($\Delta\eta = 1.0$). The corresponding fit is shown in the right panel of this figure. A more detailed description of this method will be given in Section 4.1 and a discussion in Section 5.4.

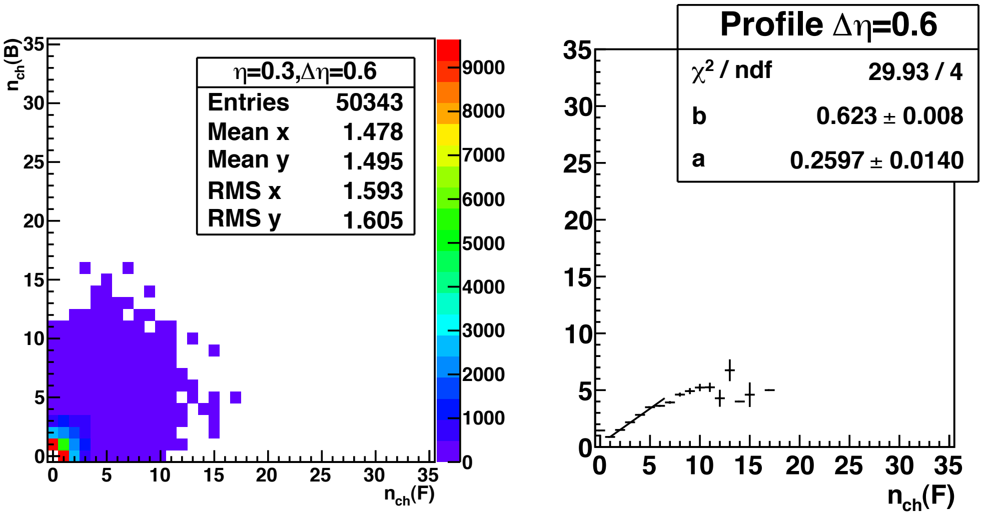

Figure 1.6: An example of a two-dimensional plot of $\langle n_B \rangle (n_F)$ as a function of n_F for pseudorapidity windows of $(\eta_1 - \eta_2) = 0.2$, centered in $\eta = 0.3$, separated in total by $\Delta\eta = 0.6$ pseudorapidity units, for ALICE energy $\sqrt{s} = 10$ TeV. Left panel: scatter plot of n_B vs n_F. Right: linear fit of the projection of it. It shows the obtained correlation strength b for the applied settings.

The UA5 Collaboration at the CERN $p\bar{p}$ collider at 546 GeV c.m. energy measured the relation between the average number of charged particles in the backward hemisphere and in the forward one. This relation was very well approximated by Eq. 1.10 [Ugoc01]. The study, performed in the pseudorapidity interval $1 < |\eta| < 4$ to remove short-range correlations, found $b = 0.43 \pm 0.01$. This value is much higher than at lower energies e.g. $b = 0.156 \pm 0.013$ at $\sqrt{s} = 63$ GeV. Assuming uncorrelated random particle emission in the selected pseudorapidity region, the shape of the n_F multiplicity distribution at fixed full multiplicity $n = n_B + n_F$ is binomial with a probability $p = 1/2$ for a particle of the full sample, n, to fall in the backward or forward hemisphere, and a resulting variance $d^2_{n_F} = p(1-p)n = n/4$. The experimental dispersion of the full distribution in the above mentioned pseudorapidity interval and the average multiplicity lead to $b = 0.69$, a much higher value than the experimental one ($b = 0.43 \pm 0.01$). However, the UA5 Collaboration claimed a reasonable agreement with experimental data by considering that not particles but particle clusters are binomially distributed in both hemispheres and that the decay products of each cluster remain in the same hemisphere [Ugoc01]. In this statistical model [Xu86] (inheriting from the 'cell model' defined in 1.3) each cluster decays approximately in 2 particles (for the UA5 energy). The cluster model explains successfully the measured FB correlations for UA5 proton-antiproton collision at an energy of $\sqrt{s} = 540$ GeV in the three 'rapidity regions' (see Fig. 1.7).

The cluster model fails when the energy range is increased and the rapidity windows are decreased. It has been found that there was an unexplained correlation left, visible also as a 'shoulder' in the multiplicity distribution (Fig. 1.5 in the previous section). In Fig. 1.8 we see how the 'cluster model' is not able to predict the measured correlation for the $1 < |\eta| < 4$ window [Xu86].

Predictions using a superposition of two NB that fitted UA5 MD for $\sqrt{s} = 900$ GeV (see 1.3) are also in good agreement with the measured FB multiplicity correlations $\langle n_B \rangle (n_F)$. This is shown in Fig. 1.9 (right panel). The events were divided into two categories: events with jets (called 'semi-hard') and without jets (labeled 'soft') [Ugoc05].

Figures 1.9 and 1.5 tell us that MD fluctuations and FB correlations could be described using a superposition of two NB. The physical picture of this scenario is that it is possible to divide the MD into two contributions, one that accounts for events with jets (semi-hard), and one 'soft' for non-jet events.

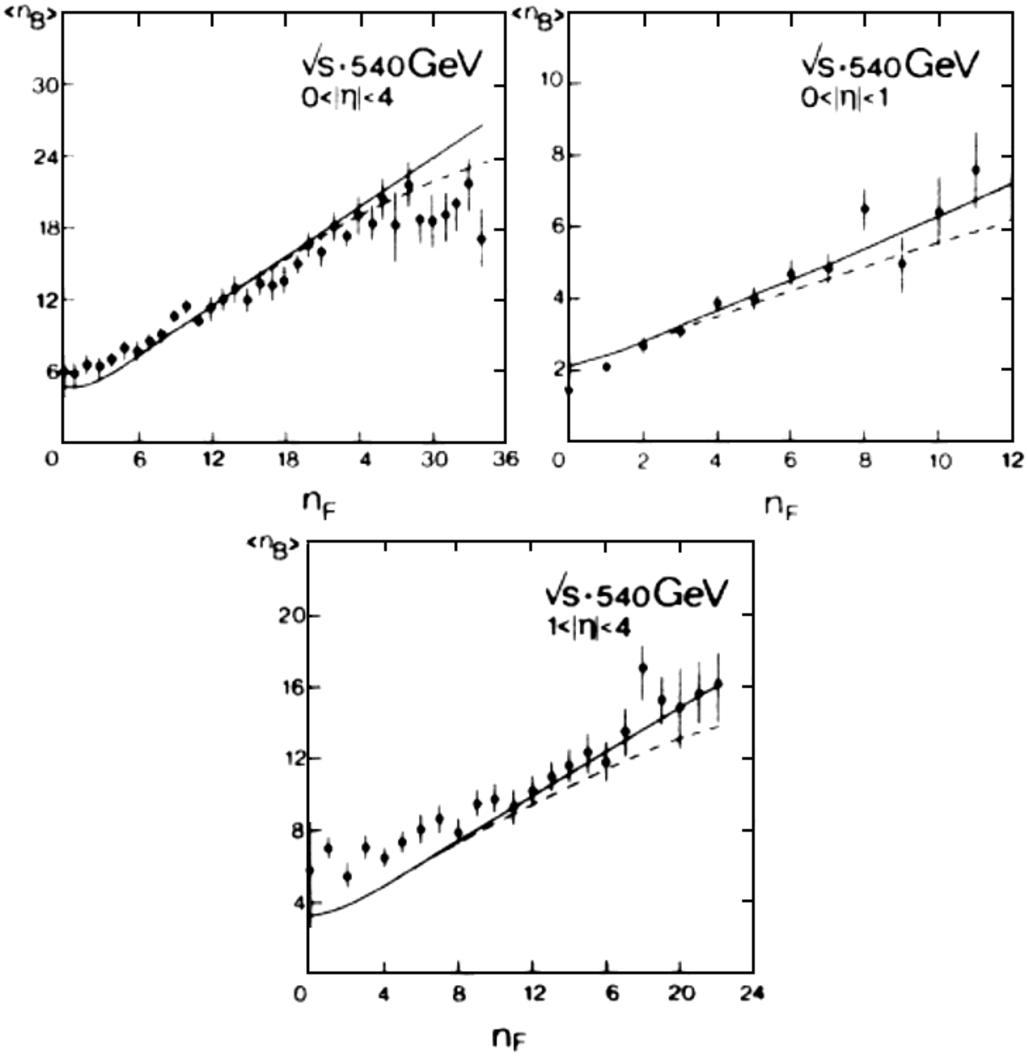

Figure 1.7: The dependence of $\langle n_B \rangle (n_F)$, the average charged multiplicity in the forward region as a function of the backward region, for three different pseudorapidity intervals for $\sqrt{s} = 540$ MeV. The dashed curve corresponds to the calculations in an hadronic cluster approach with the multiplicity distribution normalized up to the last measured point (largest multiplicity in the rapidity window). The solid line is without this normalization [Xu86].

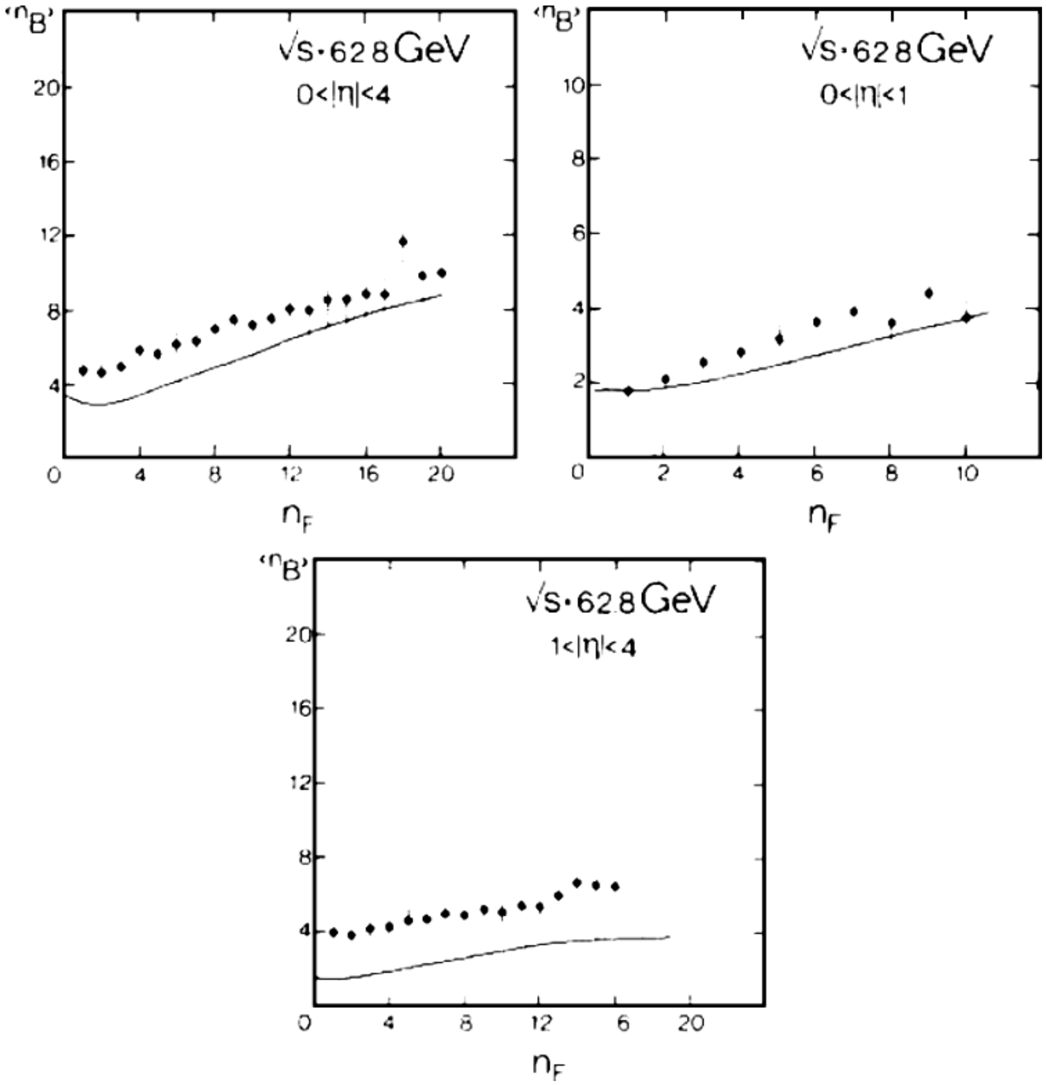

Figure 1.8: The dependence of $\langle n_B \rangle (n_F)$ for three different pseudorapidity intervals for the highest CERN ISR energy $\sqrt{s} = 62.8$ GeV. The solid line corresponds to the calculation following an hadronic cluster approach, considering three pseudorapidity regions ('central', 'projectile' and 'target'). Discrepancies for the region $1 < |\eta| < 4$ are attributed to a miscalculation of the contribution of one of these regions for the given energy (see [Xu86]).

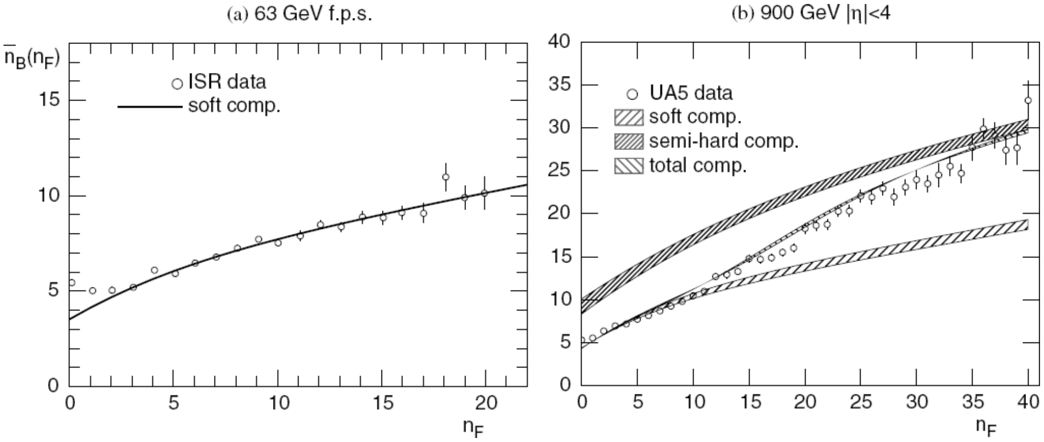

Figure 1.9: Weighted superposition model predictions for $\langle n_B \rangle (n_F)$ as a function of n_F compared with experimental data. (a) Full phase-space at CERN ISR energy $\sqrt{s} = 63$ GeV (b) Pseudo-rapidity interval of $|\eta| < 4$ at $\sqrt{s} = 900$ GeV. The model includes two components on account of two type of events, one 'semi-hard' for events with jets, and one 'soft' for the rest (from [Ugoc05]).

Each contribution follows an NB distribution, and each NB is characterized by a specific number of emitting cells. By applying a clan structure analysis in each NB, the number of emitting cells and the average number of particles emitted per cell is obtained. These two parameters (number of emitting cells and the average number of particles emitted per cell) can be used then to verify the breaking of KNO scaling in the high energy region, or to explain the FB multiplicity correlations. This approach will be chosen for understanding the output of the analysis performed in this work.

Chapter 2

The ALICE experiment

ALICE (A Large Ion Collider Experiment) is the dedicated heavy ion experiment conceived to investigate the physics of strongly interacting matter at extreme values of energy, density and temperature in nucleus-nucleus collisions, including a possible transition to quark-gluon plasma (QGP). It is located at the interaction point 2 (IP2) of the Large Hadron Collider (LHC) [Pott96]. The detector is designed to cope with the extreme particle multiplicities anticipated for Pb-Pb reactions (up to $\mathrm{d}N_{ch}/\mathrm{d}y = 8000$). It has been built by a collaboration of more than 1000 physicists and engineers from 105 institutes in 30 countries. Its total dimensions are $16 \times 16 \times 26$ m^3 with a total weight of approximately 10 000 t.

ALICE will address heavy ion reaction dynamics via studies of multiplicities, invariant mass spectra, two-particle correlations, and collective flow. The properties of the QGP will be studied using heavy flavors, photons, and jets. The QCD phase transition will be investigated by hadron abundances and by charge fluctuations. The QCD matter studies will be complemented by measurements of systems of lighter ions and of pp collisions. The pp data are needed as a reference for nuclear collisions, on one hand, and address interesting aspects of hadron collisions on the other. The multiplicity analysis presented in this work is an example for the latter.

2.1 Experimental setup

The setup of the ALICE experiment is shown in Fig. 2.1. A solenoid magnet of an internal length of 12.1 m and a radius of 5.75 m, inherited from the L3 experiment at LEP, reaches a field of 0.5 T at the nominal current of 30 kA with a field uniformity better than 2%. The magnet holds the full acceptance central barrel detectors, the Inner Tracking System (ITS), the Time Projection Chamber (TPC), the Transition Radiation Detector (TRD) and the Time Of Flight (TOF). Not covering the full acceptance, one finds the High-Momentum Particle Identification Detector (HMPID) and the PHOton Spectrometer (PHOS)[Int07].

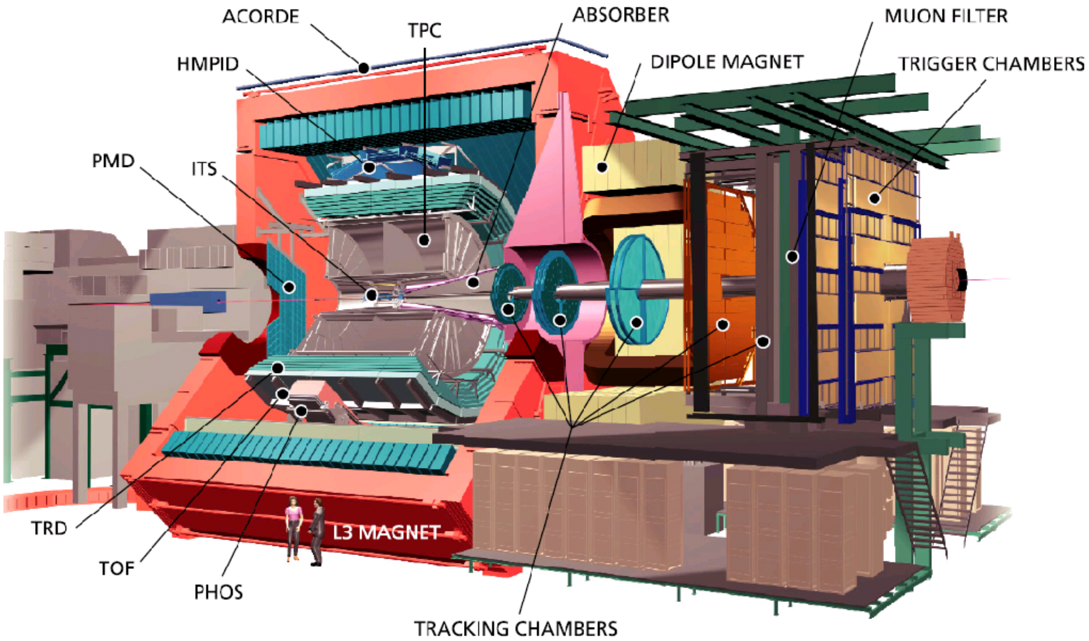

Figure 2.1: The ALICE experiment setup at the CERN LHC. The position of the different detectors is shown. A description of each detector is given in the text.

The Inner Tracking System (ITS) is aimed to localize the primary vertex with a resolution better than 100 μm, to reconstruct the secondary vertices from the decays of hyperons and D and B mesons, to track and identify particles with momentum below 200 MeV/c, and to improve the momentum and angle resolution for particles reconstructed by the TPC. It is composed of six cylindrical layers of (two pixel, two drift, and two strip) detectors, located at radii between 4 and 43 cm, with a resolution in the bending plane of $r\Delta\phi = 12 - 35$ μm. The rapidity coverage is $|\eta| < 0.9$ for all vertices located within the length of the interaction diamond ($\sigma = 5.3$ cm along the beam direction). ITS is also capable of particle identification via $\frac{dE}{dx}$, since the four outer layers have analogue readout. The overall thickness of the ITS is 8% X_0. The expected total radiation dose for the inner layer is 270 krad.

The Time Projection Chamber (TPC) is the main tracking detector of the central barrel. It is a large drift chamber that allows for charged-particle momentum measurements with good momentum resolution, two-track separation, particle identification, and vertex determination. Since this work will be centered on the TPC capabilities for multiplicity studies, it will be described in more detail in a separate section.

The Transition Radiation Detector (TRD) will be responsible for electron identification in the central barrel for momenta above 1 GeV/c. X-rays, produced by the passage of electrons through a 4.8 cm thick polypropylene fiber radiator, are detected in drift chambers with pad readout filled with Xe/CO_2 gas mixture. X-rays and the 30% higher $\frac{dE}{dx}$ of electrons provide the basis to distinguish them from pions. With six layers of radiator/readout chamber modules the pion rejection factor is 100. The TRD provides also a fast trigger (6.5 μs) for charged particles with high momentum. In a standalone mode, the TRD is reaching a momentum resolution of 3.5-4.7% at 5 GeV/c. In conjunction with the ITS and the TPC, the TRD is able to measure light and heavy vector-meson resonances and the dilepton continuum in pp and Pb-Pb collisions, and thanks to the excellent impact parameter resolution of the ITS to reconstruct open charm and open beauty in semi-leptonic decays. The TRD radiation thickness is 23% X_0.

The Time Of Flight (TOF) detector is based on the Multigap Resistive Plate Chamber (MRPC) technology. It makes particle identification available in the intermediate p_t-region below about 2.5 GeV/c for pions and kaons, up to 4 GeV/c for protons, with a p/K and K/p separation better than 3 σ. The intrinsic time resolution is about 40 ps and the efficiency close to 100%. Its total area is 140 m^2. The TOF radiation thickness is 30% X_0.

The High-Momentum Particle Identification Detector (HMPID) is a proximity focusing Ring Imaging Cherenkov Detector (RICH) using as a radiator a 15 mm thick layer of low chromaticity C_6F_{14} (perfluorohexane) liquid with an index of refraction of n = 1.30 at λ= 175 nm, corresponding to $\beta_{\mathrm{min}} = 0.77$. The radiator defines the momentum range covered by the HMPID. The HMPID is dedicated to inclusive measurements of identified hadrons at $p_t > 1$ GeV/c, extending within 5% of the central barrel acceptance, the range for p/K and K/p discrimination up to 3 GeV/c and 5 GeV/c, respectively. Identification of light nuclei and anti-nuclei (d, t, 3He, α) at high transverse momenta in the central rapidity region can be performed as well. Cherenkov photons are detected by multiwire proportional chambers (MWPC's) with CsI coated pads.

The PHOton Spectrometer (PHOS) is a single-arm high-resolution electromagnetic calorimeter made with lead tungstate crystals for low p_t direct photon measurements and for studies of jet quenching (interaction of energetic partons with dense matter) through the measurement of high-p_t π^0 and γ-jet correlations. The high-energy resolution and granularity is possible by using a dense scintillator material (lead-tungstate, $PbWO_4$) of 20 X_0 with high photo-electron yield, allowing a two-photon invariant mass resolution at the π^0 peak of 3.5%. The time resolution is 2 ns at energies above 1.5 GeV, thanks to a fast scintillator and preamplifier. A charged-particle veto (CPV) of 99% efficiency is performed via a MWPC with pad readout, placed 5 mm before the calorimeter. The material budget is less than 5% of X_0.

A cylindrical Pb-scintillator ElectroMagnetic Calorimeter (EMCal) will be placed inside the L3 magnet at a radius of 4.5 m. The construction of it began in 2008. It will enhance the existing capabilities of ALICE to study the physics of jet quenching over the large kinematic range accessible in heavy-ion collisions at the LHC. It covers $|\eta| < 0.7$ and $\Delta\phi = 107^{\mathrm{o}}$ and is positioned opposite in azimuth from PHOS. The EMCal radiation thickness is 20% X_0.

ACORDE is an array of plastic scintillator counters on the upper surface of the L3 magnet. Its pseudorapidity and ϕ coverage are $-1.3 < \eta < 1.3$ and $-60^{\mathrm{o}} < \phi < 60^{\mathrm{o}}$. It is used in combination with TPC, TRD and TOF to detect single atmospheric muons and multi-muon events (so-called muon bundles) for the study of high-energy cosmic rays in the energy region of the knee in the cosmic ray spectrum. The ALICE tracking detectors are commissioned, calibrated, and aligned using cosmic rays triggered by ACORDE fast (Level-0) trigger.

The Muon Spectrometer is composed of a steel absorber, a dipole magnet with 0.67 T and 3 Tm, and 10 detection planes with a resolution of 70 μm. It covers $-4.0 < \eta < -2.5$ and it addresses the muon decay channel of the heavy quarkonia J/ψ, ψ', Υ, Υ', Υ''. The minimum muon momentum is 4 GeV/c and the system invariant mass resolution is 1% at 10 GeV/c^2.

In addition to the mentioned subdetectors, ALICE has two Zero Degree Calorimeters (ZDC) for centrality and reaction plane angle measurements, a Photon Multiplicity Detector (PMD) for γ and charged particle measurement within $2.3 < \eta < 3.7$, a Forward Multiplicity Detector (FMD) covering $-3.4 < \eta < -1.7$ and $1.7 < \eta < 5.0$, two vertex detectors (V0A and V0C) for interaction trigger, and two TOF start detectors T0 with a resolution of 50 ps which also provide the longitudinal event vertex position within 1.5 cm.

ALICE will be able to perform fast online processing and provide trigger for rare signals and/or data compression on the fly, using its High-Level Trigger (HLT) computer farm, consisting of 1000 multiprocessor machines.

All installed detectors participated in cosmic ray data taking in 2008. The TRD signal was also already used for triggering. For the TPC there is already a calibration from the combined methods. First sets of calibration were successfully performed from these measurements for the TPC.

2.2 The ALICE Time Projection Chamber

The ALICE Time Projection Chamber (TPC) (Fig. 2.2), placed inside the L3 magnet (Fig. 2.1), is the main tracking detector of ALICE, with capabilities of track finding, momentum measurement and particle identification via specific energy loss (dE/dx). It is the biggest TPC ever built, having as inner and outer radii respectively r = 0.85 m and R = 2.47 m, a total length of L = 5 m, making a total active volume of 90 m^3, and a 3% X_0 thickness [Alme10].

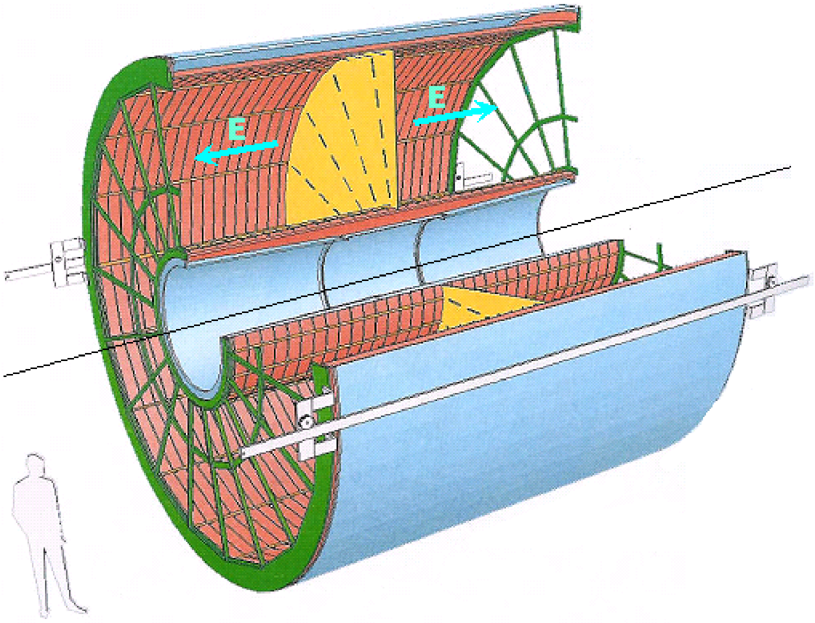

Figure 2.2: Schematic picture of the ALICE TPC. Inner and outer cylinders, the layout of the supporting wheels for the inner and outer chambers, and the central electrode are visible. The direction of the electric field is along beam pipe direction marked as a thin black line in the center of the cylinder. The magnetic field is aligned with the cylinder axis as well.

The active volume is filled with a special gas mixture Ne-CO_2-N_2 (90/10/5) and it is divided in two halves by a central electrode. The ionization electrons drift parallel to the cylinder axis over a distance of up to 2.5 m on either side of the central electrode to the end plates. The applied drift potential is 100 kV, resulting in an unprecedented field of E= 400 V/cm, and a drift velocity of around 2.7 cm/μs.

Trapezoidal multi-wire proportional chambers with cathode pad readout are mounted at each end plate. The TPC pseudorapidity coverage is $-0.9 < \eta < 0.9$ for tracks with full length and $|\eta| < 1.5$ for short tracks, the azimuthal coverage is 2π and the p_t detection range is 0.1-100 GeV/c. For Pb-Pb collisions, the TPC is designed to cope with collision rates up to 300 Hz. This collision rate is limited by the detector performance, since above this rate the space charge due to the ion feed-back during gate-open time is expected to be comparable to the space charge due to the ionization in the TPC drift volume, leading to tracking distortions of the order a few mm.

For pp collisions, the TPC is expected to deal with trigger rates of up to 1 kHz. The TPC specifications include a position resolution in the bending plane ($r\phi$) of 800-1100 μm and a $\frac{dE}{dx}$ resolution of 5.0-6.8% depending on the multiplicity. In a high particle multiplicity regime (dN/dy = 8000), a momentum resolution of Δp/p = 1 % and an energy loss resolution dE/dx= 5-7% are expected. The occupancy for central Pb-Pb collision at the inner part will be 40% (15% outer) and the two-track resolution allows to measure track pairs with Δp of less than 5 MeV/c (with B=0.5 T) [Tdr01, Gar04, Wie04].

Neon was chosen instead of argon because of its higher mobility, important to reach a good momentum resolution in high multiplicity environment. The CO_2 was taken as a quencher. Other typical hydrocarbon-based quenchers were rejected because of aging effects over the anode wire, safety regulations, or production of thermal neutrons. The widely used P10 gas mixture was discarded because of an undesirable dramatic gain degradation effect [Anto07]. It was proven [Gar06] that by adding a small percentage of N_2, the risks of self-sustained glow discharge was substantially reduced due to the absorption of electrons by N_2, without reducing the drift velocity [Anto07]. Since under normal working conditions the drift velocity has an strong dependence of gas temperature, a thermal stability with $\Delta T \approx 0.1$ K for the TPC in the drift volume is required. The CO_2 and N_2 fractions must remain constant with a 0.1% margin to ensure stable drift velocity and gas gain of the readout chambers. The O_2 can be maintained around 1 ppm or lower resulting in a signal reduction due to attachment of less than 5% for the maximum drift length of 2.5 m.

After completing installation of the front-end electronics, the TPC underwent a thorough pre-commissioning phase with cosmic rays and laser tracks for most of the year including the complete read-out chain, HLT, detector control and gas system. The technical design report specifications were reached or even surpassed; in particular, a signal-to-noise ratio for MIP better than 20:1 in the case of small pads in inner sectors and 30:1 for larger pads in outer sectors, close to the theoretical limit, was reached [Tdr01].

In January 2007, the TPC was lowered into the pit and installed at its final position. In the course of commissioning in 2007-2009, 700 million cosmics, krypton, and laser calibration events were collected with a preliminary calibration. The momentum resolution at $p_t = 10$ GeV/c is below 7%, close to the value quoted in the Technical Design Report [Tdr01]. The dE/dx resolution reaches 5% for long cosmic rays tracks, slightly better than the design value [Alme10].

To reach the TPC expected resolution values all the parameters must be under control in real-time. Of particular importance is the drift velocity of the chosen gas mixture that depends on pressure and temperature. The required resolution for the drift velocity is 10^{-4}. To monitor the drift velocity, a drift velocity monitor was installed and connected to the TPC gas system.

2.3 The drift velocity monitor of the ALICE TPC

The drift velocity monitor of the ALICE TPC, Gas prOportional cOunter For drIfting Electrons (GOOFIE), was designed at GSI. The same kind of drift velocity monitors has been employed successfully before to measure the drift velocity in other experiments as in the NA49 [Afan99], HADES [Lipp00], STAR FTPC [Morg01], and CERES [Mari04] reaching a resolution in the measurement of the drift velocity between 0.5 % and 0.05 %. We are using an improved version developed at MPI Munich. In addition to the drift velocity, the gas gain under working conditions can be measured via an integration of the signal. The device was also tested as a monitor for the composition of the ALICE TPC ternary mixture (Ne-CO_2-N_2 (90/10/5)).

2.3.1 Description

The drift velocity depends on the applied electric field (E) and on gas density (therefore on pressure P and temperature T). In GOOFIE (see Fig. 2.3), we try to reproduce the TPC physical conditions, by drifting electrons in our gas mixture, while we monitor these parameters (E, P and T).

GOOFIE was connected to the analysis line of the TPC gas system [Gar06] and it was operated under the same working field of E = 400 V/cm. The nominal voltage necessary for this working field, around -10 KV, was provided by an external Heizinger power supply PNC 20000-3 neg. To avoid fluctuations, L_d (drift length) is fixed, defined as the distance between two emitting radiation sources [Anto07] and T_d (drift time) is measured. Therefore, the drift velocity is:

$$v_d = \frac{L_d}{T_d} \ . \tag{2.1}$$

The field cage is defined by 30 parallel stainless steel plates of 0.5 mm thickness, separated 8.0 mm one from another [Anto07], with an installation precision of 20 μm. The drift channel, where we fix the drift length, is defined by 28 field plates (ring electrodes) with a 10 mm diameter hole in the middle.

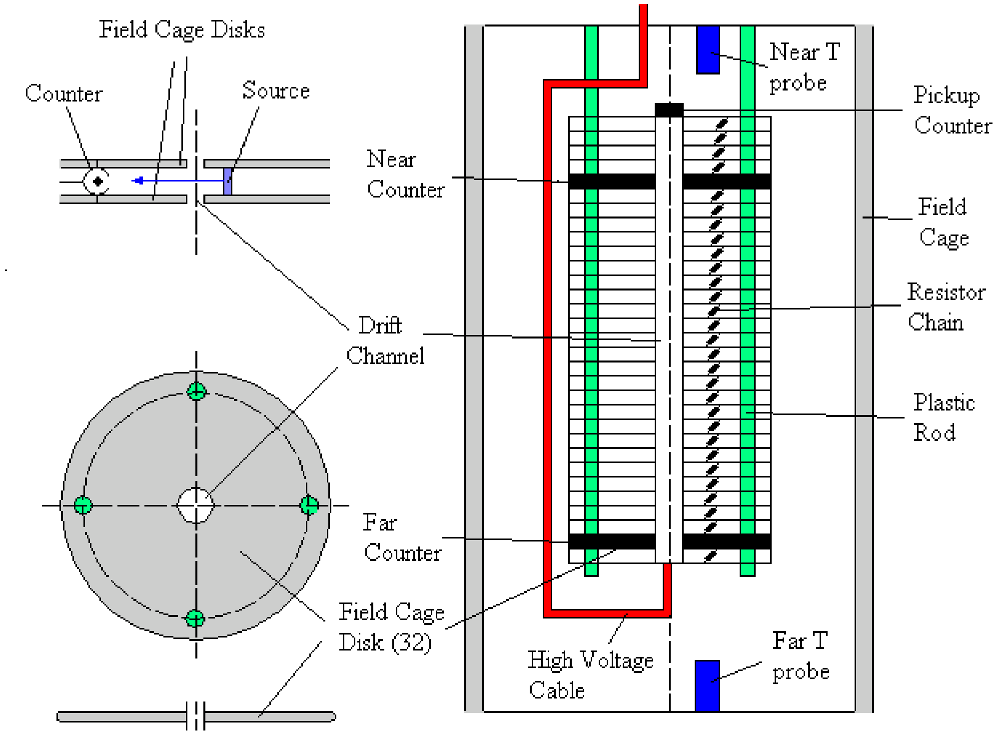

Figure 2.3: Layout of the GOOFIE, the drift velocity monitor for the ALICE Time Projection Chamber. Left, up: a part of two plates showing the relative position of the counter, its geometry, the source and the drift channel. Left, down: field cage disk with the drift hole (center) and the supporting holes. Right: View of the inner part of the field cage, showing how the field cage disks define the drift channel, marking the section where the near and the far counters (and sources) are located, and the position of the temperature probes.

The field plates are separated by a distance of 31.5 mm from a stainless steel tube (known as the field cage) which acts as an insulator from the exterior and as a vessel for the flowing gas. Like in the TPC it is necessary to degrade the applied high voltage using a resistor chain to obtain a uniform field. The GOOFIE resistor chain is composed of 29 resistors, one per space between field cage disk, of 2.750 ± 0.003 MΩ connected creating a resistor chain of 78.3 MΩ. The electron drift lines along the drift channel and the necessary field uniformity (up to reaching an error on the field of 2.3 per mil [Morg01]) are calculated with the GARFIELD software [Wie04, Gar80, Gar98].

Two α sources (Am_{95}^{241} , of energy E = 5.486 MeV) emit perpendicularly to the drift channel, ionizing our gas mixture on their way to two cylindrical "start" wire counters (called near and far counters) placed in front. The electrons produced in an ionization event drift to a counter at the end of the drift channel called pickup counter (see Fig. 2.3), where a pulse height spectrum is recorded as a function of time [Wie04]. The distance between the α-source and its trigger is set at the Bragg Peak for our gas mixture (Ne-CO_2-N_2 (90/10/5)) and our α-source (with E = 5.486 MeV) [Lipp00, Morg01] in about 40 mm. Measurements have been taken and these data compared with the output of the SRIM program [Srim01, Srim02] to fix this distance. By using two α sources we avoid the non-uniformities of the electric field near the pickup counter. The drift time T_d is defined by the difference between peak positions of different ionization events (near/far), and the distance between $rm\alpha$-sources (the drift length) has been fixed to L_d = 20.4 cm. Once T_d is measured, the drift velocity is then calculated according to Eq. 2.1.

The GOOFIE electronics was composed of two cards connected to a Linux PC. The GOOFIE board was built to work with the ALTRO chip, the same that the ALICE TPC is using in its readout electronics [Bram05, Anto07] and it is responsible for processing the analog signal of the ionization events. The board has 3 signal inputs, two for the triggering channels (near and far counters) and one for the pickup. It is powered by a DC power supply that is providing +5 volts for the analog and digital circuits, and it is connected via USB with the PC. A modified version of the original USB drivers for the ALICE TPC RCUs is used for communication with the card.

A second commercial PCI board NI-6220 was internally installed, and connected via a Very High Density Connector Interface (VHDCI) with a

SCB-68 68-Pin Shielded Connector Block, responsible for interfacing with the PT-100 sensors inside the container vessel and the pressure sensor connected to the gas analysis line providing gas to GOOFIE. A wrapper around the basic Linux drivers provided by NI was created to first monitor these values, two temperatures and one pressure, to later include the wrap in the on-line application that was used to operate the GOOFIE.

2.3.2 Operation

The power supply for the electric field is switched on manually. Once the nominal voltage for the uniform working field is reached, it is usual to monitor its stability for a period of around 30 minutes, before switching on the electronics. Since we are working close to the discharge regime for our gas mixture, this is a good practice to avoid accidental burning by a transmitted discharge of some of the GOOFIE board channels.

The previous on-line application [Anto07], prepared to read from the GOOFIE board, was modified to read also pressures and temperatures. When a trigger from one of the "start" wire counters is released, a signal is sent to the GOOFIE board. We call a GOOFIE event the group of the 3 signals (near/far counters and pickup) plus the last set of measured pressure and near and far temperatures (Fig. 2.4).

The drift velocity and the gain are obtained from the information resulting of adding 2500 GOOFIE events, to minimize fluctuations. The resulting spectrum is called the integrated signal, and can be seen in Fig. 2.5. The integrated signal was collected by the modified on-line application. Two threads were working on it: the acquisition thread and the analysis thread. In the acquisition thread, a GOOFIE event is acquired (each second, approximately) and stored as a group of static arrays in memory until the nominal value of 2500 events is reached, approximately half an hour each. Then, the integrated signal, also a static array, is copied to the analysis thread, where the next operations were performed; first the signals are recorded to a ROOT file, second, the resulting integrated signal (upper left panel of Fig. 2.5) is analyzed using an on-line version of the 'gas analysis' offline code, that will be described in the next paragraph, and third, the results were send to the ALICE TPC Offline Condition Data Base (OCDB) [Babl08], the memory is

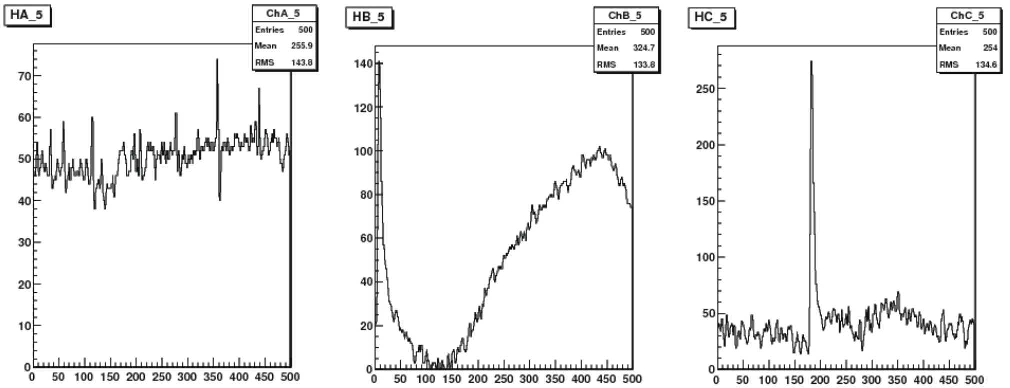

Figure 2.4: The three signals of one GOOFIE event, taken in October 29th 2006 during a test run at CERN. The x axis is divided in time bins, each one of a size of 50 μs. From left to right: signal of the near trigger counter, far trigger counter, and pickup detector. The three are stored, but only the pickup signal is used for calculating the drift velocity and the gain. The near signal shows only noise. Since the trigger threshold was set to 120 counts the peak in the far counter (140 counts) is our trigger signal. Therefore, the right panel is displaying what we call a far event. The image corresponds to the offline monitoring tool.

cleared and a 'waiting' signal is released to the acquisition thread, indicating that the analysis thread is ready to receive the next integrated signal.

The on-line version of the gas analysis offline code is designed as a library that is possible to 'plug' or 'unplug' easily from the main application. Three average temperatures are calculated: one corresponding to the near peak, one to the far, and one as the average of them. An average pressure for the acquisition interval is taken. The drift velocity and the gain corresponding to the near and far peak are obtained from the integrated signal spectrum. The corrected values for the drift velocity and near and far gains are calculated using the average temperatures and the average pressure. In addition, the gas composition after the corrected values is provided.

The procedure to deliver the above mentioned information is fully customizable. Once the application is started, several configuration files (the information contained on them will be explained later) are read. From these

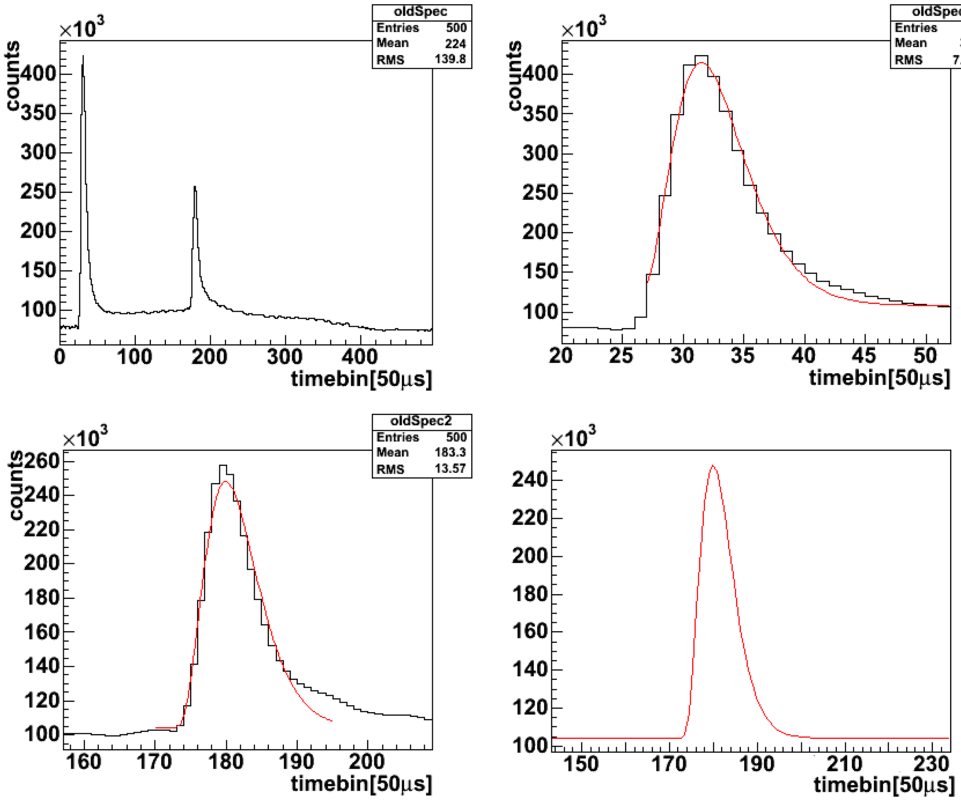

Figure 2.5: Gamma-4 fit of an integrated signal of 2500 GOOFIE events. Upper panel, left: Integrated signal of 2500 GOOFIE events. The x axis is divided in time bins, each one of 50 μs. The peak closer to the y axis is called the near peak, the second peak is called the far peak. Upper panel, right: zoom on the near peak, showing how it is fitted with a gamma-4 function. Lower panel, left: zoom on the far peak, with its gamma-4 fit. Lower panel, right: the gamma-4 function.

files the acquisition mode (static array size and integrated signal size), the analyzing method (fitting function and method to choose a window), the storage method (values from the array or from the fit of the peak), the drift distance (20.4 cm), the average values for the correction of the acquired data, and the plane coefficients for the composition calculation are derived. The configuration file also includes the size of the time bin (50 μs), the time interval between two sampled signals, despite of the fact that this number is given by the hardware specifications (the ALTRO chip).

When the integrated signal is available, a data object `CGPackData` is declared for storage. First the global temperatures and the global pressure are obtained. Then the array corresponding to the integrated signal of the C channel (the pickup channel for our settings) is scanned, and its first maximum localized and stored. The chosen window is established around it, and the region is fit. The next numbers are taken: area of the window, baseline, area below the fitting curve and peak after the fit function. Afterward, the measured window is removed from the array and the next maximum is searched. A similar operation is performed around this second maximum: storing of the maximum, fixing of a window, fitting in this window, area of the window, and area below the fitting curve. For the presented results, the information from the fit was chosen to be stored. So per integrated signal we obtain the near peak position and near area normalized by the number of near events (near gain) and the far peak position and far area normalized by the number of far events (far gain). Our drift time is given by the difference between the time bins corresponding to near and far peak position, multiplied by the time bin size (50 μs). Since the drift length is fixed, the drift velocity is then calculated using Eq. 2.1.

We call the result of the fit the 'raw' values. The raw drift velocity and the raw gains are corrected, based on the known dependence of the temperature and pressure of the gas mixture [Anto07], using the formula:

$$A_{d,corr} = A_{d,raw} - P(\frac{T}{P} - \langle\frac{T}{P}\rangle) \ , \tag{2.2}$$

where $A_{d,raw}$ is the measured raw value (drift velocity, near gain, and far gain), T/P is the gas density linked with the measured raw value, and $\langle\frac{T}{P}\rangle$

indicates an average value taken from one of the configuration files. The pressure is the global pressure for all the raw values, while we take as temperature the global values linked with the near temperature sensor (for the near gain correction), the far temperature sensor (for the far gain correction), and with the average of both (for the drift velocity correction). The result of the correction we see in Fig. 2.6.

Using the GARFIELD [Gar80, Gar98] and MAXWELL [Biag99, Anto07] programs it is possible to plot the variation of the drift velocity with CO_2 and N_2 concentration. They are appearing to lay approximately in a plane (Fig. 2.7). After fitting these planes, it is possible to write the next set of linear equations:

$$V_d(CO_2, N_2) = A * (CO_2) + B * (N_2) + C, \tag{2.3}$$

$$G(CO_2, N_2) = D * (CO_2) + E * (N_2) + F, \tag{2.4}$$

where A,B,C,D,E and F are the coefficients defining both fitting planes (plane coefficients), CO_2 and N_2 the gas contents (in percentage), V_d a drift velocity and G a gain. The gas composition is calculated from solving the system given by Eq. 2.3 and 2.4 after each couple (V_d, G) reading the plane coefficients from the configuration file. One example of the composition trends obtained is shown in Fig. 2.8.

The data sent per integrated signal to the ALICE TPC Offline Condition Data Base (OCDB) is a collection of values: drift velocity and drift velocity corrected, near gain and near gain corrected, far gain and far gain corrected, near temperature, far temperature, average of near and far temperature, CO_2 content (%), N_2 content (%) and a time tag. This is done using a special data class implementing a DIM server, a protocol developed at CERN used in all LHC experiments. The DIM server delivers the information to a Windows PVSS client, a commercial software also used for controlling LHC experiments. In addition, the recorded data was stored locally.

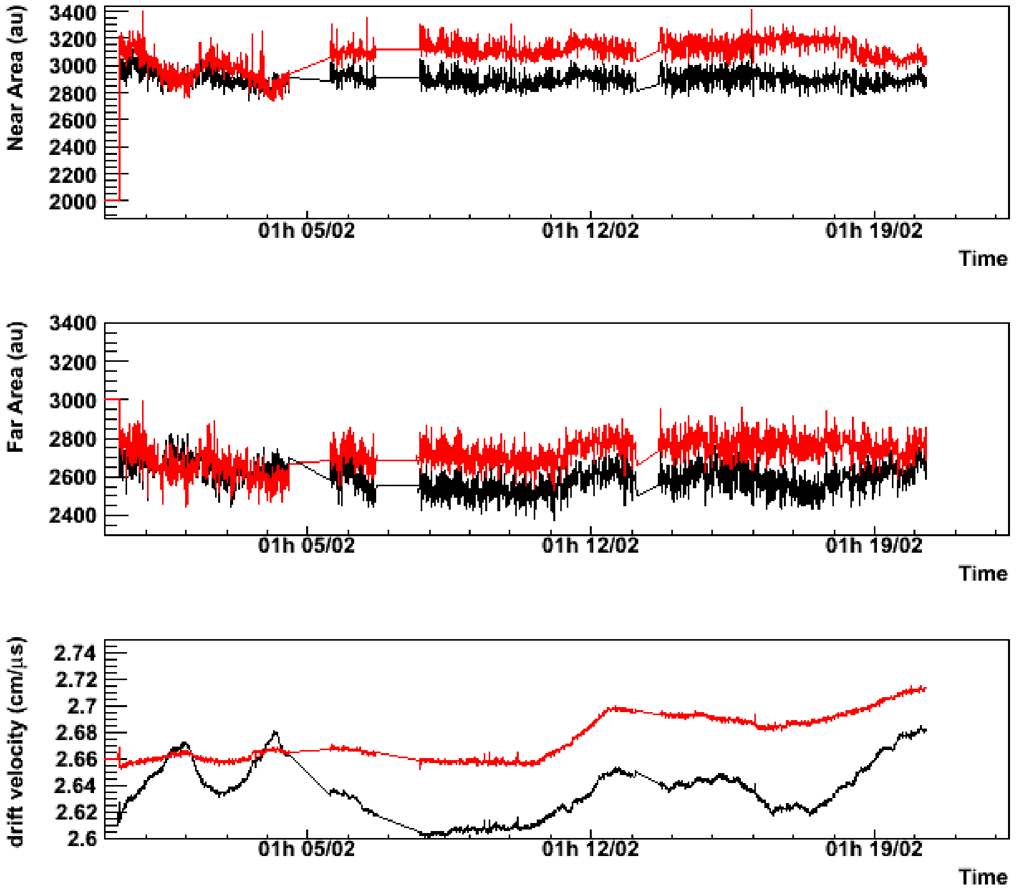

Figure 2.6: GOOFIE drift velocity and gain measurements from the test run in January 2008. It shows the drift velocity and near and far gain measured (black) and corrected (red). The reference values used for the correction taken from the configuration file were $< T_N >= 297.18$ K, $< T_F >= 295.48$ K, $< T >= 296.33$ K and a$< P >= 0.97695$ bars. The straight lines correspond to rejected data points or periods of time when the on-line application was not running.

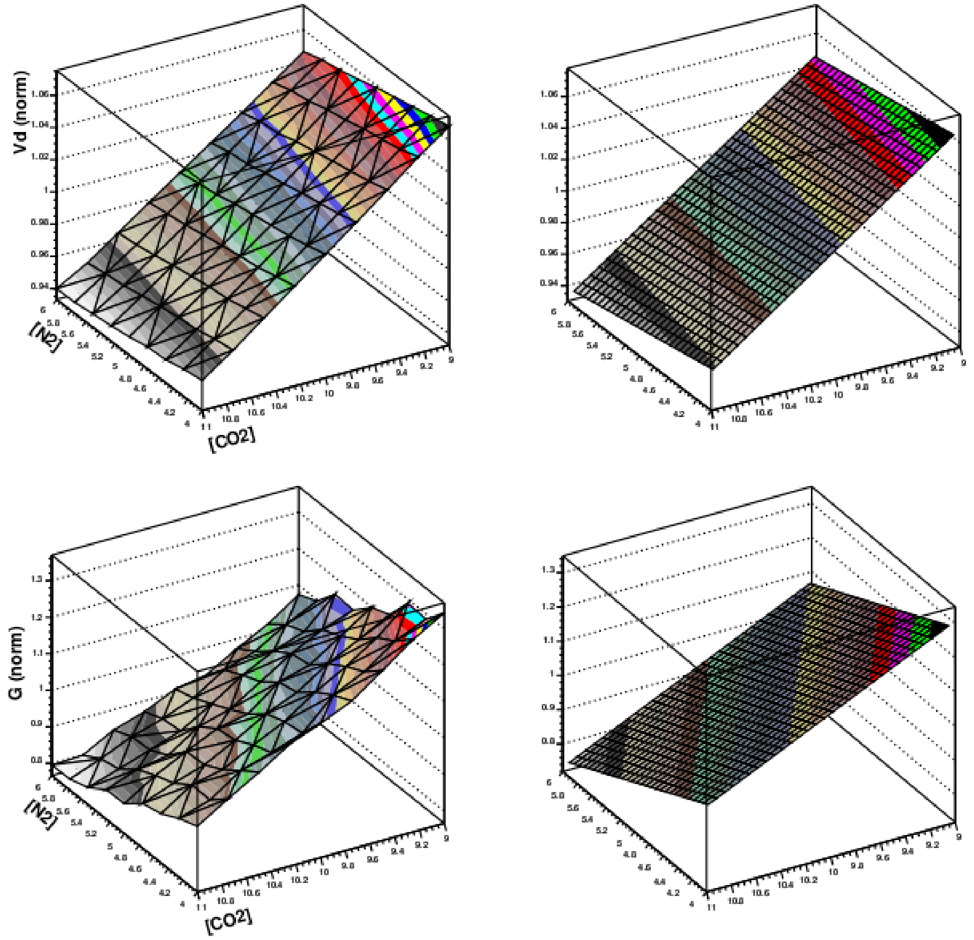

Figure 2.7: Drift velocity and gain dependence of CO_2 and N_2 concentration, and its corresponding fits to planes. Left panels: Data from GARFIELD [Gar80, Gar98] and MAXWELL [Biag99, Anto07]. The drift velocity and the gain have been normalized using the central point of each plane (drift velocity corresponding to a composition of CO_2 =10% and N_2=5%, gain corresponding to a composition of CO_2 =10% and N_2=5%) Right panels: Fit of the data to planes. The coefficients of the fit to planes are used for the composition calculation.

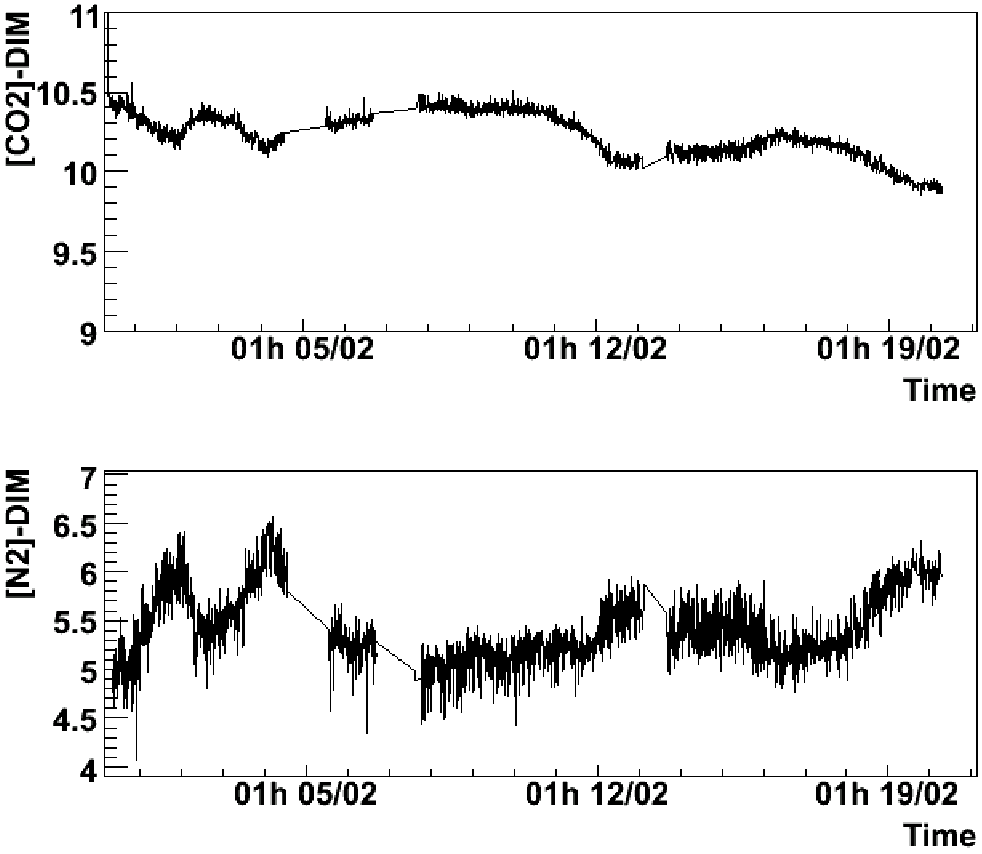

Figure 2.8: GOOFIE composition measurements from the January 2008 test run. The Y-axis is indicating the CO_2(labeled [CO2]-DIM) and N_2(labeled [N2]-DIM) on-line calculated gas percentages. Displayed points are glitch-filtered (outliers eliminated). A buffer is created and the last point stored on it. If the incoming point is outside the fixed range, the buffer is displayed instead. One tick on the horizontal axis corresponds to one day.

2.3.3 Status

GOOFIE was working in an intermittent mode due to several technical problems that we will briefly describe below. During its working time drift velocities and gain values were acquired and the gas composition derived from them. Drift velocities were in agreement with the result from laser measurements (Fig. 2.9).

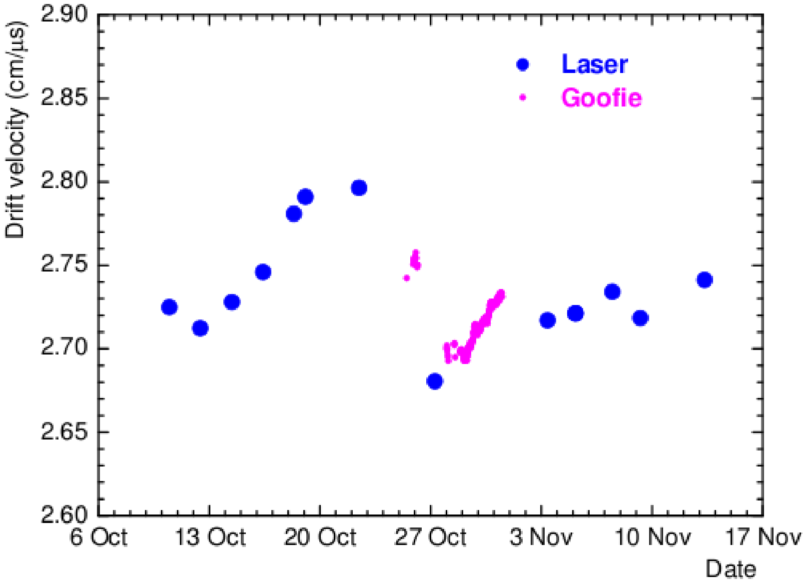

Figure 2.9: Comparison of drift velocity values obtained with laser measurements and the GOOFIE offline values.

Gain values from GOOFIE need to be normalized to be compared with reliable TPC gain results. At the moment of this analysis, no comparison has been done.

The composition calculation can be cross-checked with the value from a gas chromatograph connected to the gas analysis line of the TPC gas system. An unidentified correlation between the calculated CO_2 content and N_2 content has been observed. The discrepancy could be linked with the simplification of the running code that left only one T/P correction mode or the change of the working conditions (to a new pressure and temperature ranges). For the composition calculation the T/P register values were used instead of a set of recent data points, like before. The data for drawing the composition planes (Fig. 2.7) was also simulated for other working conditions (different gain and pressure). This could be solved by including an auto-calibration mode: T/P average values could be then re-calculated after a day of data taking, each week. A new and more detailed simulation of the gain and drift velocity dependence of the gas composition could be also necessary.

Concerning the technical problems, before an automatic procedure was developed to deliver meaningful information and to move the backup raw data, the running time was limited to disk space. Twice one of the acquisition channels of the ALTRO board was burnt due to sparks propagated by the cable connecting the detectors and the board or a slight modification of the working conditions -like an unexpected power cut-, and there was no spare board to replace the burned one, since it was a prototype. Once the ALTRO chip itself was burnt, due to an undetected damage in the cooling mechanism of the card. Since the ALTRO drivers of the GOOFIE board were not designed for the used Linux distribution but for one slightly older, it was found out that it was necessary to reboot the board and/or the computer frequently, therefore, requiring permanent monitoring. Added to that, the PVSS-DIM application responsible of delivering data to the OCDB was not fully available during the testing period, therefore, to perform a correction on the working mode it was necessary to off-line analyze the acquired data. A shielding to avoid the damage on the GOOFIE board by sparks is under development.

Chapter 3

ALICE data analysis strategy

Samples of $10^5 - 10^7$ simulated proton-proton collision events under different physical premises were generated in several campaigns coordinated by the ALICE offline group. The events were used to test the complete analysis chain, and in particular, the technical aspects of the grid-based distributed reconstruction which are not trivial and require regular exercise and optimization.

In this chapter, we describe the official analysis strategy to establish a common ground for a more specific multiplicity analysis, characterized in the next chapter.

3.1 Simulation

A good and precise simulation is the key for an optimized detector. A heavy ion collision at LHC energies results in a very large number of particles in the final state, a formidable challenge for the reconstruction and analysis algorithms. The exact multiplicity which is to be expected is not easy to predict, despite of the available data coming out of previous experiments. The c.m. energy at the LHC exceeds those at the SPS and RHIC by the factors of 300 and 30, respectively. In the case of pp collisions, on the other hand, the step is not that large, as the Fermilab worked with $p\bar{p}$ at 1.96 GeV.

AliRoot is the ALICE data processing software package. It includes detector description, event generation, particle transport, reconstruction, particle identification and generation of summary data. It is based on ROOT [Brun97] and it uses external packages like Geant [Brun87] and FLUKA to perform the transport of particles through the detector and simulate energy deposition, necessary to estimate detector response. The software is written in C++ following the Object Oriented Programming (OOP) paradigm. Wrappers are provided for legacy code and existing libraries like PYTHIA and HIJING.

The generators are based on known information, like on parametrized pseudorapidity density and transverse momentum distributions of charged and neutral pions and kaons. A typical hadronic event generator simulates initial-state composition and substructure, initial-state showers, hard and semi-hard processes, resonance decay and final-state showers. The set of AliRoot generators is provided by the ALICE offline group in charge of the event generation with a collection of possible scenarios for different physics in a modular way, which may result in different multiplicities or p_t or rapidity distributions. The user can even define its own 'generation cocktail' with weighted contribution from each generator. AliRoot was written avoiding the dependencies on a specific model, and requiring flexibility. The generators available in AliRoot are [Carm07]:

- PYTHIA [Sjos01]. Based on the 'Lund string fragmentation' model. It allows the user to switch on and off individual physics processes. There are several PYTHIA versions available, in FORTRAN and C++. PYTHIA is used for proton-proton interactions and for jet generation.

- HIJING (Heavy Ion Jet Interaction Generator) [Gyu93]. Based on a QCD model, it treats jet fragmentation using the 'Lund' model. The HIJING model has been developed to study the role of mini jets in pp, pA and AA reactions.

- HERWIG (Hadron Emission Reactions With Interfering Gluons) [Corc01]. Based on 'cluster hadronization', it uses the parton-shower approach for initial and final-state QCD radiation, including color coherence effects and azimuthal correlations both within and between jets. The last C++ version can include supersymmetric processes and allows to change the properties of the produced particles (mass, lifetime, etc).

- DMPJET. An implementation of the two-component Dual Parton Model (DPM) for high-energy hadron-hadron, hadron-nucleus, nucleus-nucleus and photon-nucleus collisions [Ppr104]. It is based on the Gribov-Glauber model of high-energy hadron-nucleus and nucleus-nucleus collisions. Multiple-parton interactions for individual hadrons are described by the PHOJET generator.
- PHOJET [Eng97]. A photon flux simulation for photon-hadron and photon-photon processes in lepton-lepton, lepton-hadron, and heavy ion-heavy ion collisions. Formulated as a two-component model (soft and hard component), it implements Regge phenomenology and Gribov's Reggeon calculus, allowing multiple soft and hard interactions to be generated in one event. Written in FORTRAN.
- ISAJET [Baer05]. Based on perturbative QCD plus phenomenological models for parton and beam jet fragmentation, its main feature is that it goes beyond the Standard Model, including for example supersymmetric theories. Written in FORTRAN.

The AliRoot event generators produce a set of particles with their momenta. The information about the particles, including the mother-daughter relationship and production vertex is stored in a kinematic tree. The kinematic tree is passed to the transport code. All generators are implemented via the ROOT generic class `TGenerator`, and in AliRoot their parameters are accessible through wrapper classes and functions. A parametrized generation, where a collection of distributions (dN/dy, p_t, etc.) is used as an input, can be performed by the specific AliRoot class `AliGenParam`. For specific studies, like HBT or azimuthal anisotropies, special generators are also provided.

3.2 Reconstruction

The reconstruction is expected to be performed with high efficiency, purity and resolution. The user should be able to obtain the data needed for a physical analysis from an easy-to-use interface from this. It is aimed to be flexible, accepting configurations where one of the detectors is not present, for example. Its code needs to be maintainable and well documented.

The main concepts used in the reconstruction are [Carm07]:

- Digit: detector signal represented by one ADC count on one single readout channel. In case of drift detectors, one digit is an ADC value of a pad in a time bin.
- Cluster: group of digits presumably created by the same particle close in space and in time.
- Reconstructed space point: estimate of the real position of the particle that created the cluster. It is frequently identified with the center of gravity of the cluster.
- Reconstructed track: set of five parameters (two positions, two angles and the curvature) corresponding to a particle's trajectory, and the associated covariance matrix.

The general reconstruction framework is shown in Fig. 3.1. The local reconstruction is the first step of the reconstruction process. By local we mean in each detector separately and without exchanging information with other detectors. The clusters are created in this step. A local reconstruction for a detector is performed by a reconstruction module only if the general reconstructor is configured for it, allowing the user the disconnection from the reconstruction of a detector or a group of them. The resulting clusters are stored in a ROOT file, creating trees handled by the loaders.

The vertexing is the reconstruction of the primary vertex position. It is executed once the local reconstruction has been done for all the detectors, using the information provided by the silicon pixel detectors, which constitute the two innermost layers of the ITS. The vertex position can be inferred in a first estimation from the distribution of the z-coordinates of the reconstructed

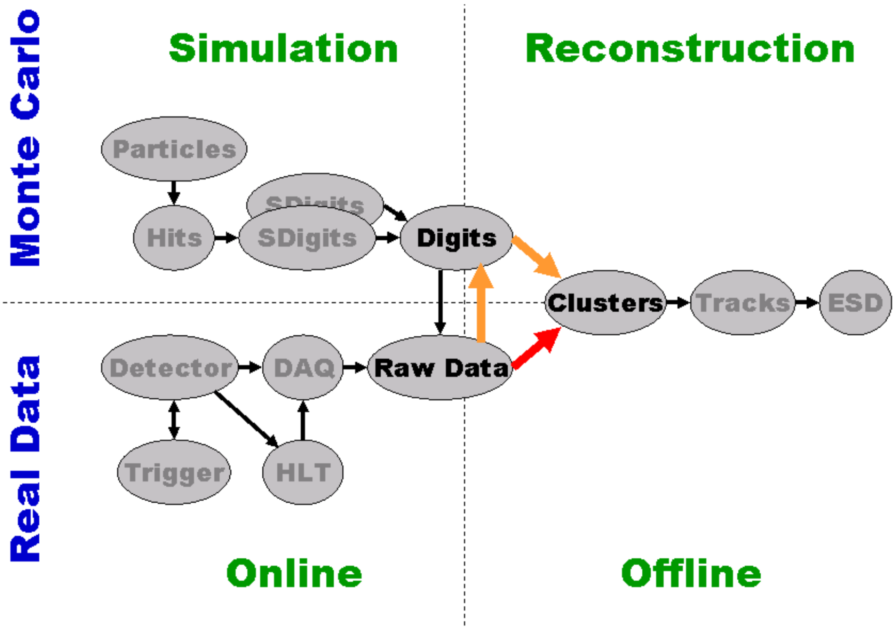

Figure 3.1: ALICE reconstruction scheme. The Monte Carlo data out of the simulation is playing in the ALICE reconstruction scheme the role of real data, serving as an input of the offline reconstruction framework.

space points in the first pixel layers, since the centroid of the distribution is correlated with the true vertex position. The final vertex position is fixed after the correlation between the points z_1, z_2 given by the two innermost ITS layers.

The track reconstruction can be divided into two large groups: global methods and local methods. The global methods are more stable with respect to noise and bad measurements, and they can operate directly on the raw data, but they require a precise global track model. Such a track model can be unknown or does not even exist because of stochastic processes (energy losses, multiple scattering), non-uniformity of the magnetic field, etc. Local methods, on the other hand, do not require the knowledge of the global track model. The track parameters are always estimated at a given point in space. They are sensitive to noise, wrong or displaced measurements and the precision of space point error parametrization, but local track peculiarities (stochastic physics processes, magnetic fields, detector geometry) can easily be understood. In the barrel part, track reconstruction is done in three passes. First, a track finding and fitting is executed in inward direction in the TPC and then in the ITS. Second, a track reconstruction in outward direction is performed through all detectors starting with the ITS. The last is a track refit in inward direction from TRD to TPC and then to ITS to get the track parameters at the vertex. The exchange of track information between detectors without introducing code dependencies is done using the combined track reconstruction.

The reconstruction of cascades, kinks, and V0s is performed with the tracks that fulfill the final refit towards the primary vertex. They are treated separately. We call cascades to the family of particles resulting from the decay of hyperons (Ξ). Decays of charged particles containing one or more neutral daughters appear as a discontinuity of the mother track at the point of its decay (kinks). The kaon decays into muon+neutrino, $\pi^{\pm} + \pi^0$, muon+ π^0 + neutrino, $\pi^{\pm} + \pi^0 + \pi^0$, are candidate for kinks. Decays of neutral particles in charged particles can be reconstructed with the daughter tracks pointing to a common secondary vertex (V^0).

The input to a reconstruction can come from raw data (real data registered by one of the detectors) or from digits in ROOT tree format. The latter is used in the case of simulated events. In AliRoot, there is class responsible for dealing with the input, called `AliReconstruction`.

The reconstructed tracks are stored on an Event Summary Data (ESD) file. Each ESD event contains global event properties and a list of reconstructed tracks/particles, kinks, V^0's, cascades, and particle identification information (PID) following the Bayesian approach. The information about the detector used to reconstruct a track is encoded as a bit pattern associated to it. A standalone library (`libESD.so`) contains all the classes that are needed to process and analyze an ESD. A typical ESD file with 100 proton-proton events has a size of around 8 Mb which is one order of magnitude smaller than raw data.

Optionally, ESDs can be further reduced by a factor of 13 for proton-proton collisions (5 for Pb-Pb collisions) by leaving out the supplementary information still present on ESD (orphan tracks, vertexes, etc). The reduced events are called Analysis Oriented Data (AOD). Specific AODs, containing subsets of ESD events selected after a certain criteria, are foreseen as well. Some of the AOD sets may be so small that they would fit on a single storage element or even on one computer

For simulated events, the ESD or AOD information is complemented by the Monte Carlo Truth (sometimes called MC Truth, MCT or simply MC) events containing the particles as created in the event, and traversing the containing detectors. They are managed by an AliRoot class derived from the ROOT Virtual Monte Carlo class, *TVirtualMC* [Carm07], that is also providing an interface with the detectors geometry. MC Truth data is used as an reference to study the efficiency and the resolution of the experiment.

3.3 Analysis

The Event Summary Data (ESD) is obtained from a simulation or real data using the reconstruction framework, and it contains the basic information for our analysis. The implementation of physics analysis, running on ESD or AOD data and possibly using MC Truth, is described below.

3.3.1 Analysis framework

The analysis framework (Fig. 3.2)[Carm07] is designed to process ALICE data in an efficient way.

The communication between analysis modules is done via container objects. Access to ALICE-specific simulation/reconstruction or analysis data is provided via ESD, AOD and MC event handlers. There must be at least one input slot, common for all analysis modules and handled by a manager class. The input slot is the ESD or AOD chain. At least one output slot must be defined per user analysis module. An analysis manager class is coordinating a list of client analysis modules (tasks) that share the same event loop.

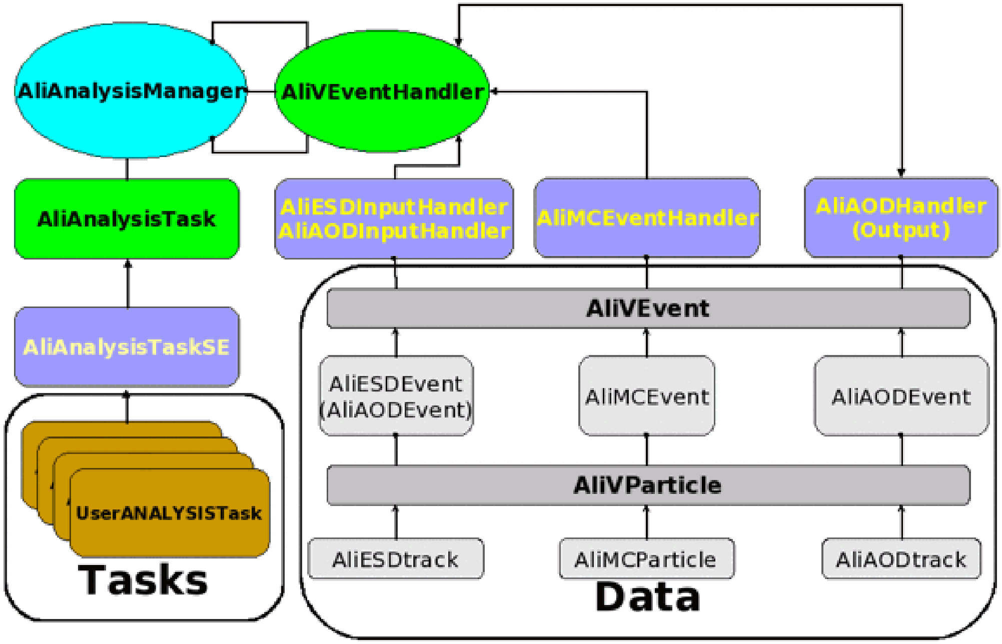

Figure 3.2: ALICE analysis framework. The user delivers his/her analysis in the form of an analysis task (`AnalysisTask`) deriving from the general `AliAnalysisTask`. The Analysis Manager `AliAnalysisManager` connects the task with the data via handlers. Three types of data are made available to the user: Event Summary Data (ESD), Monte Carlo (MC), and Analysis Oriented Data (AOD).

3.3.2 The analysis manager

The AliRoot analysis manager class (`AliAnalysisManager`) is coordinating the analysis session. The `AliAnalysisManager` is handling a list of analysis modules (called `AnalysisTask`, or simply tasks) with a common event loop, thus reducing multiple access to stored data. A task is basically a C++ class that inherit from the AliRoot class `AliAnalysisTask` [Carm07]. The user must implements the following set of virtual methods:

1. `DefineInput` and `DefineOutput`. They must be called when the task is created (in construction time), and they are responsible for allocating the slots for data containers. An ESD or AOD chains can be our input data containers. They must be linked with an slot, and they can be

common for all the tasks. The user defines the output slot for his analysis. It has to be a ROOT object like a TList or TObjectArray, stored in a ROOT file, or an AOD chain (than can be used as an input for a different task).

2. `ConnectInputData`. The user event handler (ESD, MC, AOD) is connected via this member function. It is called once at the beginning of the run. More than one event handler can be connected in one run, e.g. it is possible to access ESD and MC information in the same task.
3. `CreateOutputObjects`. Objects like ROOT histograms should be defined (bins, axis ranges, etc.) here.
4. `Exec`. The analysis is performed here. The event information is made accessible from the event handlers. Once the event is analyzed, the data is 'posted' to the output container. For a histogram, it is 'updated' with the event information.
5. `Terminate`. Called once at the end of the analysis. Memory is freed and the user files are closed.

A single event analysis task class `AliAnalysisTaskSE` optimized for single event analysis, and a multiple event task class `AliAnalysisTaskME` for multiple event analysis (like for event mixing) derived from the general `AliAnalysisTask` exist also for performing specific analysis in an optimized way [Carm07].

The task can run in several different environments without being modified. Available options include a local analysis via ROOT, distributed analysis using the Parallel ROOT Facility (PROOF), and analysis on the LHC Computing Grid, a network designed by CERN to handle the massive amounts of data that are expected to be generated by LHC experiments [Carm07]. The task can run alone or linked with other tasks, forming an analysis train.

3.3.3 Analysis train

The analysis train is the recommended way to run several analysis tasks over a large data set (see Fig. 3.3). Since the analysis train makes use of the `AliAnalysisManager` framework, the access of data can be performed via a common interface and the CPU/IO ratio is optimized. An analysis train can be started on PROOF and GRID infrastructures [Carm07] or run in a computing batch farm.

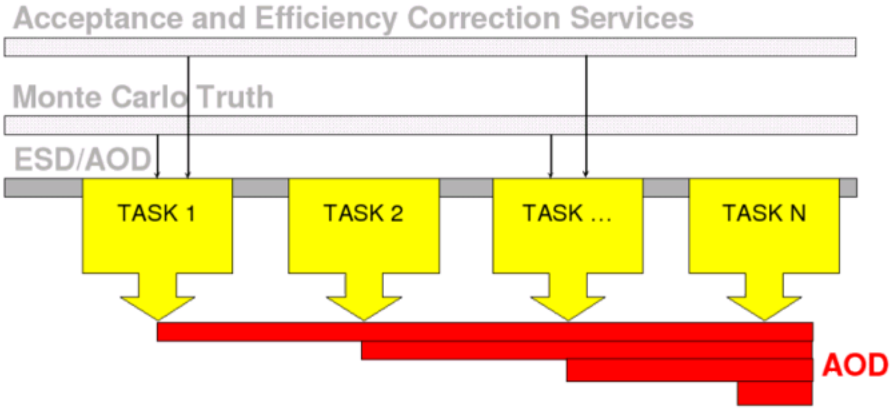

Figure 3.3: Data analysis train. Input data of various types are provided to user tasks by the analysis manager. The tasks may produce reduced events (AODs) which may be used by subsequent tasks in the same train.

A task can generate AOD files. The event selection is done by asking for event tags in an event database. The rejection speeds up considerably the analysis, however, it is possible to run over the whole data sample, without a special event cut.

The task may require specific software, e.g. definition of the classes it uses. This software has to be provided in form of a PROOF archive ('par file'). A par file is a standard tar file containing the source code needed by the task and the subdirectory PROOF-INF with macros for configuring and compiling.

The user is responsible for the validation of the task code. This is normally done by copying locally a limited number of ESD files and trying to run a local analysis. Once the user is satisfied with the output of the local test, he or she passes his task and the associated par file (if any) to the person in charge of the train.

Chapter 4

The multiplicity analysis task

The multiplicity analysis presented in this thesis was implemented as a user task and was run on a train as described in the previous chapter. Below, we present the basic concepts for the analysis, the analysis itself, the implementation used, and the applied cuts.

4.1 Basic concepts

The ALICE coordinate system is defined following the LHC rules. It is a right-handed orthogonal Cartesian system with the origin at the LHC interaction point IP2 [Int03]. The x axis is horizontal and points toward the center of the LHC. The y axis is in upward direction.

Using the ALICE general coordinate system, we define a forward pseudorapidity region ($\eta > 0$) and backward pseudorapidity region ($\eta < 0$). By dividing both spaces into small sections we specify forward pseudorapidity intervals and backward pseudorapidity intervals of fixed width (see Fig. 4.1).

For the multiplicity analysis task, this width is fixed to 0.2 units of rapidity. Since it is fixed, we identify the pseudorapidity section with only two labels: one sub-index for the pseudorapidity region (forward labeled with F, backward with B) and the position of its geometrical center. For example,

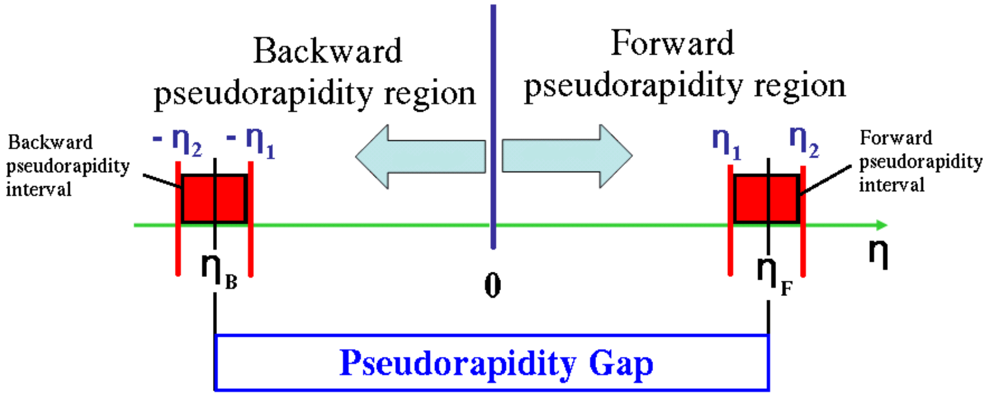

Figure 4.1: Schematic diagram of the pseudorapidity space division. Two regions are defined: the forward pseudorapidity region ($\eta > 0$) and the backward pseudorapidity region ($\eta < 0$). In one region, a pseudorapidity interval ($\eta_2 - \eta_1$) is defined as the pseudorapidity space between two given pseudorapidities. This pseudorapidity interval is labeled with the absolute value of the position of its center ($(\eta_2 - \eta_1)/2$) and a tag for identifying the region (F for Forward, B for Backward). A pseudorapidity gap ($\Delta\eta = \eta_F - \eta_B$) is defined between η_F forward pseudorapidity intervals and an η_B backward pseudorapidity intervals [Tarn08]. Rapidity can be identified with pseudorapidity for transverse momentum much higher than the particle mass.

a pseudorapidity section from $\eta_1 = 0.2$ to $\eta_2 = 0.4$ in the forward region is labeled $\eta_F = 0.3$. A pseudorapidity gap ($\Delta\eta$) is defined as the distance between the centers of the forward and backward rapidity intervals. For $\eta_F = \eta_B = 0.3$ the pseudorapidity gap is $\Delta\eta = 0.6$.

4.2 Basic idea of the analysis

We perform two different analyses. On one side, the multiplicity fluctuations are studied by analyzing the distribution of charged particle multiplicity within -0.9 $< \eta <$ 0.9 (TPC central acceptance). Multiplicity distributions of reconstructed tracks can be compared to the primary ones in order to evaluate the detector response. The shape of the distribution can fit by a negative binomial distribution, and the KNO scaling can be verified by plotting the properly scaled distribution along with those simulated for other energies.

On the other hand, forward-backward correlations are addressed by analyzing the multiplicity in two pseudorapidity regions separated by a gap (see Fig. 4.1). The correlation strength b is defined as the linear coefficient of the relation between forward and backward multiplicities:

$$\langle n_B \rangle (n_F) = a + b * n_F \rightarrow b = \frac{\langle n_B \rangle (n_F) - a}{n_F} \; , \tag{4.1}$$

as we already saw in Eq. 1.10 or as a function of a forward-forward dispersion D_{FF} and backward-forward dispersion D_{BF}:

$$b = \frac{D^2_{BF}}{D^2_{FF}} \; . \tag{4.2}$$

The dispersion coefficients are obtained from the multiplicity N_F in the forward pseudorapidity interval and the multiplicity N_B in the backward pseudorapidity interval:

$$D^2_{BF} = \langle N_F \; N_B \rangle - \langle N_F \rangle \langle N_B \rangle \; , \tag{4.3}$$
$$D^2_{FF} = \langle N^2_F \rangle - \langle N_F \rangle^2 \; . \tag{4.4}$$

The average forward and backward multiplicities can be referred to an interval or to the whole forward or backward pseudorapidity region. The correlation strength b as defined in Eq. 4.2 is supposed to be exact for a system divided in two hemispheres if we assume dispersions are having the same value for the forward and the backward coefficients. Since this is not always the case, we can consider also the backward-backward dispersion D_{BB}:

$$D_{BB}^2 = \langle N_B^2 \rangle - \langle N_B \rangle^2 \ . \tag{4.5}$$

Then, we can measure 3 different correlation strengths:

$$b_F = \frac{D_{BF}^2}{D_{FF}^2}, \quad b_B = \frac{D_{BF}^2}{D_{BB}^2}, \quad b_g = \frac{D_{BF}^2}{\sqrt{(D_{BB}^2 * D_{FF}^2)}} \ . \tag{4.6}$$

We will refer to b_F as the correlation strength (forward), b_B as the correlation strength (backwards), and b_g as the correlation strength (general case). In Section 5.4 we will compare these 3 values with the one given by the linear coefficient of the relation between forward and backward multiplicities.

4.3 Analysis implementation

In this section we describe the features of the multiplicity analysis task, the used cuts, and the analyzed samples.

4.3.1 Task details

The analysis was considered under two approaches. The first approach was to use the ROOT tree as an output container, with a set of numbers corresponding to relevant track/particle/event information. The second approach was to record the relevant histograms for a further analysis. The ROOT tree option was proven to be more versatile, since it is possible to use the same library created for the train also for external analysis, with small modifications. Histograms were recorded also, separately, to use them as a quick cross-check tool.

The ROOT tree implementation allowed the multiplicity task to cover a region, from $\eta_F = 0.1$ to $\eta_F = 0.9$ and from $\eta_B = 0.1$ to $\eta_B = 0.9$ in the case of an ESD (MC Truth) analysis (see 3.2), and an extended range for an independent PYTHIA analysis (see Sec 3.1) from $\eta_F = 0.1$ to η_F=1.9 and from $\eta_B = 0.1$ to $\eta_B = 1.9$. This results to an ESD (MC Truth) analysis from $\Delta\eta = 0.2$ to $\Delta\eta = 1.8$, and for a PYTHIA analysis to cover the region from $\Delta\eta = 0.2$ to $\Delta\eta$ =3.8.

The ROOT tree is analyzed by a library created for different reasons. One is the flexibility, since the library could be used by other data samples different from the one provided by the standard analysis (like PYTHIA samples), the other is the modularity. Several modules (C++ classes) were written, one for dealing with the information obtained from each pseudorapidity interval, one to define the control histograms, one to handle the fits of the correlation histograms, one providing fits for the MD, and one for each method studied for the calculation of the forward-backward correlation coefficients. The library can be compiled separately or as a par file.

No AOD file was produced. The task was usually tested after each modification locally in a small ESD sample, like suggested by the standard procedure. ESD and MC Truth data were analyzed using the standard analysis train. Reconstructed cosmic data were analyzed running the task in a stand-alone mode to test the code with a real output. PYTHIA samples were produced and 'translated' using additional code to match the input of the tree analyzing classes. See Sections 4.3.3 and 4.3.2 for more details on it.

4.3.2 Track cuts

When analyzing ESD data, the `AliESDtrackCuts` class was used to select good tracks. The following track quality cuts were applied:

- Minimum number of 50 TPC clusters in a track. The number is an indication of the length of the track. With this cut, fake tracks, partially reconstructed or bad reconstructed tracks are rejected.
- Maximum χ^2 per TPC cluster: 3.5. By cutting on this χ^2, we assure the clusters are properly identified. Cluster with bigger χ^2 can lead to misidentified tracks.
- Maximum covariance diagonal elements: $\sigma_y^2 = 2$ cm^2, $\sigma_z^2 = 2$ cm^2, $\sigma^2_{sin(\phi)} = 0.5$, $\sigma^2_{tan(\lambda)} = 0.5$, $\sigma^2_{1/p_T} = 2$ (GeV/c)$^{-2}$. The resolutions σ_y^2,

σ_z^2, $\sigma_{sin(\phi)}^2$, $\sigma_{tan(\lambda)}^2$ and σ_{1/p_T}^2 are the diagonal elements of the track parameter covariance matrix [Gros08]. The variables are defined with respect to a certain local reference plane X = X_{ref} rotated by an angle α around the global z direction [Dain03].

- TPC refit is required. After clusters are found, and a track is identified using Kalman filtering, an additional refit in the opposite direction (if inwards, backwards and viceversa) is required inside the TPC fiducial volume. If a track has not been fitted twice, it is rejected.
- A vertex fit cut is required and equal 3 σ. If the track is not linked with a vertex properly identified, it is not accepted. This cut filters out tracks which are not coming from a vertex.
- Rejection of kink daughters. With this cut, we expect to remove the products of the decays of a track with a special topology, which are not contributing to the relevant physics.

This collection of cuts is referred sometimes as the standard cuts.

The Monte Carlo (MC) Truth corresponding to each analyzed event was read separately, but in the same task. Therefore it was necessary to reproduce the standard ESDs track cuts for the TPC. To do so a collection of validity check functions was written, with the aim of having the possibility to plug/unplug or modify the cut for the Monte Carlo information easily. In this analysis, first the existence of a particle associated with the MC tag for the track is checked. After that, it is checked that the particle is really charged and physical primary [2], that the detector tag associated with the MC particle corresponds to the TPC (using detector track references), that the vertex position was inside a given range, and that the particle is consistent (rejecting particles that are decaying from themselves, for example). We applied a momentum cut of 0.2 GeV/c, since particles with lower momentum are not reaching the TPC [Ppr104] or are not detected, to avoid unidentified effects.

---

[2] We define physical primaries as all particles produced in the collision excluding feed-down from weak decays of strange particles.

For PYTHIA events, only a cut on the momentum (the same as for the MC Truth, $p_t > 0.2$ GeV/c) was applied. PYTHIA data samples are reaching up to 10 units of pseudorapidity in our forward-backward correlation analysis. However, this was a compromise limit and not an absolute one. In comparison, ESDs and MC Truth are covering only a portion of it due to the detector acceptance. PYTHIA data samples were processed with the help of the library created after the par file used with the multiplicity analysis task. The 'raw' PYTHIA file is given as an input of a macro that has as an output a tree with the same structure as the one provided by the multiplicity analysis task. Like this a direct comparison is possible between PYTHIA events and the output of the multiplicity analysis task, being the difference between our PYTHIA events and the output of the multiplicity analysis task that the first one is free of detector effects.

4.3.3 Input data samples

As a first approach to benchmark the analysis code, a PYTHIA tuning (see 3.1, [Sjos01]) for minimum-biased events was chosen. PYTHIA was proved to give a faster result (in term of computing performance) for testing purposes. The aim of this exercise was to test the PYTHIA generation code and the general multiplicity analysis code, and to understand the differences between different PYTHIA versions and tunings. Therefore detector effects and efficiency were not considered. Once the validity of the PYTHIA tuning was proved, a bigger sample of proton-proton collision (half a million) was generated using the same tunings as the one used for the MC Truth of the official production. To demonstrate the tuning was right, some reference distribution were obtained.

The multiplicity analysis task ran on the train over approximately 40 million of already available simulated proton-proton collisions, ESDs and MC Truth (see 3.3). The sample size of 90000 events for charged particle multiplicity distribution analysis and for forward-backward multiplicity correlations analysis was taken as a reference.

During the ALICE TPC cosmic run of June 2008, data from cosmic events was acquired. This data was later reconstructed. An analysis on the resulting files was performed also, to test the multiplicity analysis task on real data.

Chapter 5

Analysis results for simulated pp events

In this chapter, we present the output of running the multiplicity analysis task described in Chapter 4 over the samples summarized in Section 4.3.3. These results are compared to each other, with previous experimental results, and with theoretical predictions.

For PYTHIA 6.319 events, an arbitrary limit in the phase space of $|\eta| < 3$ was introduced. In the case of reconstructed data, this limit is given by the detector acceptance. For the ALICE TPC (see Section 2.2), the pseudorapidity coverage is $|\eta| < 0.9$ for tracks with full length and $|\eta| < 1.5$ for short tracks.

From each sample and applied cut, multiplicity distributions (MD) for ALICE TPC inside the acceptance ranges $|\eta| < 0.9$ and $|\eta| < 1.5$ were obtained by adding the contributions of each pseudorapidity interval. In the case of PYTHIA, additional MDs up to the maximum phase space considered $|\eta| < 3$ were also stored. The resulting histograms were scaled and fitted with a negative binomial (NB) and with the superposition of two NB.

Forward-backward (FB) correlation plots of forward charged particle multiplicity n_F versus the backward charged particle multiplicity n_B for all the input samples and the considered cuts were created. The phase space covered was also up to $|\eta| < 3$ for PYTHIA samples and up to $|\eta| < 1.5$ for the reconstructed. From each of them, the forward-backward correlation strength (b) was extracted as described in 1.4. We call this method the direct method.

The dispersion coefficients are determined by Eqs. 4.5, 4.3 and 4.4. Three forward-backward correlation strengths (forward, backward, and general) can then be derived following Eq. 4.2 for the same phase space coverage as the direct method. We call this method the dispersion method.

The two methods of calculation of the correlation strength are compared for the different analyzed samples, and the cut influence discussed, at the end of the chapter.

5.1 Multiplicity from PYTHIA

The generation with stand-alone PYTHIA is significantly faster than the full simulation. Different PYTHIA versions were tested, to see the effects of the same settings. Our first choice was PYTHIA version 5.720 (29 Nov 1995) with JETSET version 7.408 (see 3.1 and [Sjos01]). The procedure was to create samples of 5000 events that were processed and compared using the first version of the analysis code.

After a satisfactory tuning based on a comparison of particle production and some standard distributions with the output of the official production, the next step was to test the generation settings in ROOT. ROOT can be configured and compiled with a wrap over PYTHIA that is allowing the user to directly generate user-defined ROOT files. The chosen flavor was PYTHIA version 6.319. In Fig. 5.1 we show a comparison between these two PYTHIA flavors. Despite the same tuning, the resulting MD is not the same. Since actual versions are considered more correct, it was decided to use PYTHIA version 6.319, that is also 'embedded' as one of the ALICE event generators.

To check if the KNO scaling applies to PYTHIA results we generated small samples (5000 events) with a MB tuning and energies from 0.1 TeV to 14 TeV. To make it more general, no pseudorapidity range was selected.

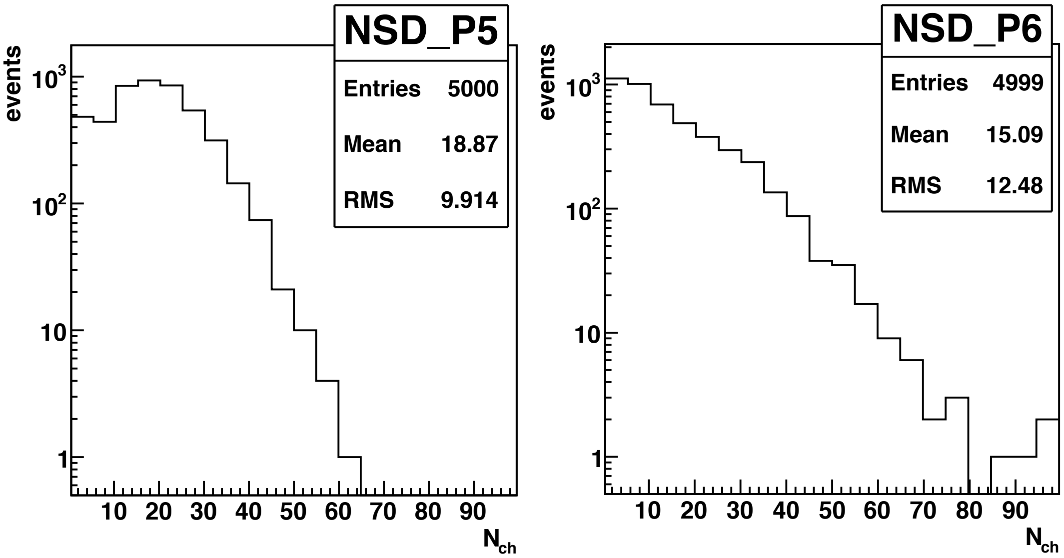

Figure 5.1: Multiplicity distributions for 5000 proton-proton collision events at an energy $\sqrt{s} = 14$ GeV with a Non-Single-Diffractive (NSD) tuning and an pseudorapidity cut of $|\eta| < 0.9$. Up : PYTHIA version 5.720. Down : PYTHIA version 6.319 (inside ROOT). Both PYTHIA versions are FORTRAN-based.

The multiplicity distributions obtained from PYTHIA 6.319 run at various energies, in fact, lay in the same range when plotted using KNO variables (Fig. 5.2). Thus, a scaling seems manifest in PYTHIA 6.319. However, it is also visible that the distribution corresponding to the highest energy (14 TeV) is below the one of the lowest energy (1 TeV) for low values of the KNO scaling variable $N_{ch}/\langle N_{ch}\rangle$ and above for high values. The difference between distributions was, at this point, attributed to the sample size and the existence of a scaling assumed in PYTHIA 6.319, letting the clarification of it to a more detailed analysis by a fit. The nature of this fit will be discussed in Section 5.3.

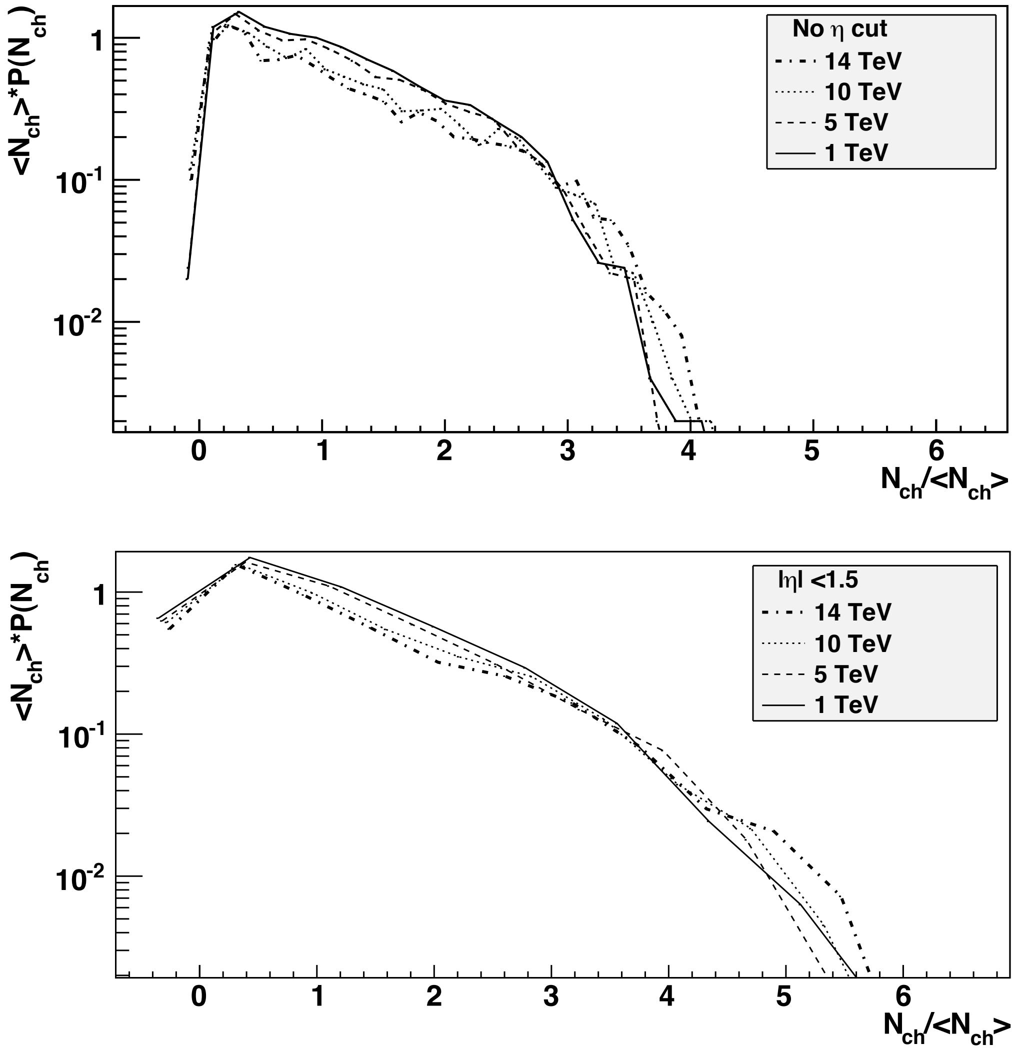

Figure 5.2: KNO scaling for PYTHIA 6.319 proton-proton events, two different pseudorapidity ranges. Up : multiplicity distribution obtained without any pseudorapidity cut, in KNO variables. Down : multiplicity distribution in KNO variables after a cut of $|\eta| < 1.5$. Particles with pseudorapidities above the cut were not taken into account for the final multiplicity distribution. Each multiplicity distribution was obtained from 5000 proton-proton collision events generated with a Non-Single-Diffractive (NSD) tuning.

5.2 Multiplicity from MC Truth and ESDs

The multiplicity analysis should be done using only these particles that fall into the fiducial acceptance of the detector. In order to define the fiducial pseudorapidity range for our analysis we compare in Fig. 5.3 the pseudorapidity distribution of the reconstructed charged particle tracks (ESDs) with the original distribution of the generated particles (Monte Carlo Truth, MCT). The unbiased distribution of primary particles taken directly from the event generator is also shown (PYT).

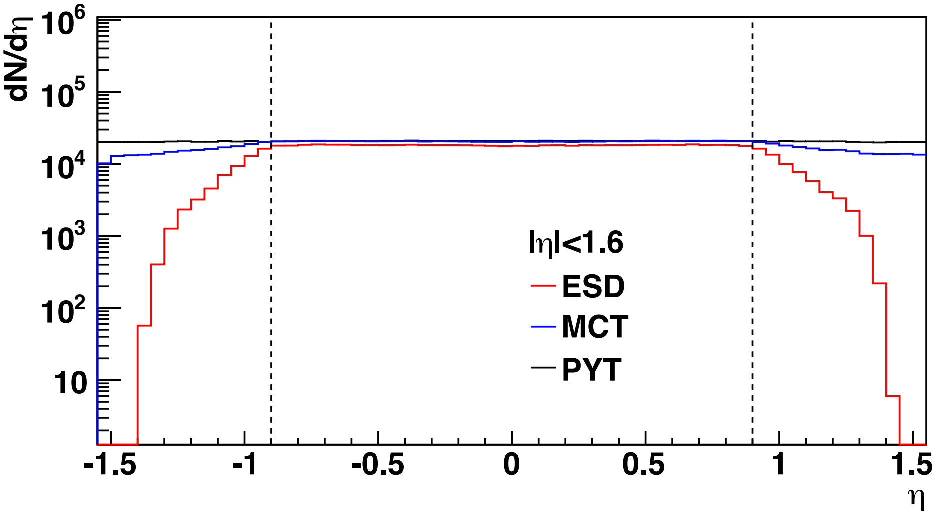

Figure 5.3: Pseudorapidity distribution of charged particles from pp collisions at $\sqrt{s} = 10$ GeV from PYTHIA 6.319 (PYT), from the Monte Carlo events (MCT), and of the reconstructed charged particle tracks (ESD). Dashed lines show the nominal TPC acceptance of $|\eta| < 0.9$.

The reconstruction efficiency clearly drops when going beyond the nominal TPC acceptance of $-0.9 < \eta < 0.9$ and thus for the multiplicity analysis we will consider only tracks falling into this region. The comparison between the multiplicity distributions from PYTHIA, from Monte Carlo, and of the reconstructed ESD tracks is shown with and without this cut in Fig. **??**. As can be seen in the right panel, applying the cut brings the three distribution closer to each other.

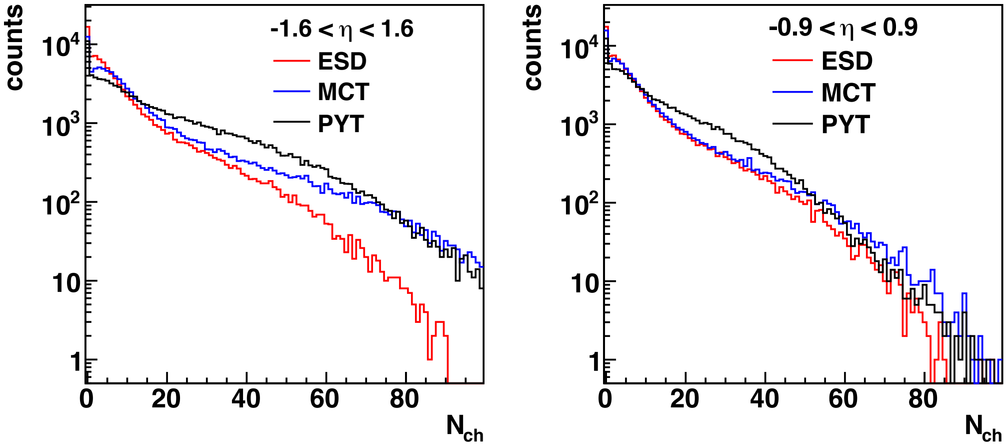

Figure 5.4: Multiplicity distribution (MD) of charged particles from pp collisions at $\sqrt{s} = 10$ GeV from PYTHIA 6.319 (PYT), from the Monte Carlo events (MCT), and of the reconstructed tracks (ESD). Left: no fiducial pseudorapidity cut. Right: with fiducial pseudorapidity cut. Standard track cuts were applied. The multiplicity distributions get close to each other once the pseudorapidity range is restricted to the detector acceptance.

As was discussed in Section 2.2, the detector has a minimum transverse momentum below which particles are lost or measured with very low efficiency, due to the magnetic field or multiple scattering [Gros08]. For the nominal magnetic field of ALICE, B=0.5 T, the p_t cut-off has been estimated to be around 0.12 GeV/c for pions in the TPC. We note that this value depends on the particle species and compare, in Fig. 5.5, the original and the reconstructed transverse momentum distributions.

The distributions coincide starting from 0.2 GeV/c. (The fact that the Pythia spectrum is harder than the other two does not matter for this study.) We thus adopt the $p_t > 0.2$ GeV/c cut for our multiplicity studies. The multiplicities with and without this cut are compared in Fig. 5.6. The cut brings the generated (MCT) and reconstructed (ESDs) multiplicity distributions closer to each other.

Even after restricting the multiplicity analysis to the fiducial acceptance the reconstructed multiplicity can differ from the original one. One of the

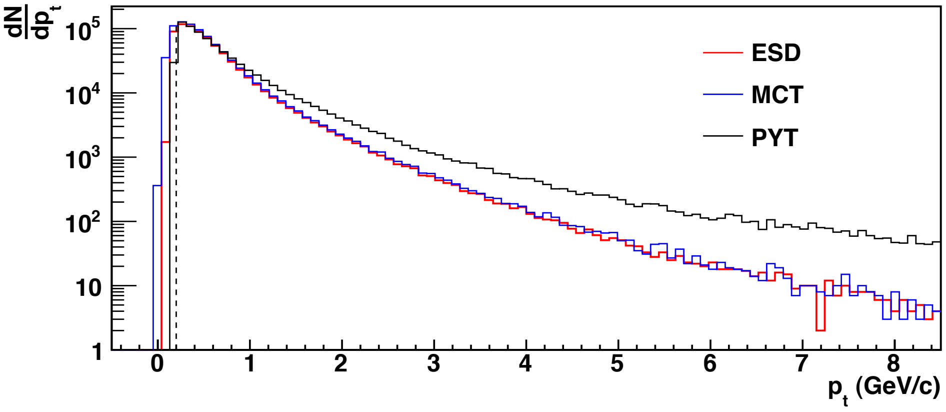

Figure 5.5: Transverse momentum spectra from Pythia 6.319 (PYT), Monte Carlo (MCT), and from the reconstructed events (ESD) for simulated pp collisions at $\sqrt{s} = 10$ GeV, with and without the p_t cut. Only the standard cuts were applied to ESDs and MCTs. The proposed p_t cut (0.2 GeV/c) is marked with a dashed line.

reasons for discrepancy is the production of secondary particles by the interaction of the primary ones with the material of the detector. The reconstructed multiplicity can be higher because of these tracks if they are not properly removed from the signal, or lower if the cuts are overdone. A detailed comparison between the mean multiplicities of the original and the reconstructed tracks, obtained after applying the fiducial acceptance cuts, is shown in Fig. 5.7.

The Monte Carlo particles and the reconstructed tracks (red and black symbols, respectively) agree reasonably well when the fiducial acceptance cuts $-0.9 < \eta < 0.9$ and $p_t > 0.2$ GeV/c are applied.

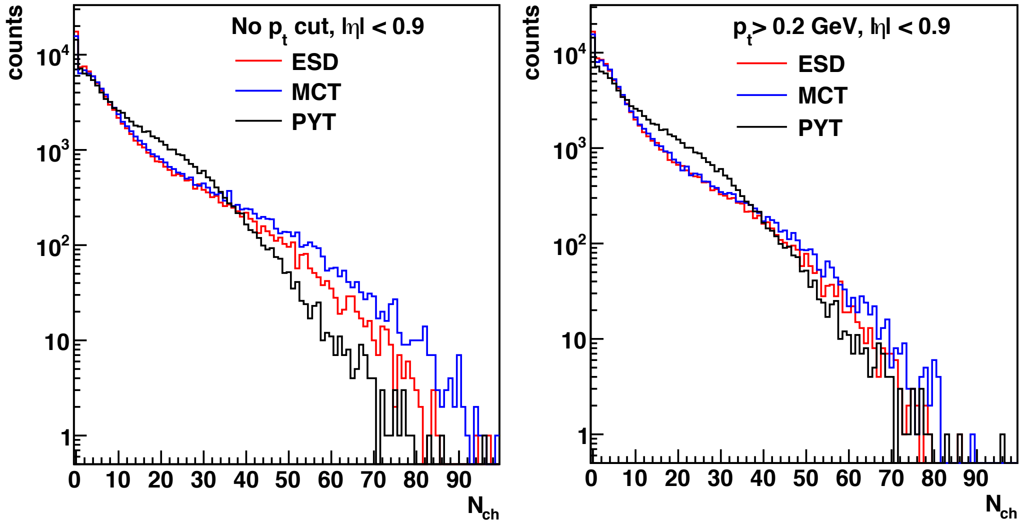

Figure 5.6: Multiplicity distributions (MDs) from Pythia 6.319 (PYT), reconstructed events (ESD), and the corresponding Monte Carlo Truth (MCT) from simulated collisions at $\sqrt{s} = 10$ GeV in our fiducial volume (TPC central acceptance). Left: MDs without any p_t cut. Right: MDs after a p_t cut of 0.2 GeV/c.

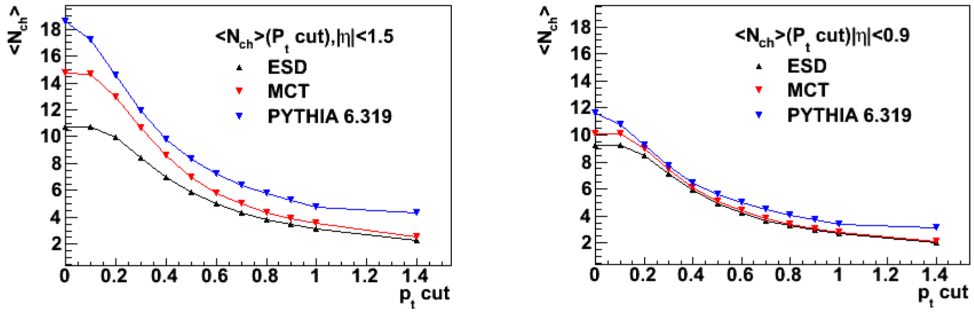

Figure 5.7: Dependence of the mean charged particle multiplicity $\langle N_{ch} \rangle$ from PYTHIA 6.317 (blue), Monte Carlo (red) and ESDs (black) on the η and p_t cuts. All samples were generated for pp collisions at $\sqrt{s} = 10$ GeV.

5.3 Parametrization of the multiplicity distribution

Previous results for PYTHIA pp events at $\sqrt{s} = 0.2$ TeV have shown that it was possible to fit the multiplicity distribution with a single negative binomial (NB) distribution [Dash09]. As shown in Fig. 5.8, the fit function reproduces the PYTHIA points over four orders of magnitude.

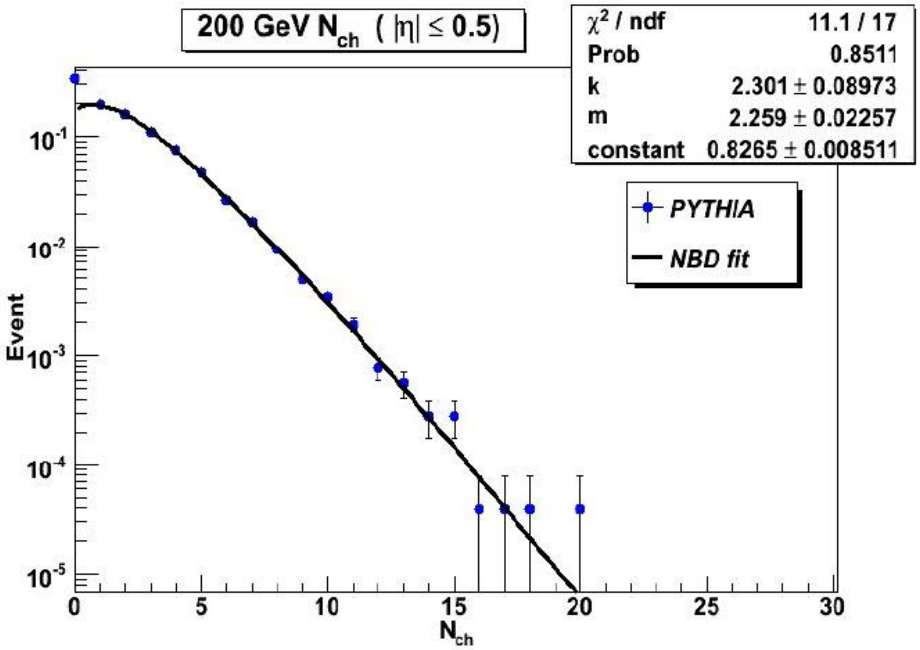

Figure 5.8: Fit of a multiplicity distribution from PYTHIA pp events at $\sqrt{s}$ = 0.2 TeV by a negative binomial distribution. Figure taken from [Dash09].

Our attempt to perform an analogous fit to the multiplicity distribution of pp collisions at $\sqrt{s}$=10 TeV failed because the distribution has two components which cannot be reproduced simultaneously by a single binomial fit function. This is shown in Fig. 5.9. The multiplicity distribution (histogram) was obtained from 90000 PYTHIA 6.319 pp events at $\sqrt{s}$ = 10 TeV. The

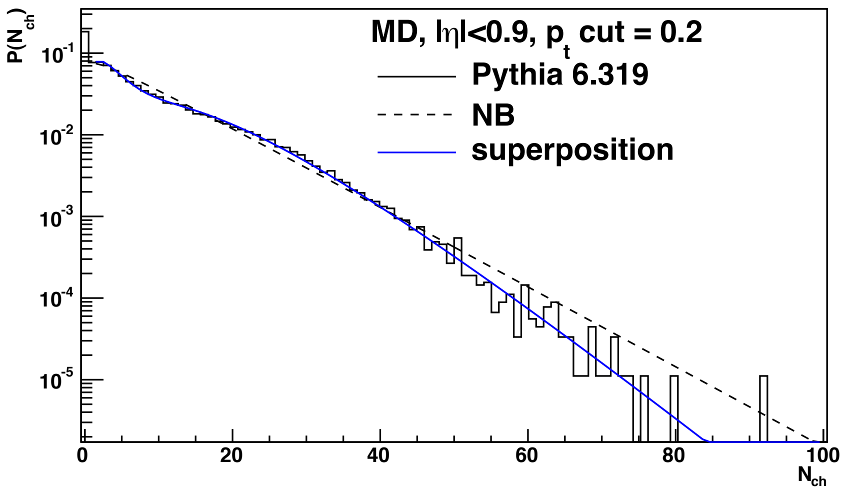

Figure 5.9: Charged particle multiplicity distribution from PYTHIA 6.319 pp events at $\sqrt{s} = 10$ TeV fitted by a single binomial (dashed line) and by a superposition of two binomial distributions (solid blue line).

fiducial acceptance cuts $-0.9 < \eta < 0.9$ and $p_t > 0.2$ GeV/c were applied. The single binomial fit (dashed line) clearly underestimates the bump at N_{ch}=25 and overestimates the high multiplicity tail.

A much better fit can be performed using a sum of two binomial distributions (blue solid line) accounting for the low and high multiplicities, respectively. This observation holds also for the multiplicity distributions from Monte Carlo and from the reconstructed ESDs (Fig. 5.10). Each NB distribution is characterized by two parameters, the average multiplicity $\overline{n}$ and the number of contributing cells k. Alternatively, in the language of the clan model, one can use the average number of clans $\overline{N}$ and the average number of particles per clan $\overline{n_c}$. The relation between the two sets of parameters is

$$\begin{aligned} \overline{N} &= k \ln\left(1 + \overline{n}/k\right) && (5.1) \\ \overline{n_c} &= \overline{n}/\overline{N}\ . && (5.2) \end{aligned}$$

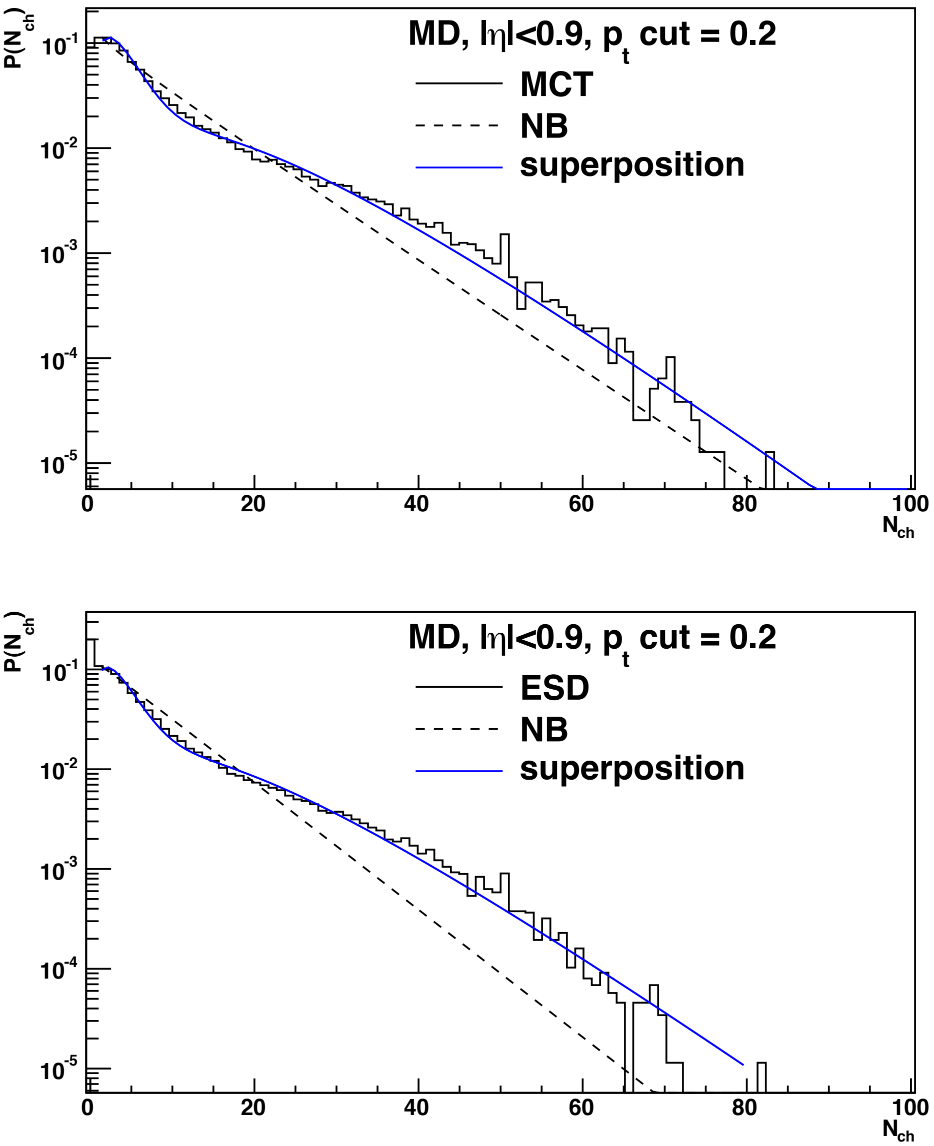

Figure 5.10: Charged particle multiplicity distribution from Monte Carlo (MCT) and from reconstructed events (ESD) fitted by a single binomial (dashed line) and by a superposition of two binomial distributions (solid blue line).

The complete fit function was

$$\begin{aligned} & P_n(\overline{n}_1, k_1, \overline{n}_2, k_2, w) = \\ = \quad & (1-w)\ \frac{k_1(k_1+1)...(k_1+n_1-1)}{n_1!}\ \frac{{\overline{n}_1}^{n_1}\ {k_1}^{k_1}}{(\overline{n}_1+k_1)^{n_1+k_1}} \\ + \quad & w\ \frac{k_2(k_2+1)...(k_2+n_2-1)}{n_2!}\ \frac{{\overline{n}_2}^{n_2}\ {k_2}^{k_2}}{(\overline{n}_2+k_2)^{n_2+k_2}}\ . \end{aligned}$$

The results of the fits are collected in Table 5.1. The subscripts 1 and 2 refer to high and low multiplicity components, respectively. The ESD parameters are lower by 5-8% than the respective MCT values. The respective correction would need to be applied when analyzing actual experimental data.

sample	$\sqrt{s}$ (TeV)	k_1	k_2	$\overline{n}_1$	$\overline{n}_2$
PYT	10	2.97 ± 0.09	1.85 ± 0.01	14.77 ± 0.18	2.86 ± 0.07
MCT	10	2.61 ± 0.06	2.31 ± 0.02	16.90 ± 0.02	2.95 ± 0.03
ESD	10	2.51 ± 0.06	2.12 ± 0.01	15.94 ± 0.02	2.81 ± 0.03
UGO	14	2.0	3.4	14	4.9

Table 5.1: Results of a fit of two negative binomial distributions to the multiplicity distributions from PYTHIA 6.319 (PYT), from Monte Carlo (MCT), and from reconstructed events (ESD). The obtained fit parameters can be compared to theoretical calculations (UGO) [Ugoc05].

The Monte Carlo parameters in Table 5.1 are in rough agreement (20-40%) with the theoretical calculations from [Ugoc05].(One should keep in mind the difference in the collision energy.) There, the two components were identified with soft and semi-hard events, the latter characterized by a high momentum transfer between the collision partners. In order to verify whether such a classification is consistent with our simulation we compare, in Fig. 5.11, the transverse momentum distributions for events with low (< 10) and high (>40) multiplicities. The particles emerging from high multiplicity events turn out to have, on average, higher transverse momenta. This confirms the picture of soft and semi-hard collisions leading to events with low and high multiplicities, respectively.

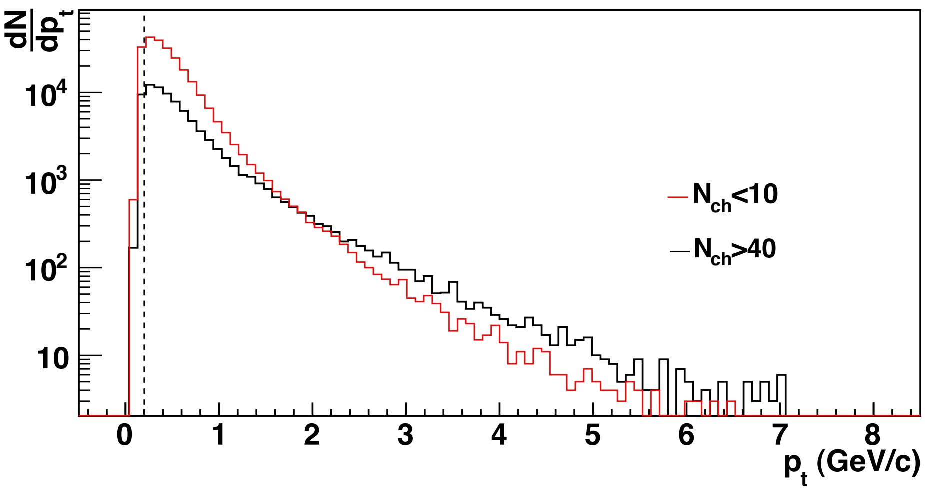

Figure 5.11: Transverse momentum distributions from 90000 simulated pp collisions at $\sqrt{s}$ = 10 TeV after a high (N_{ch} >40) and low (N_{ch} <10) multiplicity cut. A pseudorapidity interval of η <0.9 is selected, corresponding to the TPC central acceptance. No normalization is done. The dashed line marks the applied p_t cut of 0.2 GeV/c. It is shown that events with high multiplicity (N_{ch} >40) have, on the average, higher p_t.

The distinct high multiplicity component developing in the multiplicity distributions at high energies constitutes a clear violation of the KNO scaling. Comparing the two panels of Fig. 5.4 one can see that the effect gets stronger when the pseudorapidity acceptance is restricted. Finally, it should be noted that the second bump becomes manifest only with sufficient event statistics. In fact, the distributions used to test the KNO scaling in PYTHIA, shown in Fig. 5.2, extend only over 2-3 orders of magnitude which is not sufficient to detect the second component.

5.4 Forward-backward correlations

The forward-backward correlation analysis method was introduced in Sec. 4.2. We run the analysis on $5 \cdot 10^5$ pp events at $\sqrt{s} = 10$ TeV generated with PYTHIA 6.319 (PYT), and on the same number of Monte Carlo (MCT) and reconstructed events (ESD) from the full simulation of the ALICE detector. The PYTHIA generator contains both short and long range correlations. From the comparison between the results obtained with the particles propagated through the detector (MCT) with those from the reconstructed tracks we learn about the apparatus response.

We start by presenting, in Figs. 5.12, 5.13, and 5.14, the respective forward-backward multiplicity correlation plots. The forward and backward η bins have a width of 0.2 and their centers are separated by an interval of $\Delta\eta = 0.2$, 0.6, or 1.0. The left column of these figures shows the accumulated correlation histograms. The histograms are cut in slices according to $n_{ch}(F)$ and the average $n_{ch}(B)$ is determined for each slice. The result, shown in the respective plots on the right side, is fit by a straight line (Eq. 4.1). The slope of the fit b represents the correlation strength. We will refer to this as the direct method. As one can see, there is a clear positive correlation between the forward and backward multiplicities.

Alternatively, the correlation coefficient can be determined from Eq. 4.6. The three variants of this method, which differ by the way how the dispersion is calculated, should give the same results if the forward and backward acceptances are identical. This is the case for the ALICE detector. We verify this by plotting all three in Fig. 5.15. The difference is, in fact, about 1% in our region of interest. In the following we thus use the general b_g rather than the more popular b_F. This method will be referred to as the dispersion method.

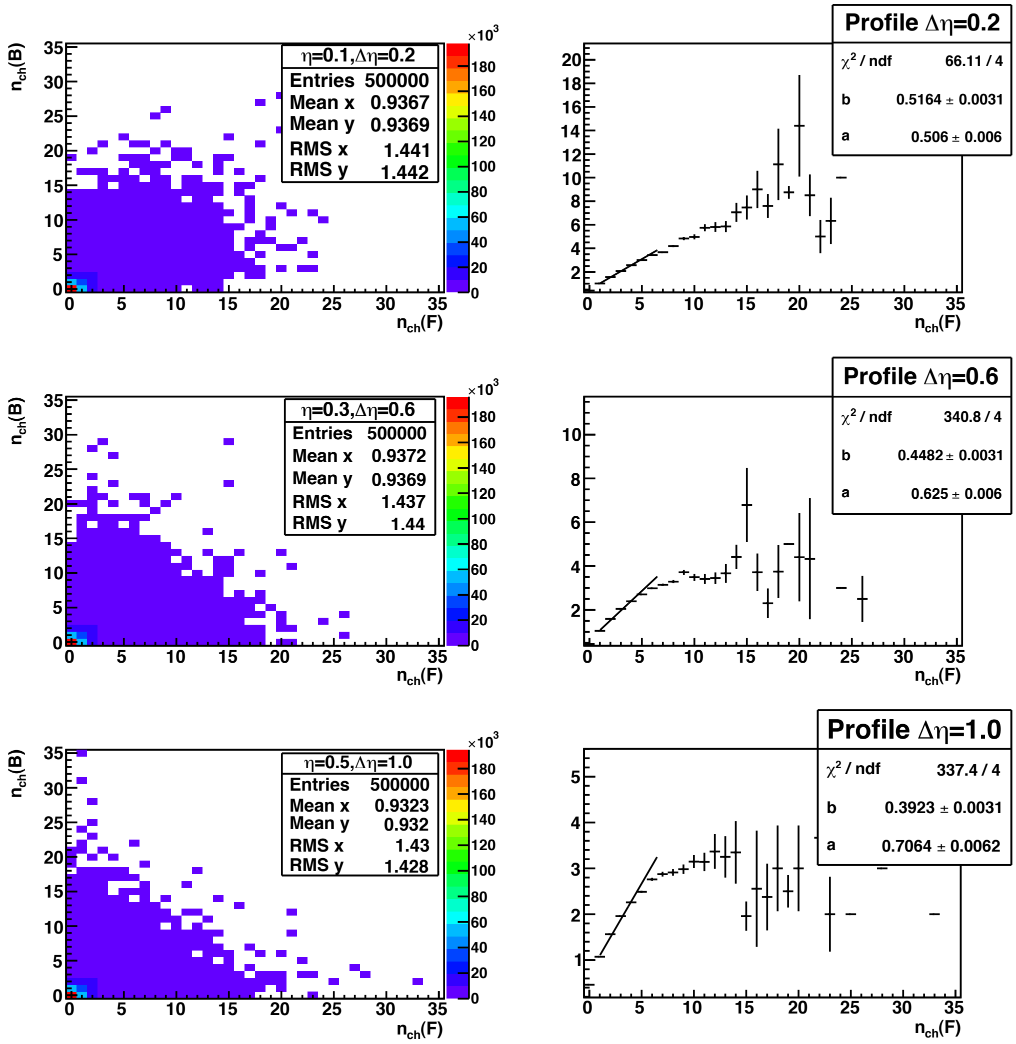

Figure 5.12: Forward-backward multiplicity correlation plots for standalone PYTHIA simulated pp events at $\sqrt{s} = 10$ TeV. The forward and backward η intervals are both 0.2 units wide. The results for the η windows centered at ± 0.1, ± 0.3, and ± 0.5 are shown in the upper, middle and bottom panels, respectively as correlation plots (left) and its fitted projections (right). Pseudorapidity gaps $\Delta\eta$ are defined from the center of the forward interval to the center of backward interval. No p_t cut is applied.

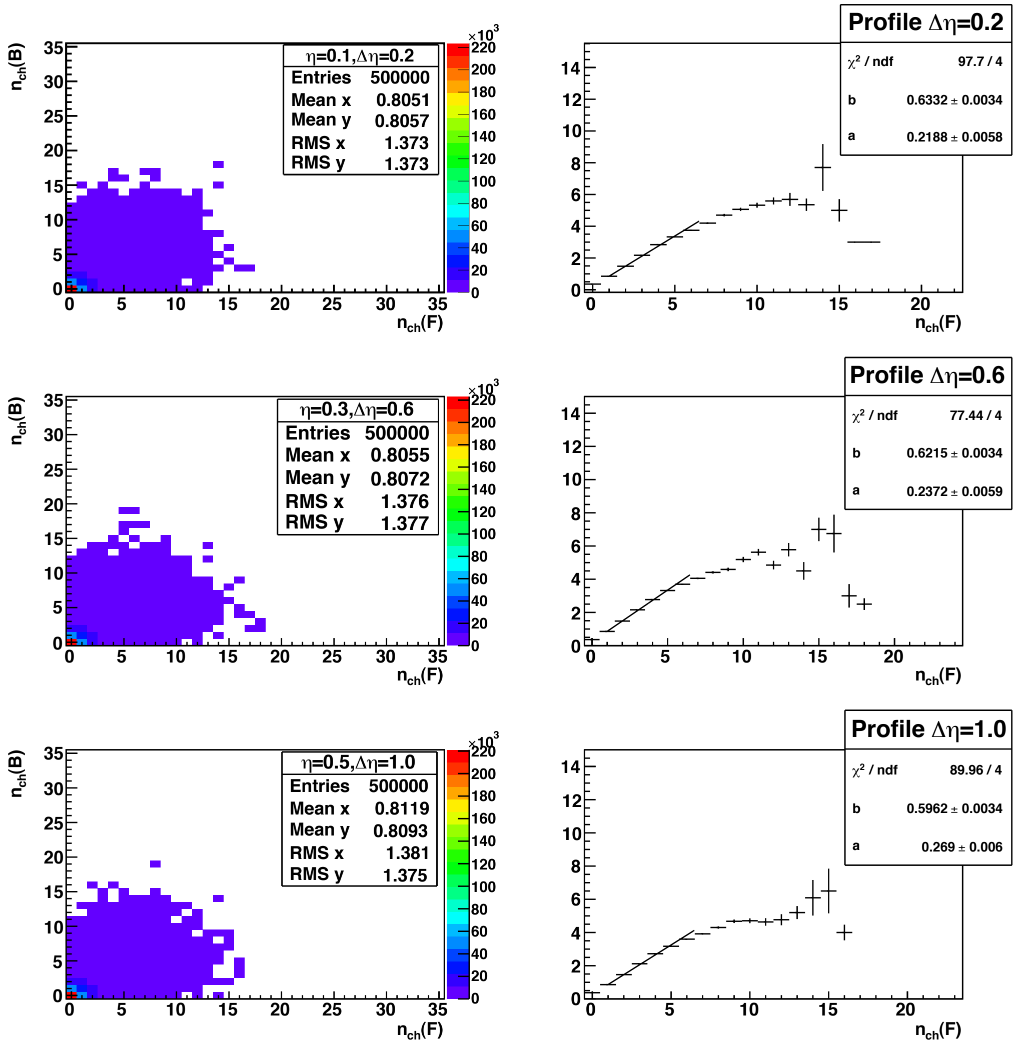

Figure 5.13: Forward-backward multiplicity correlation plots for the Monte Carlo Truth (MCT) of reconstructed tracks (ESD) of ALICE simulated pp events at $\sqrt{s} = 10$ TeV. The forward and backward η intervals are both 0.2 units wide. The results for the η windows centered at ± 0.1, ± 0.3, and ± 0.5 are shown in the upper, middle and bottom panels, respectively as correlation plots (left) and its fitted projections (right). Pseudorapidity gaps $\Delta\eta$ are defined from the center of the forward interval to the center of backward interval. No p_t cut is applied.

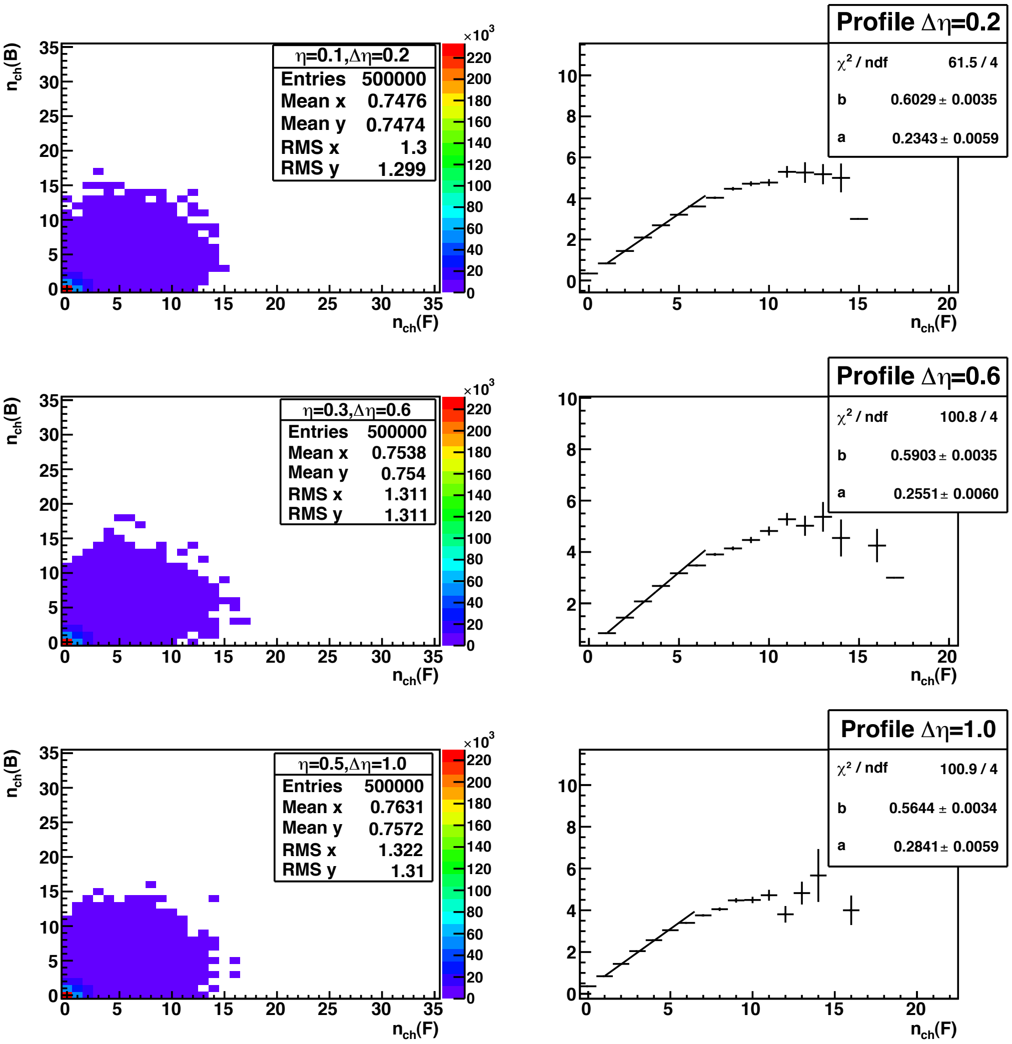

Figure 5.14: Forward-backward multiplicity correlation plots from reconstructed tracks (ESD) of ALICE simulated pp events at $\sqrt{s}$ = 10 TeV. The forward and backward η intervals are both 0.2 units wide. The results for the η windows centered at ±0.1, ±0.3, and ±0.5 are shown in the upper, middle and bottom panels, respectively as correlation plots (left) and its fitted projections (right). Pseudorapidity gaps $\Delta\eta$ are defined from the center of the forward interval to the center of backward interval. No p_t cut is applied.

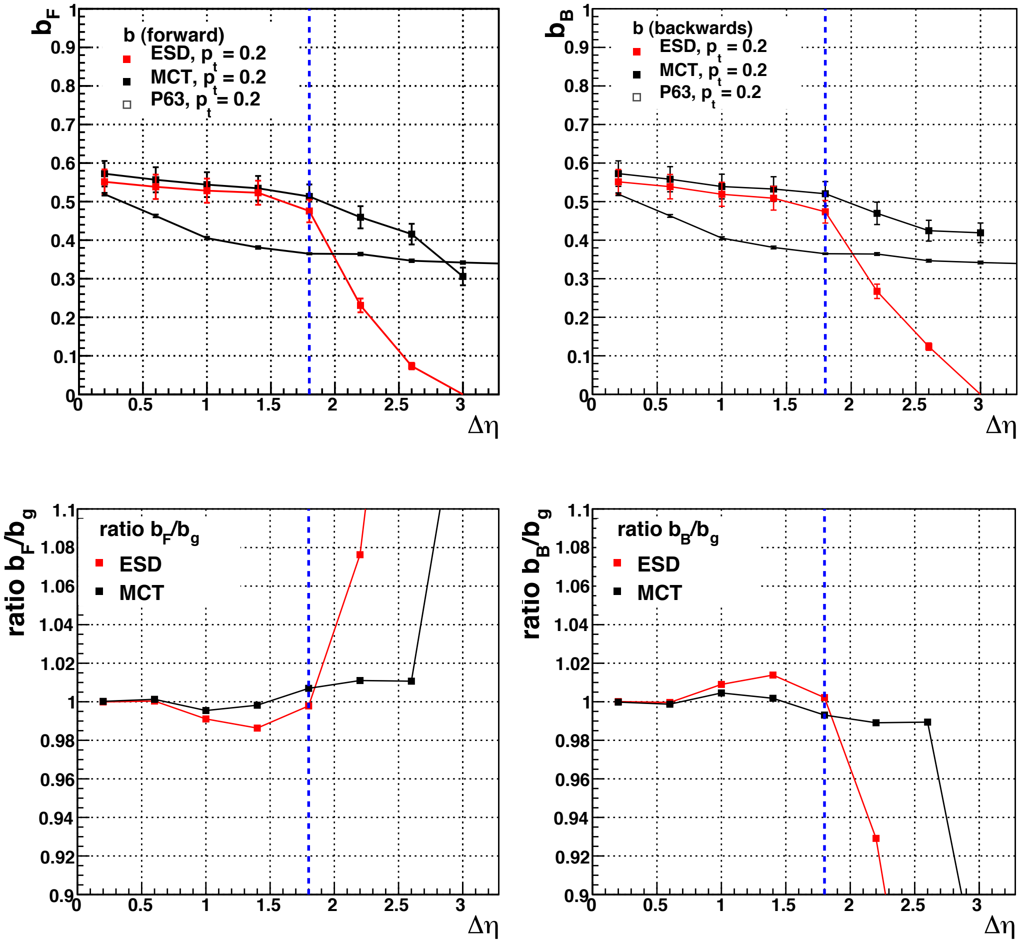

Figure 5.15: Forward-backward correlation strength in simulated pp events at $\sqrt{s} = 10$ TeV as a function of the pseudorapidity gap. The values and their ratios are shown in the upper and lower parts of the figure, respectively. The three dispersion method flavors agree within 2%.

The comparison between the two methods of the correlation strength determination is shown in Fig. 5.16. The dispersion method gives values that are 10-15% lower than the direct method. The $p_t > 0.2$ GeV/c cut reduces the correlation strength by 3%.

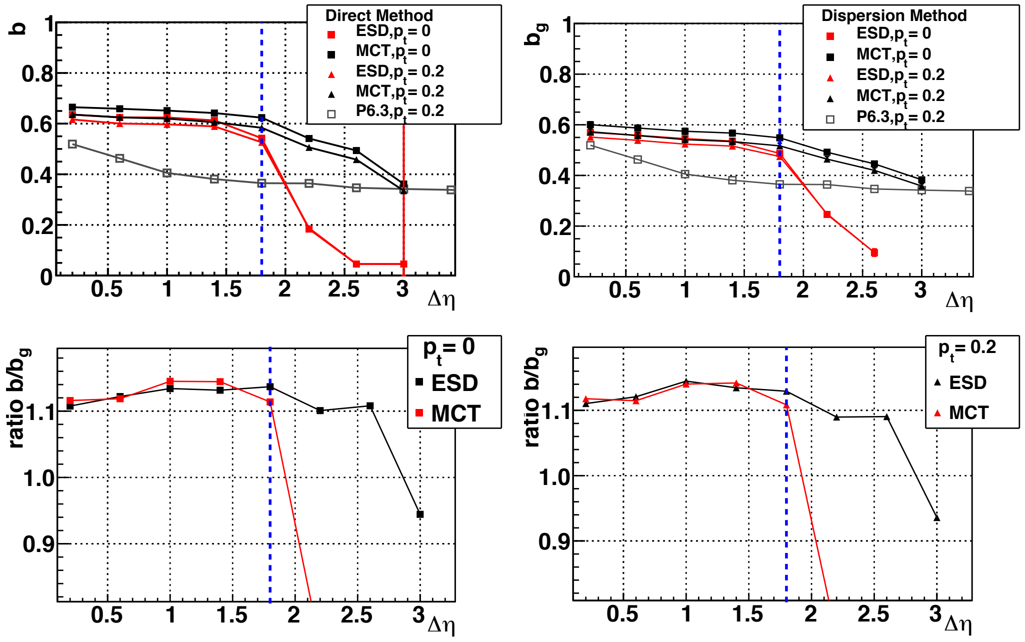

Figure 5.16: Forward-backward correlation strength in simulated pp events at $\sqrt{s} = 10$ TeV as a function of the pseudorapidity gap. The values and their ratios are shown in the upper and lower parts of the figure, respectively. The direct and the dispersion methods agree within 15%.

The correlation strength determined directly can be compared to the $p\bar{p}$ collision results obtained by E735 at Fermilab [Alex95] where the same method was used (Fig. 5.17). The dependence of our b on the size of the pseudorapidity gap is weaker than in the case of the E735 data. The pure PYTHIA correlations, on the other hand, rapidly decrease between $\Delta\eta = 0$ and $\Delta\eta = 1.0$. This might be interpreted as a signature of short range correlations present in PYTHIA. Concerning the magnitude of the correlations, our values are comparable to the ones observed by E735 at a collision en-

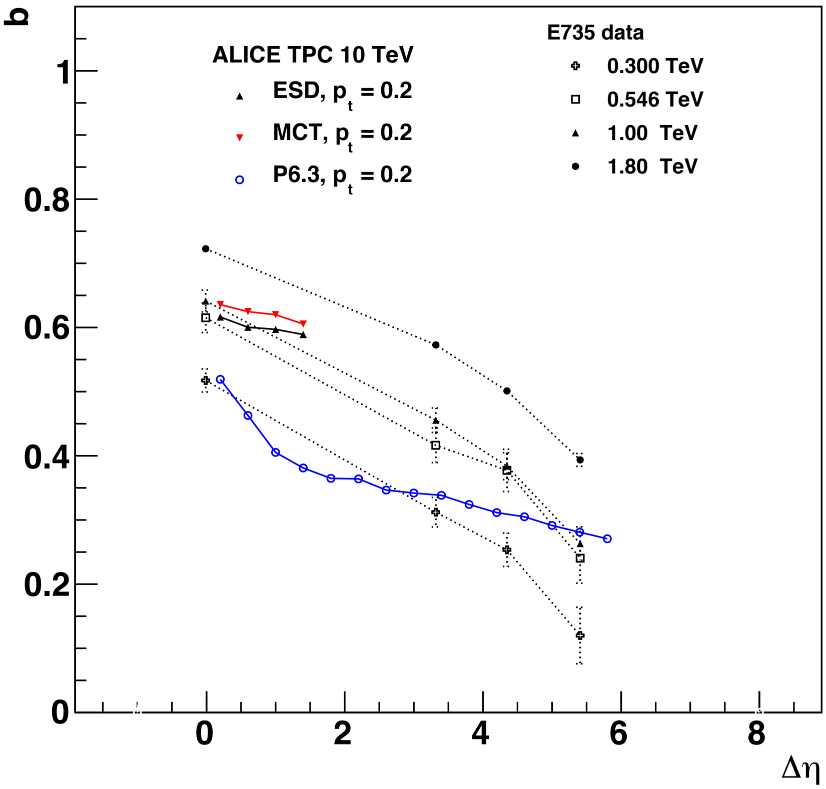

Figure 5.17: Dependence of the correlation strength on the size of the pseudorapidity gap. We compare E735 $p\bar{p}$ results [Alex95] with the output of an analysis of simulated data at $\sqrt{s} = 10$ TeV (ESDs) and the corresponding Monte Carlo Truth (MCT) for the TPC central acceptance $|\eta| < 0.9$ using a p_t cut of 0.2 GeV/c. The PYTHIA 6.319 dependence (P6.3) is also shown.

ergy of $\sqrt{s} = 0.3$ TeV. An extrapolation to 10 TeV would exceed our result significantly.

The pseudorapidity range over which the multiplicity fluctuations are correlated can be quantified by fitting an exponential to the $b(\Delta\eta)$ dependence:

$$b(\Delta\eta) \sim e^{-\frac{\Delta\eta}{\lambda}} \ . \qquad (5.3)$$

The pseudorapidity correlation length λ can be used to estimate the range of correlations in the coordinate space assuming that the rapidity and the space-time rapidity are roughly equal to each other. In classical systems, the correlation length is expected to diverge at the critical point. To get some feeling about the reliability of the so determined correlation length we compare, in Fig. 5.18, the fit of Eq. 5.3 to the correlation strength determined via the direct and the dispersion methods.

The correlation length obtained is on the order of 10-20 and, in nature, might point to existence of extended objects like color flux tubes or percolating strings [Brog09]. Unfortunately, the discrepancy between the correlation length obtained from Monte Carlo and from reconstructed events is significant. The correlation strength is nearly constant over the analyzed pseudorapidity gap range and thus the exponential fit is not stable. Obviously, the correlation length can only be measured reliably if its value is not much larger than the experiment's acceptance. We postpone the quantitative analysis of the statistical and systematic errors to the next section.

The fact that the correlation strength we obtained is lower than the experimental one is also visible in Fig. 5.19 where we plot b versus the collision energy. The multiplicity correlations shown in this figure were obtained for wide pseudorapidity intervals without a gap. Our value is 15% below the $a_0 + a_1 \ln \sqrt{s}$ extrapolation from the existing ISR, UA5, and E735 experimental data. The disagreement does not originate from the difference between the collision systems, $p\bar{p}$ versus pp. In fact, Pythia even predicts that the correlation strength in pp should be some 3% higher that in $p\bar{p}$ at the 10 TeV collision energy. The difference increases to about 30% when going down to ISR energies. This could be because pp collisions have more quark-diquark strings which contain more energy than quark-antiquark ones and thus lead to increased forward-backward correlations.

On the other hand, the UA5 and E735 results can be rather well reproduced by Pythia $p\bar{p}$ simulations once the pseudorapidity coverage is extended to $-3.0 < \eta < 3.0$, similar to the actual acceptance of the two experiments. This means that the difference between the simulated ALICE points in Fig. 5.19 and the extrapolation line from lower energies is primarily a trivial consequence of the ALICE central barrel acceptance being narrower than the acceptances of UA5 and E735.

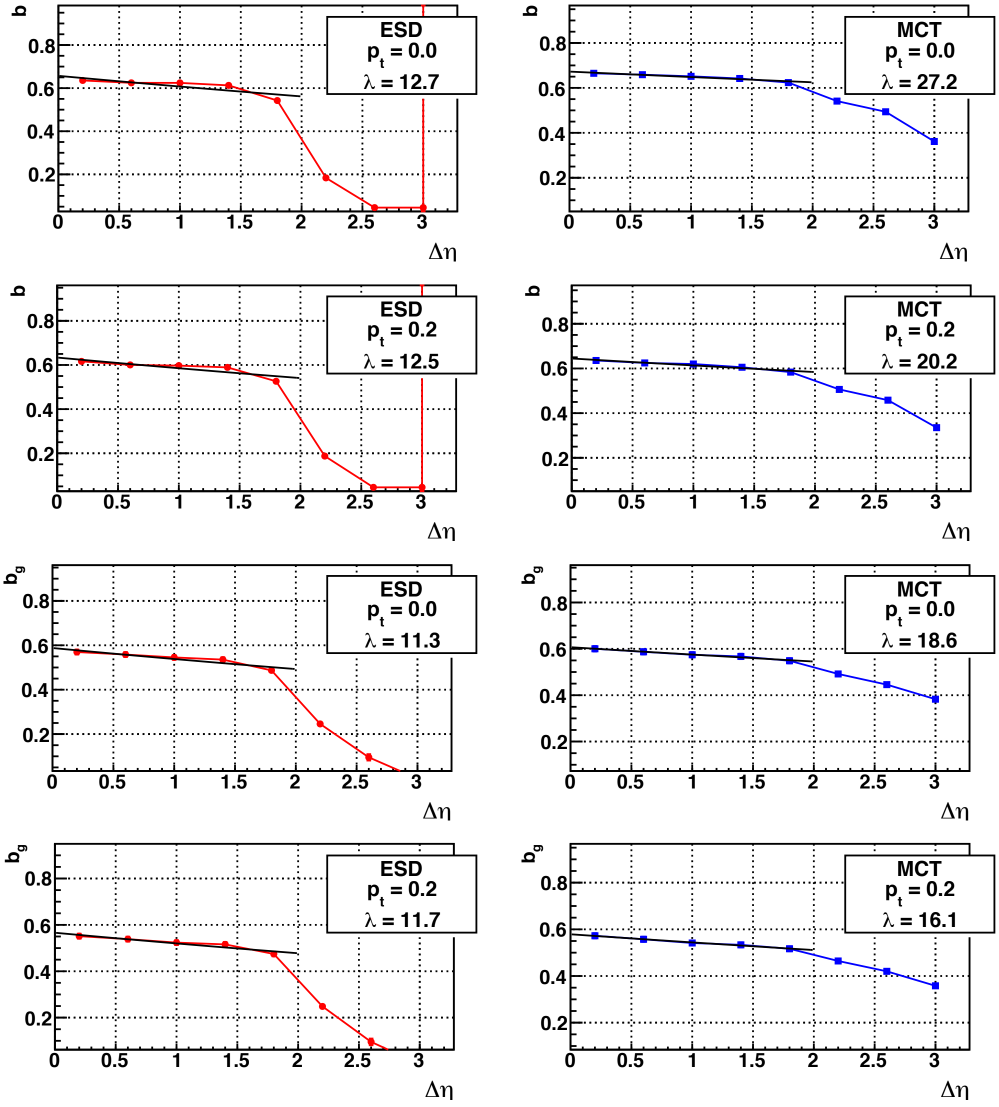

Figure 5.18: Fits of Eq. 5.3 to the dependence of the correlation strength b on $\Delta\eta$ for reconstructed tracks (ESD) and the corresponding MC Truth (MCT), for the direct (labeled b) and dispersion (labeled b_g) methods. Two values of the p_t cut were studied. Results are summarized in Table 5.2.

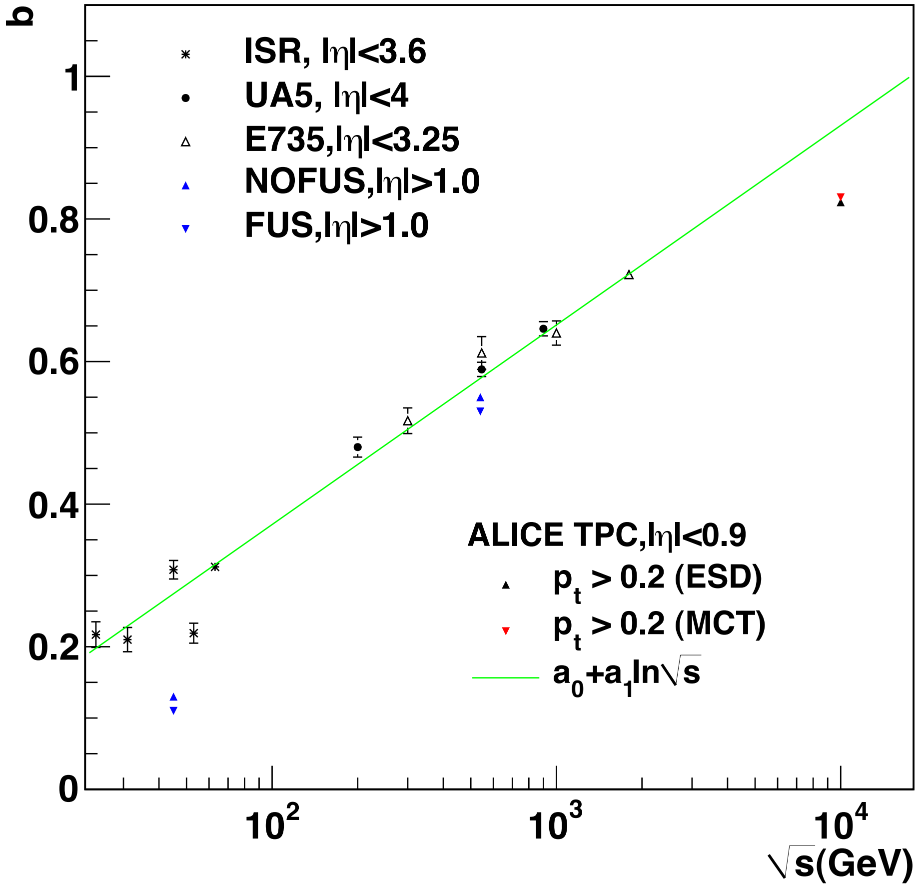

Figure 5.19: Energy dependence of the correlation strength b. Shown are experimental data from ISR pp collisions [Uhli78], UA5 $p\bar{p}$ [Anso88], E735 $p\bar{p}$ [Alex95], and the results of a string fusion model (labeled FUS when the string fusion is included, NOFUS when it is not included [Amel94]) together with the information from the analysis of the reconstructed tracks (ESD) and the corresponding MC Truth (MCT) of simulated pp collisions in the ALICE TPC.

5.5 Discussion of systematic errors

In this section we describe some checks performed to estimate the systematic errors of the analysis. In Fig. 5.20 we show in the left panel how the multiplicity from the reconstructed tracks (ESD) is correlated with its corresponding Monte Carlo Truth (MCT), and in the right one we demonstrate the absence of correlations between different events. The multiplicity has been measured in the central acceptance, $|\eta| < 0.9$.

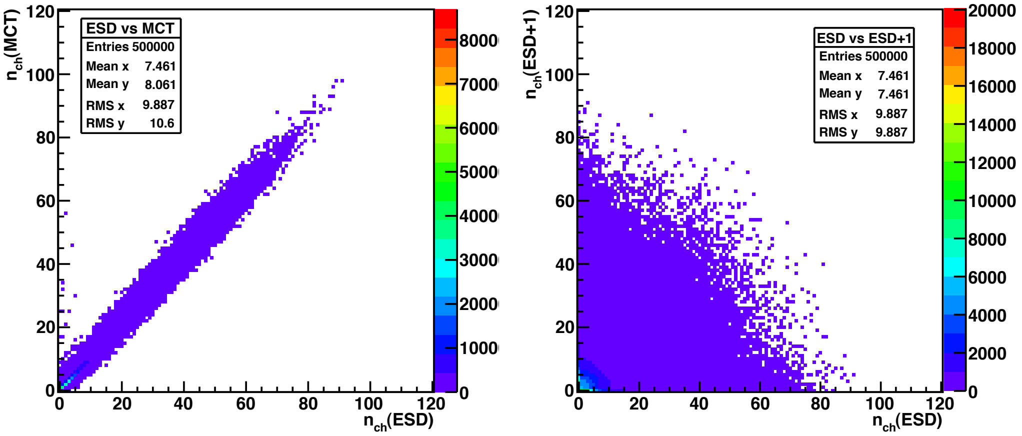

Figure 5.20: Correlation tests for event multiplicity. Left: multiplicity from reconstructed tracks (ESD) versus its corresponding Monte Carlo Truth (MCT). Right: multiplicity from one ESD versus the one of the next. Both analyses were performed over half a million of events generated at $\sqrt{s}$=10 TeV. A p_t cut of 0.2 GeV/c is applied.

Both histograms were subject to the procedure of the extraction of the correlation strength, yielding b=1.138±0.001 (no p_t cut), b=1.085±0.001 (p_t cut of 0.2 GeV/c) for ESD vs MCT, and b=0.009±0.004 (no p_t cut), b=0.018±0.002 (p_t cut of 0.2 GeV/c) for the event mixing case. A Monte Carlo multiplicity equal to the reconstructed one (ESD) should give a b=1.0. The correlations obtained with event mixing are negligible as expected.

As seen in the previous subsections the correlation strength in PYTHIA, MCT, and ESD differ by 0.05-0.1, depending on $\Delta\eta$ (Fig. 5.21). We attributed this to the combined detector response and not to the analysis procedure and declare this to be the systematic error of the method.

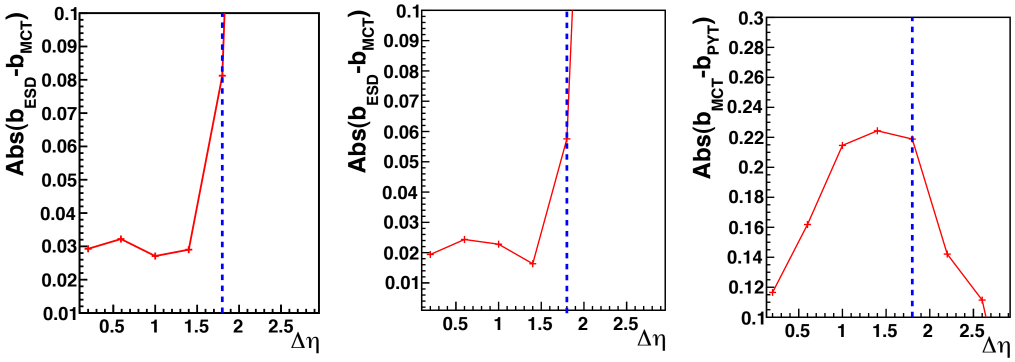

Figure 5.21: Systematic errors. Left: difference between correlation strength from reconstructed tracks (b_{ESD}) and the one corresponding to its Monte Carlo Truth (b_{MCT}), no p_t cut. Center: difference between b_{ESD} and b_{MCT} after a p_t cut of 0.2 GeV/c is applied. Right: difference between correlation strength from Monte Carlo Truth (MCT) and the one given by PYTHIA after p_t cut of 0.2 GeV/c is applied. Half a million of collisions at $\sqrt{s}$=10 TeV were analyzed.

The choice of forward and backward hemispheres is arbitrary for symmetric collision systems. We checked for trivial mistakes by swapping the two multiplicities. The correlation strength remains unchanged (Fig. 5.22).

The difference in the correlation length λ between ESD and MCT information is present in all the acquired correlation strengths, for both studied cuts (p_t =0.2 GeV/c, p_t =0.0 GeV/c). The results are summarized in Table 5.2 and visualized in Fig. 5.23. The error of the dispersion method is larger that that of the direct method and stays constant when a higher or lower number of events is being analyzed, pointing to the non-exponential shape of $b(\Delta\eta)$ as its origin. Therefore, the error is declared as systematic for the dispersion method. Concerning the difference between ESD and MCT, the error bars in Fig. 5.23 suggest that it can be of a statistical origin. The clearly smaller correlation length from PYTHIA ($\lambda \approx 5$), on the other hand, becomes similar to the MCT and ESD ones if the exponential fit is performed in the $\Delta\eta > 1.8$ region. This is consistent with the steep slope of the

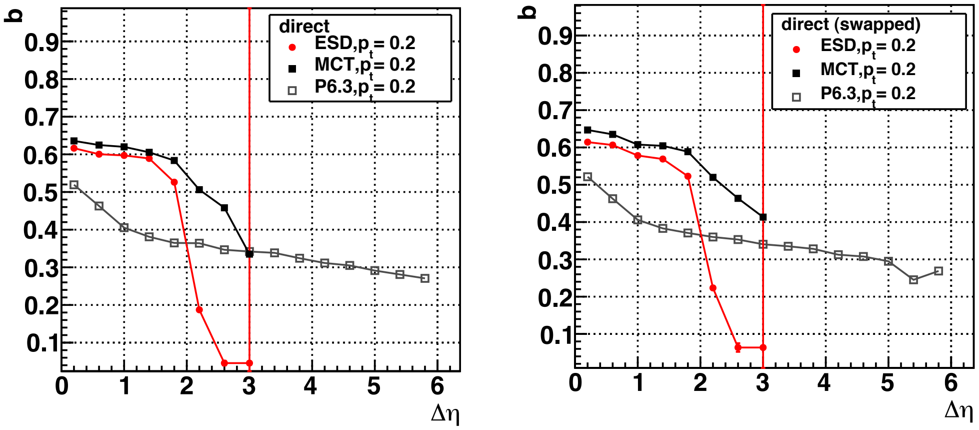

Figure 5.22: Correlation strength b from the direct method after swapping forward and backward regions for PYTHIA 6.319 (P6.3), Monte Carlo Truth (MCT), and the reconstructed (ESD) events. A p_t = 0.2 GeV/c cut was applied for all samples.

PYTHIA points at low $\Delta\eta$ in Fig. 5.18 that we interpreted as a sign of short range correlations.

λ	ESD	MCT	PYT
b (p_t =0.0)	12.73 ± 0.81	27.24 ±3.14	4.83 ± 0.11
b (p_t =0.2)	12.58 ± 0.84	20.20 ±1.95	4.66 ± 0.01
b_g (p_t =0.0)	11.36 ±2.03	18.64 ±5.49	5.11 ± 0.51
b_g (p_t =0.2)	11.76 ±2.19	16.11 ±4.11	5.20 ± 0.13
b_F (p_t =0.0)	11.42 ±6.07	20.10 ±18.93	5.83 ± 1.32
b_F (p_t =0.2)	11.12 ±5.78	16.78 ±13.21	5.16 ± 1.58
b_B (p_t =0.0)	11.22 ±5.79	17.39 ±14.09	5.45 ± 0.98
b_B (p_t =0.2)	12.37 ±7.09	15.49 ±11.21	5.15 ± 1.50

Table 5.2: The correlation length determined using the direct method (labeled b) and the dispersion method (b_g, b_F, b_B), from PYTHIA 6.319 (PYT), Monte Carlo Truth (MCT), and reconstructed pp events (ESD) at $\sqrt{s}$=10 TeV.

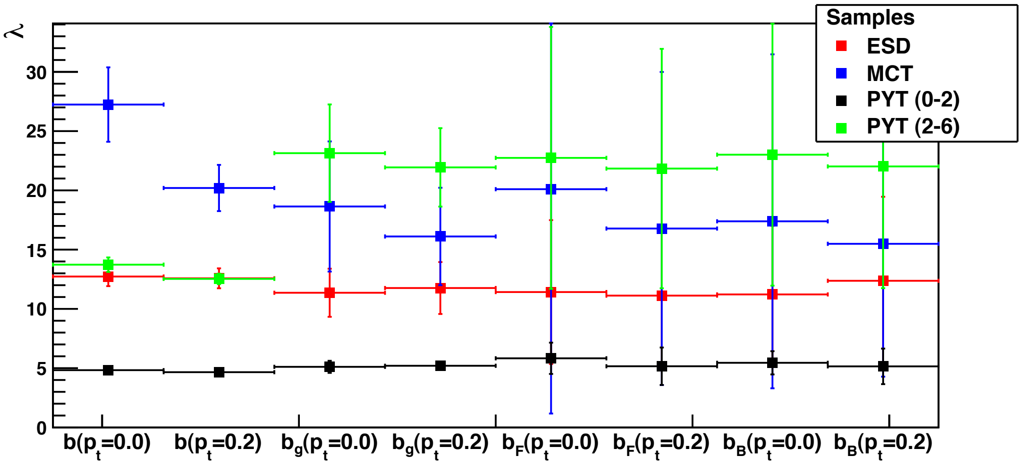

Figure 5.23: Comparison of correlation lengths λ from two methods for the three samples. The difference between the Monte Carlo Truth (MCT) and the reconstructed events (ESD) is statistically not significant. The PYTHIA correlation length (PYT(0-2)) becomes similar to the other two (PYT(2-6)) once the short range correlations are suppressed (see text).

Chapter 6

Analysis results for cosmic ray events

The analysis was tested on data taken during the ALICE TPC cosmic run of June 2008 that was reconstructed using the official framework. The resulting multiplicity distribution (MD) is shown in Fig. 6.1, and forward-backward (FB) multiplicity correlation plots in Fig. 6.2.

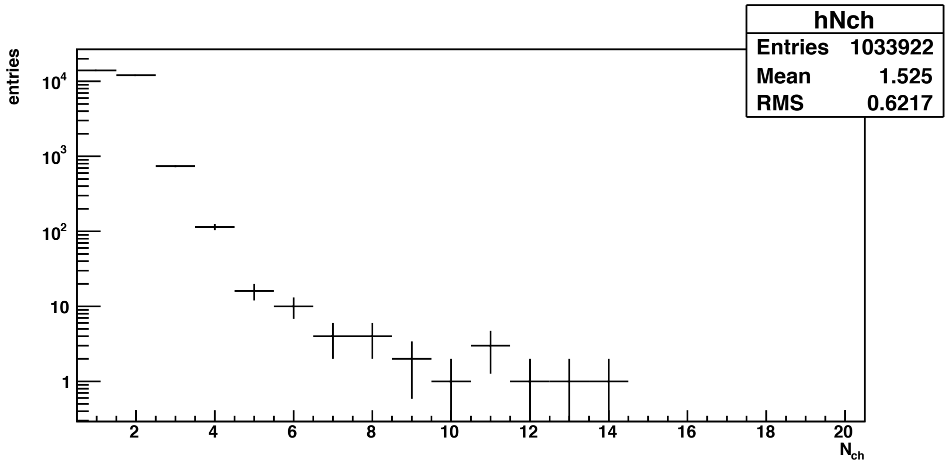

Figure 6.1: Multiplicity distribution (MD) from 10^6 cosmic events. Events with zero reconstructed tracks are included in the number of entries.

As the MD of cosmics events is not supposed to follow any of the discussed distributions the sole meaning of this analysis was to test the analysis procedure on real data.

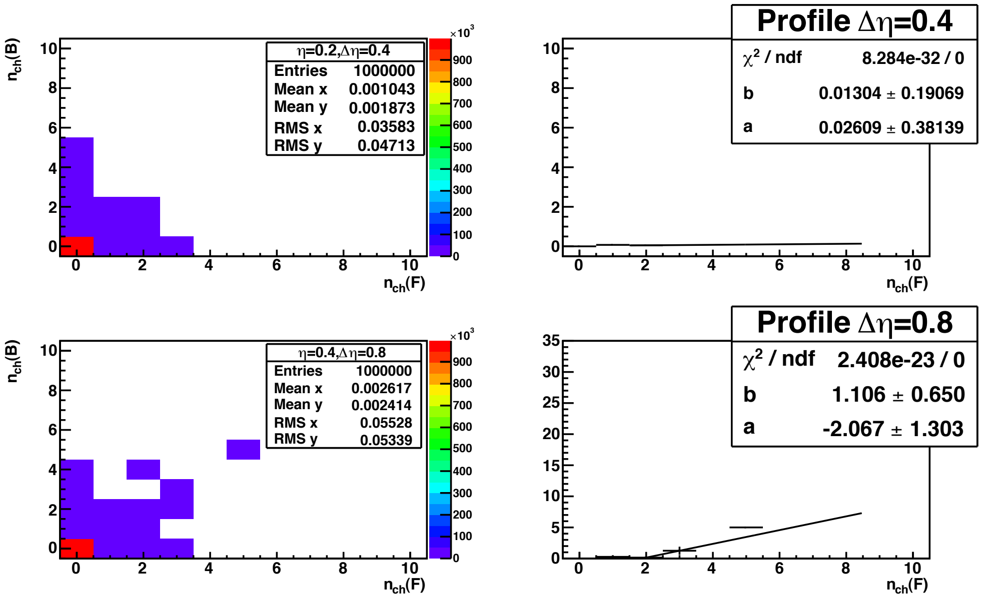

Figure 6.2: Forward-backward correlation plots obtained from 10^6 events collected during the ALICE TPC cosmic run of June 2008. Forward and backward η intervals are both 0.4 units wide. The results for the η windows centered at ± 0.2 ($\Delta\eta = 0.4$) and ± 0.4 ($\Delta\eta = 0.8$) are shown in the upper and bottom panels, respectively as correlation plots (left) and its fitted projections (right). Pseudorapidity gaps $\Delta\eta$ are defined from the center of the forward interval to the center of backward interval. No p_t cut is applied.

For cosmic showers, one expects a positive correlation between multiplicities in different acceptances due to the varying energy of the initial particle, reflected in the shower multiplicity. The fact that a single particle traversing the TPC can produce two reconstructed tracks also can contribute to positive correlations. The correlation strength b for cosmic events is within 0.013 ±0.19 ($\Delta\eta$=0.4) to 1.106 ±0.65 ($\Delta\eta$=0.8), being of 1.26 ±0.083 for intervals of full forward/backward pseudorapidity and zero $\Delta\eta$. It is important to note that the counts in the first bin of the correlation plot depend on the trigger details so the first bin of $\langle n_{ch}(F)\rangle$ was excluded in the determination of b (right panels of Fig. 6.2).

Chapter 7

Conclusions

In this thesis we developed an analysis of charged particle multiplicities for the ALICE experiment at the LHC and studied the multiplicity distributions and the multiplicity correlations in simulated pp collisions at LHC energies.

The multiplicity distribution from pp collisions at the LHC can be fitted by two negative binomial (NB) distributions which may be attributed to soft and semi-hard collision events. Each NB is characterized by two parameters, the number of contributing cells k and the average multiplicity $\overline{n}$. We compare the four parameters of the fit with the extrapolation of experimental data to $\sqrt{s} = 14$ TeV [Ugoc05]. The soft events have a lower average multiplicity and a smaller number of contributing cells and follow the KNO scaling. The semi-hard component has a higher average multiplicity and a higher number of contributing cells and breaks the KNO scaling; it may originate from string percolation or other additional sources expected to appear at high collision energies [Gel09, Brog09]. Concerning the detector response, the three considered samples give multiplicity distributions that match reasonably well for the ALICE TPC acceptance of $|\eta| < 0.9$. The errors of the NB fit parameters are low (around 3% of the value for k, 1% for $\overline{n}$) and we conclude that the TPC is perfectly suited for testing the existence of a second contribution to the MD, and with it, the breaking of the KNO scaling.

The forward-backward multiplicity correlations at the LHC are expected to be large (0.5-0.7) and only weakly dependent of the pseudorapidity gap $\Delta\eta$.

Short range correlations, originating from jets and/or resonance decays, can be avoided by going to higher $\Delta\eta$. A constant forward-backward correlation strength b over a long $\Delta\eta$ range might be a sign of string percolation [Brog09].

To calculate b, we used two different techniques. In the first method, called direct method, we fill correlation plots between forward and backward multiplicities and extract the correlation coefficient from this histogram. In the second method, called dispersion method, b is obtained from a calculation of the dispersion coefficients. Both methods show similar b values and tendency.

The dependence of b on $\Delta\eta$ for detector reconstructed tracks (ESD) closely follows that of the corresponding Monte Carlo Truth (MCT). The agreement is on the order of 5% which means that the forward-backward correlations are not seriously distorted by the apparatus and the data analysis.

Summarizing, we have demonstrated that the ALICE TPC detector is well suited for an analysis of the charged particle multiplicity and of the long range correlations in proton-proton collisions at the LHC, and we developed and tested software tools for this purpose. Using event generators we also estimated the results to be expected (Figs. 5.10 and 5.17). It should be noted that, while in this work the multiplicity distributions and the forward-backward correlations were discussed separately, in reality their features might come from the same origin. In fact, the existence of two classes of events, e.g. soft and hard ones respectively with low and high multiplicities, naturally leads both to a two-component multiplicity spectrum and to enhanced forward-backward correlations. These relations will be studied in depth with the ALICE experiment at the LHC by identifying and analyzing separately the various event classes. The experimental program of ALICE has just started with the first publication of the charged particle multiplicities observed in pp collisions at $\sqrt{s} = 900$ GeV [Ali10]. While the first paper was based on only 284 pp collisions, and the total statistics collected so far at 900 GeV is 250 k events, the current plan is to record at least 10^9 pp events at $\sqrt{s} = 7$ TeV within the 2010/2011 LHC running period. This number exceeds by several orders of magnitude the statistics considered in this thesis and will allow to perform a differential analysis addressing these important questions.

Bibliography

[Adar08] PHENIX Collaboration, A. Adare, et al, *Charged hadron multiplicity fluctuations in Au+Au and Cu+Cu collisions from* $\sqrt{s_{NN}}$ *= 22.5 to 200 GeV*, arXiv:0805.1521v1 [nucl-ex].

[Afan99] S. V. Afanasiev, *The NA49 Large Acceptance Hadron Detector*, Nucl. Instr. and Meth. A 430 (1999) 210.

[Alex95] T. Alexopoulos et al, *Charged particle multiplicity correlations in* $p\overline{p}$ *collisions at* $\sqrt{s}$ *= 0.3-1.8 TeV*, Phys. Lett. B 353 (1995) 155.

[Ali10] The ALICE Collaboration, *First proton–proton collisions at the LHC as observed with the ALICE detector: measurement of the charged particle pseudorapidity density at* $\sqrt{s}$ *= 900 GeV*, arXiv:0911.5430v2 [hep-ex]

[AliRoot] Alice Collaboration, *AliRoot, An Object-Oriented Data Analysis Framework*, http://aliweb.cern.ch/offline.

[Alme10] J. Alme et al. *The ALICE TPC, a large 3-dimensional tracking device with fast readout for ultra-high multiplicity events*, e-Print: arXiv:1001.1950 [physics.ins-det]

[Alne85] G. J. Alner et al., *Multiplicity distributions in different pseudorapidity intervals at a cms energy of 540 GeV*, UA5 Collaboration, Phys. Lett. B 160 (1985).

[Amel94] N. S. Amelin, *Long and Short Range Correlations: A Signature of String Fusion*, Phys. Rev. Lett. 73 (1994) 2813.

[Anso88] R. E. Ansorge for the UA5 Collaboration, *Charged particle correlations in* $p\overline{p}$ *collisions at c.m. energies of 200, 546 and 900 GeV*, Z. Phys. C 191 (1988).

[Anto07] D. Antonczyk, *Detailed Analysis of Two Particle Correlations in Central Pb-Au Collisions at 158 GeV per Nucleon*, PhD thesis, TU Darmstadt (2007).

[Babl08] S. R. Bablok *et al*, *High Level Trigger Online Calibration framework in ALICE*, J. Phys.: Conf. Ser. 119 (2008) 022007.

[Baer05] H. Baer et al, *ISAJET 7.78*, http://www.hep.fsu.edu/isajet/.

[Bene76] J. Benecke et al, *Forward-Backward correlations and the multiplicity distribution in high-energy collisions*, Nucl. Phys. B 110 (1976) 488.

[Bene78] J. Benecke, J. Kuhn, *How to see independent emission in hadronic production*, doi:10.1016/0550-3213(78)90319-X.

[Bial85] A. Bialas, F. Hayot *On the multiplicity distribution in e+e-¿hadrons* Phys. Rev. D 33 (1986) 39.

[Biag99] S. F. Biagi, *Monte Carlo simulation of electron drift and diffusion in counting gases under the influence of electric and magnetic fields*, Nucl. Instr. and Meth. A 421 (1999).

[Bram05] R. Bramm, *Characterization of the ALICE TPC Readout Chip*, PhD thesis, Frankfurt University (2005).

[Brog09] P. Brogueira, J. Dias de Deus, C. Pajares, *Long range forward-backward rapidity correlations in proton-proton collisions at LHC*, http://arXiv.org/abs/0901.0997v1.

[Brun87] R. Brun et al, *GEANT 3: user's guide Geant 3.10, Geant 3.11; rev. version*, CERN, Geneva, 1987.

[Brun97] R. Brun, F. Rademakers, *ROOT - An Object Oriented Data Analysis Framework* Proceedings AIHENP'96 Workshop, Lausanne, Sep. 1996, Nucl. Instr. and Meth A 389 (1997) 81-86.

[Carm07] F. Carminati, G. Bruckner, *The ALICE Offline Bible*, Version 0.00 (Rev. 22).

[Carr83] P. Carruthers, C.C. Shih, *Why the hadronic multiplicity distributions in e^+e^- annihilations are so narrow*, Phys. Lett. B 137 (1983).

[Chou83] K.C. Chou, L.S. Liu and T.C. Meng, *Koba-Nielsen-Olesen scaling and production mechanism in high-energy collisions* Phys. Rev. D 28 (1983) 1080.

[Corc01] G. Corcella et al, *HERWIG 6.5*, JHEP 0101 (2001) 010 [hep-ph/0011363].

[Dain03] A. Dainese, N. Carrer *A parametrizarion of the Kalman filter track reconstruction in the ALICE TPC*, ALICE-INT-2003-011.

[Dash09] A. K. Dash *Multiplicity distribution in pp collisions at LHC energies*, http://arxiv.org/pdf/0908.0188.

[Diam84] R. N. Diamond, *Total inelastic pion multiplicity distribution in 250 GeV/c pp interactions*, Phys. Rev. D 29 (1984) 368.

[Eng97] R. Engel, *PHOJET 1.10*, http://www-ik.fzk.de/engel/phojet.html.

[Foa75] L. Foá, *Inclusive study of high-energy multiparticle production and two-body correlations*, Phys. Rep. Vol. 22 (1975).

[Gar80] J. N. Marx, *Particle Identification by Energy Loss Measurement and Long Drift Imaging Chambers*, SLAC-R-239 SSI80-007.

[Gar98] R. Veenhof, *GARFIELD*, Nucl. Instr. and Meth. A 419 (1998).

[Gar04] C. Garabatos, *The Alice TPC*, Nucl. Ins. and Meth. A 535 (2004) 197.

[Gar06] C. Garabatos, *The ALICE TPC gas system: commissioning experience*, GSI Scientific Report (2006).

[Gel09] F. Gelis, T. Lappi, L. McLerran, *Glittering Glasmas* arXiv:0905.3234v3 [hep-ph]

[Gott84] K. Gottfried, V. F. Weisskopff, *Concepts of Particle Physics*, Oxford University Press (1984).

[Gros08] J. F. Grosse-Oetringhaus, *Measuring the charged particle multiplicity distribution with the ALICE detector*, ALICE-INT-2008-002.

[Gyu93] M. Gyulassy, X. N. Wang, *HIJING 1.0 A Monte Carlo Program for Parton and Particle Production in High Energy Hadronic and Nuclear Collisions*, LBL-34246 (1993).

[Int03] L. Betev, P. Chochula, *Definition of the ALICE Coordinate System and Basic Rules for Sub-detector Components Numbering*, ALICE-INT-2003-038.

[Int07] *ALICE(A Large Ion Collider Experiment)*, ALICE-INT-2007-008.

[Kian85] D. Kiang, S. H. Ling and K. Young, *Multiplicity distribution in hadron-nucleus scattering*, Phys. Rev. D 31 (1985).

[Kitt04] W. Kittel, *General characteristics of hadron-hadron collisions*, Acta Physica Polonica B 35 (2004).

[Koba72] Z.Koba, H.B.Nielsen and P.Olesen, *Scaling of multiplicity distributions in high energy hadron collisions*, Nucl. Phys. B 40 (1972) 317.

[Kras99] L. Diósi, S. Krasznovszky, I. Wagner, *KNO scaling in the neutral pion multiplicity distributions for p-$\overline{p}$ interactions at 40 and 250 GeV*, Phys. Lett. B 454 (1999) 381.

[Kras92] L. Diósi, S. Krasznovszky, I. Wagner *Description of charged-particle multiplicity distributions in e^+e^- annihilation at TRISTAN and LEP1 energies from AMY, ALEPH, OPAL and DELPHI collaborations*, Phys. Lett. B 295 (1992) 320.

[Lipp00] C. Lippmann, *Aufbau und Inbetriebsnahme eines Gasqualittsmonitor fr die HADES-Driftkamern*, Diplomarbeit. Frankfurt University (2000).

[Mari04] A. Marin, *New results from CERES*, J. Phys. G 30 (2004) 709.

[Morg01] T. Morgan, *Construction and Calibration of the STAR FTPC Drift Velocity Monitor*, Placement Report. Max-Plank-Institut fur Physik (2001).

[Pott96] K. M. Potter, *The Large Hadron Collider (LHC) project of CERN*, Technical report, CERN LHC Project Report 36, 1996. 333.

[Ppr104] ALICE Collaboration, *ALICE PPR I*, J. Phys. G 30 (2004) 1517.

[Prim06] P. Hristof, *AliRoot Primer*, http://aliceinfo.cern.ch/Offline/AliRoot/Manual.html.

[Sarc87] I. Sarcevic, *Is There Koba-Nielsen-Olesen Scaling at Fermilab Tevatron Collider Energies (1600-2000 GeV)?*, Phys. Rev. Lett. 59 (1987) 403.

[Sjos01] T. Sjostrand et al, *PYTHIA version 6.319*, Comp. Phys. Commun. 135 (2001) 238.

[Srim01] J. P. Biersack, L. Haggmark, *SRIM*, Nucl. Instr. and Meth. 174, 257 (1980).

[Srim02] J. F. Ziegler, *The Stopping and Range of Ions in Matter*, Vol. 2-6, Pergamon Press, 1977-1985.

[Tarn08] T. J. Tarnowsky, *Long-range multiplicity correlations in relativistic heavy ion collisions as a signal for dense partonic matter*, http://arxiv.org/abs/0807.1941v1.

[Tdr01] ALICE TPC Collaboration, *ALICE TPC. Technical Design Report*, CERN/LHCC 2000-2001.

[Ugoc01] R. Ugoccioni, A. Giovannini, *Superposition effect and clan structure in forward-backward multiplicity correlations*, Phys. Rev. D 66 (2002).

[Ugoc05] R. Ugoccioni, A. Giovannini, *Scenarios for multiplicity distributions in pp collisions in the TeV energy region*, J. Phys.: Conf. Ser. 5 (2005) 199.

[Uhli78] S. Uhlig et al, *Observation of charged particle correlations between the forward and backward hemispheres in pp collisions at ISR energies*, Nucl. Phys. B 132 (1978) 15.

[Wie04] J. Wiechula, *Präzisionmessung der Electronen-Driftgenswindigkeit in* $NeCO_2$, Diplomarbeit, Frankfurt University (2004).

[Wong94] C. Y. Wong, *Introduction to High-Energy Heavy-Ion Collisions*, Science (1994).

[Xu86] Cai Xu et al, *Statistical approach to non-diffractive hadron-hadron collisions: Multiplicity distributions and correlations in different rapidity intervals*, Phys. Rev. D 33 (1986) 5.

List of Figures

Acknowledgments

I would like to thank sincerely Professor Peter Braun-Munziger for the opportunity he gave me to join ALICE, for his precise comments about the work here shown and for his support to my situation in general. I furthermore acknowledge the help of Dr. Garabatos and Dr. Antonczyk who enlightened me about the meaning of being an experimental researcher, and thank for their almost endless patience, specially at the beginning of my days as a PhD student. I could not have reached this point without them.

This thesis would not have been written without the direction of Dr. Miskowiec. Therefore I direct to him my deepest gratitude. His special way of commenting and discussing was pushing me to continue and injecting me with the energy necessary to go ahead with what I was considering, at the very beginning, an easy task. If this work is something that can be considered interesting is mainly because of his tips in this direction.

I am indebted to all the ALICE group at GSI also. Special thanks to my office mates, Sedat Altinpinar, who had always time to discuss and who provided me with an unvaluable feedback, Benjamin Dönigus, who has a special ability to find the weak points of my writing, and to Anar Manafov, who tought me how to love my terminal, not to hate it, and who saved me a lot of time helping me to write a more beautiful code. I also give thanks to Dr. Bailhache, who enlightened me about the use of some of the ALICE specific code, and who showed enough curiosity about the subject of my studies to make it more interesting, and to Markus Fasel, who had always time to help me.

I can't also forget to mention all the people who read this work partially or all, and who made comments about the quality of the plots, the cleanliness of an expression or the absence or repetition or a concept. In this list of tireless readers apart from the ones already mentioned I want to include in first place Dr. Andronic, followed by Dr. Ricaud. I want to include some people who read it without knowing about the specific subject (but knowing about physics) like A. Alarcón, A. Merino, E. Fernández and many more.

Many thanks to all.

Eidesstattliche Erklärung

Hiermit erklare ich eidesstattlich, dass ich die vorliegende Dissertation selbständig verfasst, keine anderen als die angegebenen Hilfsmittel verwendet und noch keinen Promotionsversuch unternommen habe.

Darmstadt, den 7. August 2012

Juan F. Castillo Hernández

Curriculum Vitae

Name	Juan Francisco Castillo Hernández
Born the	21/08/1975 in Sevilla, Spain
Nationality	Spanish

Education

2009, March-June. Grant for the 2009 Doctoral Training Progam "Strongly Correlated Quantum Systems". ECT*, Trento, Italy (3 months).
2009, September. "EMMI seminar: QGP meets Cold Atoms". GSI, Darmstadt, Germany.
2008, July. "EMMI kick-off event". GSI, Darmstadt,Germany.
2007, September. Attendance to "Lecture Week on Chiral Simmetry - Fall 2007". Helmholtz Reseach School. Haus Bergkranz/Kleinwalsertal, Austria.
2006, May 18th. Technical University Darmstadt, Germany. Validation of a research report under the supervision of Prof.Dr. P. Braun-Munzinger as a Diploma thesis equivalent. "Development of a Ternary Mixture Monitor".
2005, April. GSI, Darmstadt, Germany. Join the ALICE german group under a PhD position.
2005, February. Grant for the CERN-TARGISOL Winter School. Casa E. S. José, El Escorial, Madrid, Spain.
2004, September 26- October 5. Grant for the "European Marie Curie Training Course. Low Temperature Plasma Physics: Basic and Applications",
Centre of Excellency Ruhr-University Bochum, CPS
Arbeitgemeinschaft Plasmaphysik (Bochum-Ruhr Univeersität)
Bad Honnef, Germany.
2004, February. **Licenciado en Ciencias Físicas** (Especialidad Fundamental) (Fundamental Physics Graduate, M.Sc) University of Seville.

Publications

- Charged-particle multiplicity measurement in proton-proton collisions at energy = 7 TeV with ALICE at LHC. 2010. ALICE collaboration.
- Charged-particle multiplicity measurements in proton-proton collisions at energy= 900 GeV and 2.36 TeV with ALICE at LHC. 2010. ALICE collaboration.
- First proton-proton collisions at the LHC as observed with the ALICE detector: measurement of the charged particle pseudorapidity density at energy = 900 GeV. 2010. ALICE collaboration.
- Development of a Ternary Mixture Monitor. Forschungarbeit-Diploma equivalent under the supervision of Prof. D. P. Braun-Munzinger. TU Darmstadt , 18th May 2006 .
- Experience with the Goofie during the TPC commisioning. INSMETH-33. GSI Scientific Report 2006. First author.
- Commissioning of the ALICE Time Projection Chamber. INSMETH-31. GSI Scientific Report 2006. Second Author.
- Phonons, surface vibrations and their effect on desorption kinetics. TARGISOL Winter School 2005. Casa E. S. José, El Escorial, Madrid, Spain, February 17-23, 2005. EU-project HPRI-CT-2001-50033. Conference contribution.